uOttawa

L'Université canadienne
Canada's university

t

FACULTÉ DES ÉTUDES SUPÉRIEURES ET POSTOCTORALES

uOttawa

L'Université canadienne
Canada's university

FACULTY OF GRADUATE AND POSDOCTORAL STUDIES

Catherine Aldous
AUTEUR DE LA THÈSE / AUTHOR OF THESIS

M.Sc. (Physics)
GRADE / DEGREE

Department of Physics
FACULTÉ, ÉCOLE, DÉPARTEMENT / FACULTY, SCHOOL, DEPARTMENT

Novel van der Waals Compounds in the Nitrogen-methane Binary Systems at Room Temperature and High Pressure

TITRE DE LA THÈSE / TITLE OF THESIS

Serge Desgreniers
DIRECTEUR (DIRECTRICE) DE LA THÈSE / THESIS SUPERVISOR

CO-DIRECTEUR (CO-DIRECTRICE) DE LA THÈSE / THESIS CO-SUPERVISOR

Javier Giorgi

Paul Finnie

Gerald Oakham

Gary W. Slater
Le Doyen de la Faculté des études supérieures et postdoctorales / Dean of the Faculty of Graduate and Postdoctoral Studies

Novel van der Waals Compounds in the Nitrogen-Methane Binary System at Room Temperature and High Pressure

Catherine Aldous

Thesis submitted to the

Faculty of Graduate and Postdoctoral Studies

in partial fulfillment of the requirements for the

M.Sc. degree in Physics

Department of Physics

Faculty of Science

University of Ottawa

Your file Votre référence
ISBN: 978-0-494-73858-0
Our file Notre référence
ISBN: 978-0-494-73858-0

Abstract

Beginning in the early 1990's, the study of binary mixtures containing simple molecules under high pressure led to the discovery of a solid van der Waals compound: a weakly bound molecular solid whose cohesion is primarily due to van der Waals forces. The formation of this type of compound, such as $He(N_2)_{11}$ discovered in 1992 in the helium-nitrogen system by Vos *et al.* [Vos, 1992], is predicted in systems such as those containing nitrogen and methane. The nitrogen-methane binary system is studied at room temperature under high pressure in order to construct the pressure-concentration phase diagram up to 16 GPa. Over 20 mixtures of varying concentration have been studied within a diamond anvil cell through Raman spectroscopy and powder X-ray diffraction using synchrotron radiation. Within the phase diagram, phases exist that resemble the pure species at similar thermodynamic conditions, and additionally, two novel van der Waals compounds are observed.

Statement of Originality

To the best of her knowledge, the author states that this thesis represents an original contribution in the field of high pressure solid state physics. Contributions of the author include planning, preparing, and conducting X-ray diffraction experiments at the Canadian Light Source (with the exception of the 64% sample, which was completed prior to the start of the author's graduate studies), performing Raman spectroscopy experiments at the University of Ottawa, and analyzing data to obtain and understand results. Although the majority of the work was done by the author, the author worked closely with supervisor Serge Desgreniers and occasionally with colleagues, who demonstrated procedures and offered occasional assistance with data acquisition, as expected with graduate studies.

Acknowledgements

I would like to acknowledge and thank the University of Ottawa, professor Serge Desgreniers and NSERC for providing generous financial support. This has allowed me to focus on research, attend enriching conferences and travel to the Canadian Light Source for experiments.

I greatly appreciate the opportunities to perform research at the Canadian Light Source using the Hard X-Ray Microanalysis beamline. The beamline scientists, Dr. Ning Chen and Dr. Chang-Yong Kim, were very helpful with these experiments, even well beyond their normal working hours. These experiments constitute a vital contribution to this work.

I am very grateful for the opportunity to work in the Laboratoire de physique des solids denses under the supervision of Serge Desgreniers. As part of this group, I have been able to work alongside my colleagues Jesse Smith, Daniel Pohl, Laura Downie and Alexandre Bouchard. My colleagues have offered me insightful discussion, support and camaraderie. I am thankful for Jesse Smith, for his selfless willingness to share his knowledge and experience. Daniel Pohl has also had a significant impact on my success as a graduate student; we started out as lab partners in our undergraduate degree, and quickly became best of friends. I am indebted to him for his friendship and support throughout the challenges of the university experience, and for inspiring me to enter the field of condensed matter physics.

With the Laboratoire de physique des solids denses, I was given the chance to develop specific skills as well as versatility as a young researcher. This would not have been possible without the patience and support of Serge Desgreniers. As a supervisor, Serge Desgreniers offered his time and knowledge to help me understand my research, while allowing me the independence to explore it. In spite of his busy schedule, he was always available for discussion. Most importantly, he inspired me to develop the curiosity and enthusiasm necessary to become a successful researcher.

Table of Contents

List of Figures

Chapter 2

Chapter 3

Chapter 4

Chapter 5

List of Tables

Chapter 2

Chapter 3

Chapter 4

1. Introduction

1.0 Introduction

The study of mixed molecular systems containing components such as nitrogen and methane contributes to our understanding of the universe. These molecules are found in the atmospheres, surfaces and interiors of planetary bodies [Raulin, 1982], [Kouvaris, 1991], [Quirico, 1995], [Sun, 2006]. On Earth, the air is 78% nitrogen by volume [Sihachkr, 2005] and methane is the primary component of natural gas [Sun, 2006]. Furthermore, nitrogen and methane are both considered to form some of the simplest known molecular crystals, and thus are important in defining and elucidating theories pertaining to the solid state.

A significant part of the study of the model molecular solids formed by nitrogen and methane can be summarized in a *phase diagram*. A phase diagram provides the thermodynamic conditions (i.e. temperature, pressure) necessary for achieving a particular *phase*. A phase describes the state of a material having consistent physical and chemical properties. A phase that is of the lowest possible energy is an equilibrium phase of the material for those particular thermodynamic conditions. Upon changing one or more thermodynamic variables, a state of lower energy may be available. In this case, the system undergoes a phase transition into the lowest energy state [Callister, pp. 237-238].

The phase diagrams of nitrogen and methane have been established across an extensive range of pressures and temperatures [Gregoryanz, 2007], [Tassini, 2005], [Sun, 2006], [Maynard-Casely, 2009] in which a high degree of polymorphism is observed. By mixing these molecules and varying the temperature, pressure and concentration of the components, a new phase diagram may be produced.

The phase diagram of a mixed system can be very different from those of the individual constituents. Within a mixed phase diagram, the number of phases that are thermodynamically stable can be determined by *Gibb's phase rule*:

$$\pi = k - f + 2 \qquad \text{(Equation 1.1)}$$

where the number of phases, π, is determined by the number of externally controlled variables, f, and the number of components in the mixture, k [Sears, 1975, pp. 210-215]. For a binary mixture (k = 2) with pressure and concentration varied (f = 2), a maximum of two phases can be observed.

The research presented here focuses on probing the undiscovered solid phases of the nitrogen-methane binary system. The overall objective is to construct the pressure-concentration binary phase diagram at room temperature at pressures ranging from 1 to 16 GPa. Since the pressure and concentration are varied while the temperature is fixed (f = 2), Gibb's phase rule displayed in Equation 1.1 restricts the number of possible phases to 2. In each phase region of the solid binary phase diagram there are several possibilities: phase segregation, in which the pure species exist in their respective structures, a solid solution, in which one component is dissolved in

the structure of the other, a compound, in which the two molecules exist in a structure different from that of their pure phases, or a combination of these possibilities.

Similar systems in which novel compounds were discovered have been studied. These compounds are classified as van der Waals (vdW) compounds, which are weakly bound molecular solids, found to be stabilized under high pressure [Vos, 1992]. The formation of vdW compounds is expected in the nitrogen-methane binary system. The results of this prediction are demonstrated in this work.

1.1 Thesis Outline

This thesis is divided into chapters: Chapter 1 is an introduction, Chapter 2 provides a review of the relevant literature, Chapter 3 outlines an overview of the experimental techniques, Chapter 4 presents the results, Chapter 5 is a general discussion and Chapter 6 provides conclusions as well as the future goals for this project.

The literature review presented in Chapter 2 is an overview of the study of materials under extreme conditions (Section 2.1) including the development of high pressure research and some of the applicable elements of this research pertaining to this work. Selected aspects regarding the study of binary mixtures and vdW compounds are reviewed (Section 2.2) and the previously published work on the nitrogen-methane binary system is described (Section 2.3). Prior to constructing a binary phase diagram, knowledge of the phases of each constituent is vital. The solid phase diagrams of pure nitrogen (Section 2.4) and pure methane (Section 2.5) are summarized with a focus on the relevant thermodynamic range (room temperature and high pressures up to 16 GPa).

Chapter 3 begins with a description of the protocol used in preparing the nitrogen-methane binary mixtures in the diamond anvil cell (DAC) (Section 3.1). A list of samples studied is displayed (Section 3.2) to demonstrate the range and extent of study. In order to characterize these mixtures at high pressure, Raman spectroscopy (Section 3.3) and X-ray diffraction (XRD; Section 3.4) are used. These techniques are powerful tools in describing the phases of the mixtures. Although the nitrogen-methane binary phase diagram includes the melting line and solid-fluid co-existence region, the focus is on the solid phases. Thus, the description of Raman spectroscopy and XRD is most relevant to the study of crystalline solids.

A *crystalline solid* is a periodic array of atoms or molecules, described by a repeating unit, the *unit cell*. The unit cell is characterized by its lattice parameters; these are the magnitude of unit cell vectors that define the three dimensional crystal [Kittel, pp. 4-5]. Describing the structure of the crystalline solids formed by the nitrogen-methane mixtures is important in constructing the binary phase diagram. The results of the investigation on these binary mixtures are presented in Chapter 4, which begins by displaying the proposed phase diagram (Section 4.1). The phase diagram includes phases that resemble those of the pure species. The analysis of these phases (Section 4.2 and 4.3)

demonstrate how the two molecular species interact at high density. From this, the solubility of nitrogen in the solid phases of methane, and that of methane in the solid phases of nitrogen can be determined as well as the effect of substituting one molecule in the lattice of the other. As predicted for this binary system, vdW compounds exist. Two compounds have been discovered as a result of this research: the T_1 compound (Section 4.4) and the MR compound (Section 4.5). These novel compounds are surprisingly complex, and their descriptions include the proposal of a unit cell, space group, number of molecules in the unit cell and stoichiometry.

After an account of each phase has been presented in Chapter 4, a general discussion follows in Chapter 5. The nitrogen-methane binary phase diagram is far from simple, particularly in the methane-rich portion (< 50% nitrogen). This side of the phase diagram presents a mixture of the two novel compounds, transitions significantly affected by hysteresis, and questions regarding the MR compound (Section 5.1). Other binary systems with similar components have been studied; a discussion relating and contrasting the nitrogen-methane binary system with similar systems is also presented (Section 5.2). Any parallel features between binary phase diagrams help shape the theories of these systems at high density. Finally, the validity of the results is discussed (Section 5.3).

The final chapter of this thesis, Chapter 6, provides a summary of the results obtained (Section 6.1) and an outline of future prospects for study of the nitrogen-methane binary system (Section 6.2). The phase diagram would benefit from additional refinement and further classification of the novel vdW compounds. Lastly, concluding remarks are presented (Section 6.3).

2. Literature Review

2.0 Introduction

Subjecting a material to extreme conditions such as high pressure can bring out polymorphism, surprising new properties and reactions. The study of materials under high pressure was significantly assisted by the development of the diamond anvil cell (DAC). The widespread use of the DAC was due in part to the advancement of the ruby fluorescence method for pressure calibration. High pressure research is an important aspect of materials science and has led to many discoveries including the structure of core materials, high-temperature superconductors, metallic phases, and the formation of vdW compounds, to name just a few.

The discovery of the first vdW compound is said to be that of Vos *et al.* in 1992 [Vos, 1992]. This compound, a solid weakly bound by vdW forces, consisted of nitrogen molecules and helium atoms in the unusual stoichiometry of $He(N_2)_{11}$. This was not the only vdW compound that was found to be stabilized under high pressure. However, it signified a new class of solids that can have important implications, for instance, in understanding planet formation and detonation mechanics. In order to comprehend the formation of these vdW compounds, it is essential to study other simple binary systems, like those containing simple molecules and noble gases.

The following sections introduce the fascinating world of high pressure research, outlining some of the momentous developments that pushed the experimental limits of this field. The subsequent sections focus on binary mixtures, their study under high pressure and some examples of some mixtures containing nitrogen and methane. This provides an introduction to the nitrogen-methane binary system, one that has been studied very little, with the previous studies restricted to low temperatures and low pressures. The description of this binary system represents the object of this research. Following this, the phase diagrams of nitrogen and methane are summarized. As this work deals with the study of the binary phase diagram over pressures from 1 to 16 GPa at room temperature, the focus is placed on the solid phases in this thermodynamic range.

2.1 The Study of Materials under Extreme Conditions

Extreme conditions can be considered to be anything that is far from what we normally experience. These extreme conditions can be created in the laboratory by the application of high pressure, and by cooling or heating materials. Extreme conditions are also present inside the Earth and throughout the solar system. The study of materials under extreme conditions is, therefore, imperative for the understanding of the formation of planets and surface ices [Katrusiak, 2007].

Subjecting materials to extreme conditions can also induce transitions or chemical reactions and dramatically affect the properties of the material. For example, Li, among many other elements, cooled to 15 K and subjected to 30 GPa becomes superconducting [Martinez-Canales, 2006]. The application of pressure has been instrumental in producing the highest critical temperature superconductors: $HgBa_2Ca_2Cu_3O_{8+\sigma}$ has a T_c of 166 K [Hemley, 2009]. The field of energetic materials also benefits from the application of extreme conditions. Theoretical studies show that nitrogen-rich compounds under extreme conditions (high pressure and high temperature) can undergo a transition into a form in which the nitrogen molecules are mostly single-bonded, which could be used to harness a tremendous amount of energy [Eremets, 1992].

The application of extreme conditions also induces rich polymorphism in materials. In 1998, the phase diagram of H_2O comprised 15 or so different phases [Hemley, 2002]. Taking simple hydrocarbons, such as methane, and applying 15 GPa and high temperature can produce diamond [Hemley, 2002]. Metallic phases have been identified in materials such as oxygen [Desgreniers, 1990] and have been predicted to occur for hydrogen. The metallization of hydrogen is an ongoing quest, as well as other features of hydrogen-systems such as high-density storage systems, in the application of clean energy delivery [Hemley, 2009].

The examples given here illustrate a mere fraction of the impact that the study of materials under extreme conditions could have. The universe offers an incredible range of temperature and pressure conditions and the pursuit of obtaining these conditions in the laboratory is ongoing.

2.1.1 High Pressure

When discussing the application of pressure, the SI unit, the pascal (Pa) is commonly used; currently, high pressures are described in terms of gigapascals (GPa), or 10^9 Pa. This work deals primarily with a range of 1 – 16 GPa. The magnitude of this pressure range can be realized upon comparing to atmospheric or room pressure, which is accepted as 101,325 Pa (1.01×10^{-4} GPa). Current experimental capabilities have been known to create pressures of a few hundred gigapascals. However, at these extreme values, monitoring the pressure precisely becomes difficult. There have been claims of pressures exceeding 500 GPa since the late 1980's [Bassett, 2009], [Syassen, 2008].

Even 500 GPa of pressure pales in comparison to some of the pressures present in the solar system. Although adequate for the description of the interior or the Earth, which is just over 360 GPa, these pressures are insufficient to describe the formation of other planets such as Jupiter, whose interior reaches 4000 GPa [Katrusiak, 2007]. Pressures found elsewhere in the universe go much higher than this; for example, the interior of a star like our sun is estimated at 1.5×10^7 GPa and the interior of a neutron star is on the order of 10^{29} GPa [Katrusiak, 2007]. With such a range available, pressure becomes an extremely powerful variable in the study of materials. Table 2.1 illustrates this range with examples of pressures observed in the universe.

Table 2.1: Pressures Found in the Universe

Example	Pressure
Ultra high vacuum obtained in a lab	10^{-18} GPa
Sea level (atmosphere)	1.01×10^{-4} GPa
On the bottom of Marians Trench (11,000 m deep)	1×10^{-1} GPa
Next-generation turbines in engines and electrical power plants (~1000 K)	4×10^{-1} GPa
Crust-mantle boundary of Earth	1 GPa
First DAC without gasket	1.0×10^{1} GPa
Center of the Earth	3.64×10^{2} GPa
Highest pressure claimed in the lab in 1987	5.5×10^{2} GPa
Interior of Saturn	2.5×10^{3} GPa
Interior of the Sun	1.5×10^{7} GPa
Inside a neutron star	10^{29} GPa

Table 2.1: Examples of pressures throughout the universe. Values are adapted from various sources [Hemley, 2009], [Smith, 2009], [Eremets, p. 50], [Katrusiak, 2007]. Note: neutron star and planet interiors are also at extreme temperatures.

2.1.2 Producing High Pressure in the Laboratory

The accessibility of high pressure research is basically attributed to the invention of the diamond anvil cell (DAC), which is described in detail in the next section. The DAC has been celebrated as the most important development in instrumentation for high pressure research since its design and implementation in 1959 by Jamieson *et al.* [Jamieson, 1959] and Weir *et al.* based on the ideas of Bridgman [Katrusiak, 2007]. However, prior to its invention and still employed today are other high pressure cells and hydraulic presses.

Although it is not discussed in detail, it is important to mention the piston-cylinder system for pressure generation. Driving a piston into a cylinder, either on one or both side, to compress a sample is a simple method for reaching static pressures up to 5 GPa, but typically less. This apparatus is not as versatile as pressure cells such as the DAC, as optical measurements are more difficult to make [Eremets, p. 120].

The basic features of high pressure cells include anvils (not necessarily diamonds), used to transfer a force to its smaller area to compress a sample. There is a gasket that supports the anvils, contains the sample (although in some cases, the gasket is created by the extrusion of the sample itself) and provides the isotropic compression of the sample. The design of the Bridgman anvil apparatus was an important development that led to the widely used and praised DAC. The Bridgman anvil apparatus originally employed tungsten carbide anvils and reached pressures around 10 GPa [Emerets, p.36]. Using diamond anvils in this design has many advantages, as diamonds are transparent to a wide range of wavelengths and can withstand extremely high pressures, routinely surpassing 100 GPa, with a reasonable maximum considered to be about 400 GPa. A big disadvantage of the DAC, however, is the limited sample volume.

The diamond anvils of a DAC can be altered to accommodate a larger sample volume. Typical diamond anvils have parallel surfaces – the table (the larger surface, over which force is applied) and the culet (the smaller surface which is in contact with the sample). By implementing a nonflat culet, such as one with a cupped or grooved surface, sample volumes can be increased several times. However, the maximum pressure obtained is typically much lower [Eremets, pp. 35-45].

Other cell designs, anvil types, and choice of gasket are implemented to perform a particular type of study. For example, cells with sapphire anvils may be used to perform Raman spectroscopy (see section 3.3) as they exhibit less luminescence than diamond. It also permits data to be taken where the Raman peaks of diamond overpower that of the sample. It also has the advantages of additional transparency to ultraviolet light beyond that of diamond, and a larger sample volume. The sapphire typically operates to about 15 GPa [Emerets, 83].

For this work, a DAC provides the opportunity to perform XRD and Raman spectroscopy measurements, encompassing an adequate volume such that the signal obtained is sufficiently strong to study the material. Thus, only the DAC is described in further detail.

2.1.3 The Diamond Anvil Cell

The diamond anvil cell is praised for its large range of capabilities by high pressure researchers. It can produce megabar pressures (hundreds of gigapascals), and allows for high or low temperature studies, different types of diffraction and scattering experiments, as well as spectroscopy and other physical measurements, while being compact enough to fit in the palm of your hand. Perhaps the most remarkable quality of the DAC is that it allows one to visually observe a sample while it undergoes phase transitions and crystallization, melting, phase separation and other pressure-induced effects [Bassett, 2009].

There were numerous developments leading to the DAC that we use in the lab today as well as countless designs that aim towards different purposes. There have been numerous review articles outlining the progress of this device [Jayaraman, 1986] [Katrusiak, 2007]. A short and non-exhaustive timeline of important events is presented here.

Table 2.2: Timeline of Some of the Important Developments in DAC design

Year	Development
1937	The formulation of the principle of massive support and the opposed anvil cell is derived by Bridgman, using tungsten carbide anvils producing pressures of 10 GPa
1950	Lawson and Tang used diamonds in a high pressure cell
1959	The DAC is designed independently by Jamieson and Weir and colleagues for different purposes
1962	A metal gasket is employed for sample containment and generation of hydrostatic pressure by van Valkenburg
1972	Forman and colleagues create a pressure scale using ruby-fluorescence

1976	Pressures of 120 GPa have been achieved
1977	Buras and colleagues used synchrotron XRD on a sample in a DAC
1982	A dedicated beamline for high pressure research is described by Hazen and Finger
1987	Pressures of 550 GPa (at 300K) have been claimed

Table 2.2: Select events that contributed to the development of the DAC from various sources [Katrusiak, 2007], [Bassett, 2009], [Jayaraman, 1986].

The general idea of the DAC is shown in Fig. 2.1. The two opposing diamond anvils face each other with their culets and tables parallel to each other. The table of the anvils are supported by the rigid seats (not shown) which also provide an aperture for visual observation and performing measurements. Between the culets, a drilled metal gasket extrudes around the anvils and creates a compression chamber. The sample is placed inside the compression chamber, along with a pressure gauge, such as an internal standard or piece of ruby, and in some cases a pressure-transmitting medium. The body of the cell consists of a piston and cylinder (not shown), each with one seated diamond anvil. Putting the piston into the cylinder and turning a few pressure screws causes the anvils to be driven towards each other, applying pressure onto the compression chamber.

Employing diamonds in a pressure cell has allowed for the production of ultrahigh pressures. The diamond anvils, known as the hardest material, are brilliant cut and are usually between a tenth and a third carat in weight. The weight and cut are chosen with respect to the specific purpose of the diamond anvil cell and experiments to be carried out [Smith, 2009]. The maximum pressure offered by a DAC is dependent on the size of the culet, which is evident from the definition of pressure as force over area. A pressure of roughly 50 GPa can be obtained with the use of 600 μm diameter culets, and culets of half that size can produce pressures of 100 GPa with a similar force. For experiments above 100 GPa, a bevelled cut is required [Eremets, pp. 49-55].

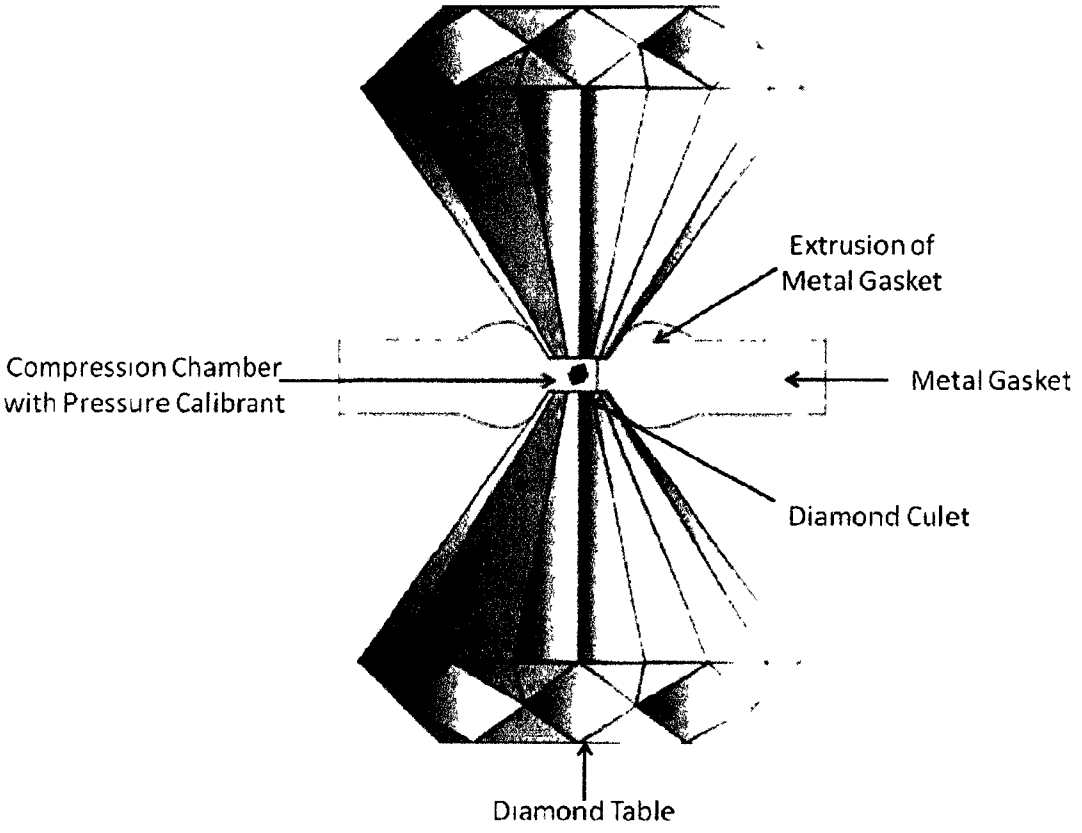

Figure 2.1: Schematic diagram of the interior of a DAC.

The diamonds also offer the transparency available with the DAC. The diamonds are transparent to electromagnetic radiation ranging from the ultraviolet to X-ray range, allowing a variety of studies to be performed: Raman spectroscopy, Brillouin scattering, IR spectroscopy, optical absorption, and X-ray diffraction (XRD) for short wavelengths [Bassett, 2009].

Originally, the sample was placed and compressed between the anvils until only a thin layer remained. The sample accumulating around the edge of the culet acted as a gasket. However, the pressure across the sample was not uniform and caused the diamond faces to become distorted. The implementation of a metal gasket allowed for hydrostatic pressure generation and the ability to use in situ pressure calibrants for more accurate pressure measurement [Smith, 2009].

The seats are typically made of a material strong enough to withstand the stress incorporated with driving and supporting the diamonds, such as hardened steel or tungsten carbide. However, it is important that they still provide a sufficient optical aperture. The wider the optical opening, the less support is provided to the diamonds. Thus, the material chosen is dependent on the function of the DAC, and in some cases different materials, resulting in different optical accessibilities, are used for each seat. For example, beryllium seats are useful for X-ray transparency, although to provide adequate support to the diamond anvil, a smaller optical aperture is required.

The specific types of DACs used in this work are presented in section 3.1. In addition to the design, this section provides specifications including diamond and gasket type, sample diameter and thickness, and seat material.

2.1.4 In Situ Pressure Measurement

The widespread use of the DAC for high pressure research was in part attributed to pressure calibration by the ruby fluorescence technique. The ruby fluorescence technique involves a spectroscopic measurement of the R_1-R_2 doublet, demonstrated in Fig. 2.2, and allows for convenient pressure measurement over a wide range of pressures. The addition of a ruby chip or microsphere is simple, does not disturb the sample, and causes very little interference in XRD patterns. The piece of ruby is generally a microsphere of 5-15 μm in diameter and thus occupies a small fraction of the sample space.

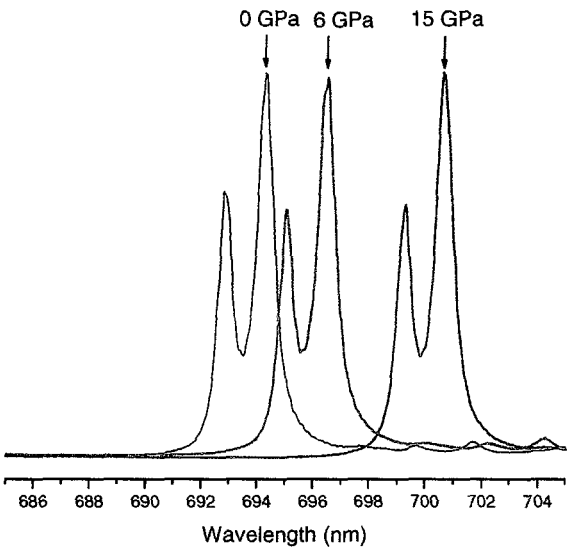

Figure 2.2: The fluorescence of a ruby ($Al_2O_3:Cr^{3+}$) measured at ambient pressure, 6 GPa and 15 GPa to demonstrate the shift in wavelength associated with increasing pressure.

The use of the ruby fluorescence technique as a pressure calibration method was advanced by several groups, each adding to the accuracy of the scale and pushing the pressure limit. The scale was originally proposed to be linear. The linearity of the ruby scale remains up to about 20 GPa [Katrusiak, 2007]. The scale remains accurate up to 180 GPa with a modification proposed by Mao *et al.* [Mao, 1978]:

$$P[\text{GPa}] = 380.8\left[\left(\frac{\lambda}{\lambda_0}\right)^5 - 1\right] \qquad \text{(Equation 2.1)}$$

where λ is the wavelength at the current pressure and λ_0 is the position of the R_1-line at ambient pressure [Jayaraman, 1983]. Slight modifications to this relationship are required for ultrahigh pressures, but this form is sufficient for the current work extending to 16 GPa. At room temperature, the ruby scale is estimated to be accurate to 0.01 GPa [Eremets, 176].

This technique has the great advantage of its wide pressure range, but other techniques are implemented for pressure calibration as well. Internal standards are convenient for XRD

experiments since they do not require any additional measurements. It involves using a material with a well-established equation of state, usually one with a high symmetry structure and strong scattering ability. Common internal standards include metals (Pt, Mo, Au), NaCl and SiO_2 [Katrusiak, 2007]. This technique also has some obvious disadvantages. The XRD images acquired contain reflections from both the standard and the sample, which can make analysis of low symmetry structures particularly difficult. It is also necessary to select an internal pressure standard that does not react with the sample, air or the pressure medium and is a viable pressure calibrant in the desired range of pressure. [Angel, 1997]. Other techniques for pressure calibration include a fixed-point scale, in which well-known melting point or transitions are used to predict the pressure of the cell [Katrusiak, 2007].

For this work, the ruby fluorescence technique is used for its simple and accurate measurement. Since the DAC used does not permit a large volume, the use of a small ruby microsphere does not disturb or react with the sample, and thus, it is an appropriate pressure gauge.

2.2 The Study of Binary Mixtures

In the 1990's, there were many investigations on the solid phases of binary systems. In particular, these studies focused on the high pressure solid phases, which were made easily accessible with the development of the DAC [Schouten, 1995]. Since information on the thermodynamics of binary mixtures cannot be trivially obtained by adding the weighted values of the pure species, experimental studies on simple binary systems is essential for the development of theory [Schouten, 2001].

The effect of adding one component to another can significantly impact its physical properties and phase diagram. This can shift phase transitions to different thermodynamic conditions or shift the phases lines associated with the pure components. It can also induce new transitions into disordered mixed solids, or more interestingly, form solid compounds with physical properties quite different from those of the separate components [Kooi, 1999], [Schouten, 1999].

In 1992, Vos et al. [Vos, 1992] claimed to have observed a new phenomenon; the formation of a solid van der Waals (vdW) compound. Just as gas atoms or molecules can be bound by vdW interactions, weakly bound multi-component compounds can be formed in the solid state. Prior to this discovery, molecular binary systems were seen to exist as either a solid solution, or a mixture of the pure phases. Vos and co-workers remark that vdW solid compounds could represent a new class of solids. This study indentified the stoichiometric compound $He(N2)_{11}$ while exploring the high pressure binary phase diagram of helium and nitrogen. This inspired the study of more simple binary systems under high pressure and the revealing of many other vdW solid compounds.

The understanding of the formation of these vdW compounds can be important in many areas of research. In planetary systems, high pressures exist and there is an abundance of simple molecular species influenced by vdW interactions. The phase diagrams of the mixed systems of these molecules have a significant impact on our understanding of the composition of planets, satellites, and surface ices. [Vos, 1992], [Schouten, 1995]

In a binary system, it is also possible to shift phase transitions, possibly even eliminate them. Thus, their phase diagram may allow more accessible pathways to novel, and hopefully useful, phases. This has been proposed as a possible mechanism for more easily obtaining metallic

hydrogen [Ulivi, 1999]. Studying mixed systems under high pressure could also offer insight into the idea of high density hydrogen storage systems and detonation mechanics [Somayazulu, 1996].

The following sections offer a brief summary of investigations done on selected phase diagrams, and describe some of the vdW compounds identified. Of course, there are several other important features of mixtures such as the formation of clathrates, gas-gas, fluid-gas and fluid-fluid equilibria [Schouten, 1995]. However, these aspects lie beyond the scope of this project.

2.2.1 The Discovery of vdW Compounds

As stated, Vos et al, 1992, claimed to have documented the first occurrence of a solid vdW compound in the helium-nitrogen binary system. The compound observed in a DAC was described as possessing well-developed crystal facets, which was unusual for these simple components that normally exist as rounded crystals. The stoichiometry of $He(N2)_{11}$ was based on molar composition and the compound was defined by a hexagonal unit cell containing 24 entities: 2 helium atoms and 22 nitrogen molecules. Lattice parameters at 12.6 GPa are given to be a = 8.019 Å and c = 9.461 Å. [Vos et al 1992]

The stoichiometry of $He(N2)_{11}$ was quite unexpected, as it deviated from the Hume-Rothery rule for compound formation in dense metallic systems. This rule stated that solubility for these systems is strongly affected by geometry. Thus, the diameter ratio, α, should predict whether compound formation is possible and for which molar ratios. Specifically, α is required to be above 0.85 for compound formation.

The formation of $He(N_2)_{11}$ (the helium-nitrogen diameter ratio is 0.62 [Kooi, 1999]) as well as compounds in other systems challenge this rule. It is also necessary to take into account the molecular shapes and intermolecular potentials of the components [Schouten, 2001]. Hence, the study of vdW compounds in simple systems formation is crucial in refining its theoretical description. [Loubeyre, 1993] This became one of several motivations for the study of binary systems under high pressure.

Many binary systems have been studied in efforts to find other vdW compounds beginning in the early 1990's. Studies are still being performed in 2010 on systems containing simple molecules and/or noble gases [Weck, 2010].

2.2.2 Experimental Techniques for Constructing Phase Diagrams

In section 2.1, the DAC was discussed for its versatility in the study of materials as a function of pressure and temperature. The effect of the application of pressure can be characterized with the use of many techniques. This section focuses on Raman spectroscopy and XRD, as these are the main techniques applied in this work. These complementary methods are discussed in greater detail in Chapter 3.

Raman spectroscopy and XRD are helpful for the study of materials in the DAC, and thus provide a means for exploring phase diagrams. Specifically, the present work deals with the construction of a pressure-concentration phase diagram at constant temperature. In order to construct this unknown phase diagram, the phase boundaries must be defined, the phase mixtures distinguished, and the corresponding structures determined.

Raman spectroscopy is a powerful tool for probing the vibrational energy levels of the molecules within the mixture. A Raman spectrum shows characteristic vibrational modes that depend on the molecular species, and provide details regarding their orientational and translational behaviour [Schouten, 2001]. Although determining the exact crystalline structure and atomic positions is not possible with Raman spectroscopy alone, phase transitions can be well defined (provided that they are accompanied by changes in the vibrational modes). Raman spectroscopy is sensitive to changes to the molecules within the environment of a crystal, so it can indeed be useful for studying mixtures [Bini, 1998]. Phase transitions can be observed from the appearance, splitting or disappearance of modes, or more subtly, by broadening or change of slope of vibrational frequency over pressure.

XRD, especially combined with synchrotron radiation, is essential for obtaining detailed structural information of the phases. Structural changes are clear based on the changes in the XRD pattern, and multiple phases are distinguishable. From the XRD pattern, it is possible to obtain the unit cell, space group, equation of state, and positions of the atoms in the crystal. It also gives an idea of the time and space-averaged disorder [Cromer, 1980]. Of course, the amount of information obtainable from an XRD pattern depends on the quality of the sample and requires extensive data analysis.

2.2.3 Relevant Binary Systems

Most of the binary systems that are studied under pressure in the search of vdW compounds include simple molecular species, such as nitrogen, methane, oxygen and hydrogen and/or noble gas atoms. These simple systems provide an opportunity to develop theories on the interactions and compound formation between components at high density.

Nitrogen has been studied in mixtures with a noble gas in order to reveal the effects of mixing spherical and almost spherical particles that weakly interact [Kooi, 1999]. Binary vdW compounds have been discovered in the nitrogen-helium [Vos, 1992], nitrogen-neon and nitrogen-xenon [Kooi, 1999]. In mixtures with helium, neon, and krypton, stoichiometric compounds are observed. Oxygen has also been studied with these noble gases, and stoichiometric compounds are also observed [Weck, 2010].

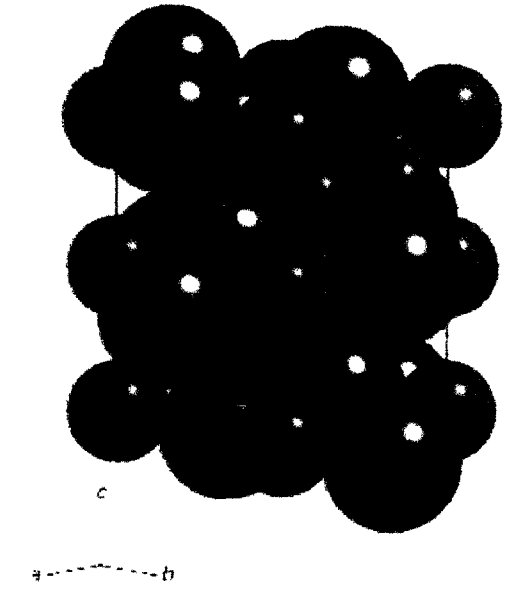

Figure 2.3: The $CH_4(H_2)_2$ compound with methane molecules represented by blue spheres and the hydrogen molecules represented by red spheres; both molecules are orientationally disordered. This structure is the same as $Ar(H_2)_2$, where the methane molecules would be replaced by argon atoms [Somayazulu, 1996].

Methane-hydrogen mixtures exhibit a very interesting phase diagram with the formation of four different stoichiometric compounds below 8 GPa at room temperature, including one displayed in Fig. 2.3. One of these compounds, $CH_4(H_2)_2$, has a structure that is extremely close to that of $Ar(H_2)_2$. Argon and methane are practically the same size, so similarities in their binary phase diagrams with hydrogen are expected. The argon-hydrogen system, however, has only one documented compound [Somayazulu, 1996], [Ulivi, 1999]. Although parallels can be found between binary mixtures with similar components, differences also exist that highlight the complex nature of binary mixtures.

2.3 The Nitrogen-Methane Binary System

Novel vdW compounds have been identified in other binary systems as previously described. Nitrogen and methane have a molecular diameter ratio of about 0.96. The mixed system is thought to be ideal to study due to their similar size and intermolecular potentials [Schouten, 1995]. Yet, this system has not been given significant attention at high pressures, and so it is the main objective of this work to determine if vdW compounds exist in the high pressure nitrogen-methane binary system. This section outlines some of the work previously done on this system.

Methane and nitrogen both possess simple shapes and thus their mixtures are said to provide a model system to elucidate existing theories on molecular interactions [Zhang, 1992]. The early stages of development of the solid-solid nitrogen-methane phase diagram started with the determination of the solid-liquid equilibrium. The solid-liquid equilibrium of this system was studied in 1939 by Fedorova and then in 1941 by Fastovskij and Krestinskij. Discrepancies in these studies inspired Omar *et al.* to re-determine the complete melting line in 1962. This was done at several low pressures (0.25, 0.7 and 2 atm). The increase in pressure brings the gas-liquid and liquid-solid regions further apart [Omar, 1962]. The liquid-solid region appears to increase in size, spanning more of the phase diagram, shown in Fig. 2.4.

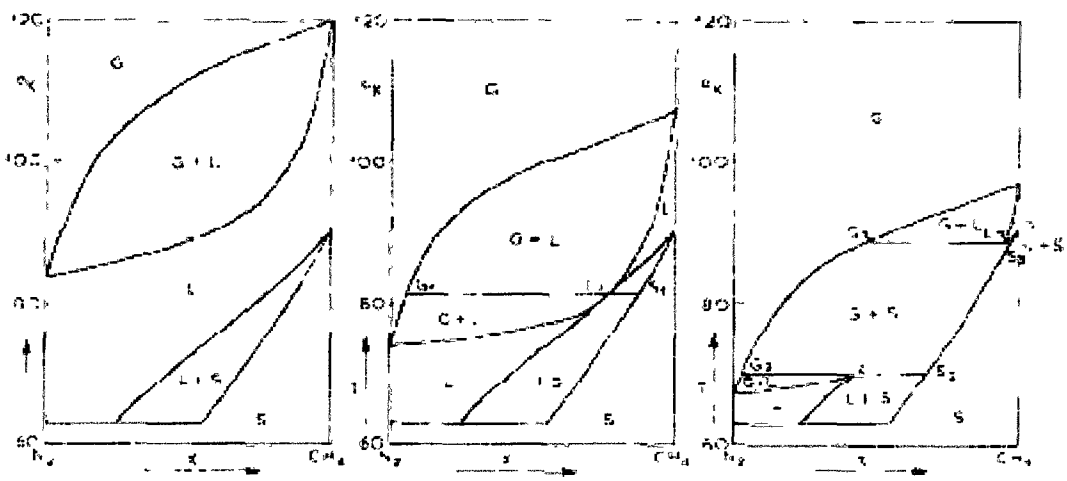

Figure 2.4: The T-x N_2-CH_4 phase diagrams at (left) 2 atm, (middle) 0.7 atm and (right) 0.25 atm. The temperature increases up the vertical axis and the amount of nitrogen in the mixture increases left [Omar, 1962].

In 1983, the low temperature solid binary phase diagram was studied at ambient pressure with XRD. At 62 K, this phase diagram shows the solubility of nitrogen in the I-CH_4 structure is 45%, and the solubility of methane in the β-N_2 structure is 23%. At lower temperatures, below 36 K the solubility of nitrogen in methane is 3-4% and 1-2% for methane in nitrogen. This represents a temperature range for which nitrogen is in the orientationally ordered phase, α-N_2. Below 62 K, a solid solution exists in the concentration range beyond the solubilities mentioned [Prokhvatilov, 1983]. This study was completed to better define the solubility limits after a solid-solid phase diagram was proposed in 1980 by Connolley *et al.* This study presented fewer data points and phase lines that were not well defined. One interesting comment made in this study, however, was that increasing methane concentration resulted in increasing lattice constants in the mixed solid phases [Connolley, 1980].

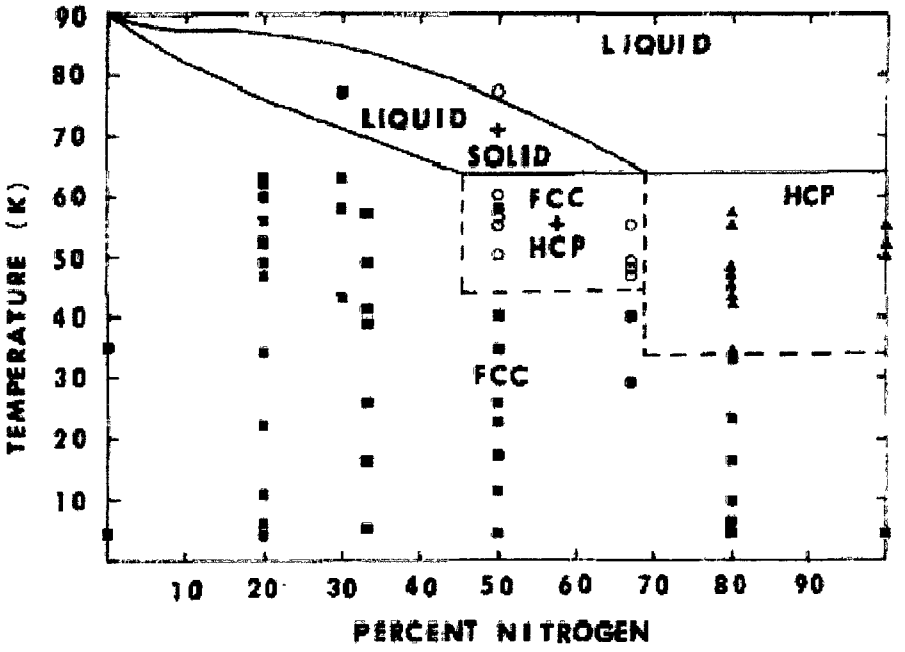

Figure 2.5: The solid-solid phase diagram for the nitrogen-methane system at low temperature as determined by XRD [Connolley, 1980]. Phase lines separating the different face-centered cubic (fcc) structures are not included, so this does not give an accurate representation of the solubility of one component in the pure structure of the other. Both nitrogen and methane exist in fcc structures in the low temperature range. Above ~35K, nitrogen exhibits a hexagonal-close-packed (hcp) structure and methane maintains its fcc phase.

2.4 The Solid Phases of Nitrogen

Out of the seven elements that form diatomic molecules under room conditions, nitrogen has the strongest intramolecular forces. Despite the simplicity of the molecule, its phase diagram is surprisingly complex, consisting of many different crystal structures as well as an amorphous phase above 100 GPa. In addition to the polymorphism of nitrogen, the structures of lower pressure phases of nitrogen have been a subject of debate, with many conflicting proposals for molecular orientation and symmetry group.

Commencing in the early 1980's, many studies attempted to uncover the structure of the room temperature solid phases of nitrogen using XRD techniques. As the accessibility of high pressure XRD rose, more and more studies offered increasingly rigorous descriptions of the structures of these solid phases, and the phase diagram was consistently extended. In 2007, Gregoryanz *et al.* performed XRD studies up to 170 GPa and 2500 K, identifying new phases and presenting the phase diagram of nitrogen, shown in Fig. 2.6.

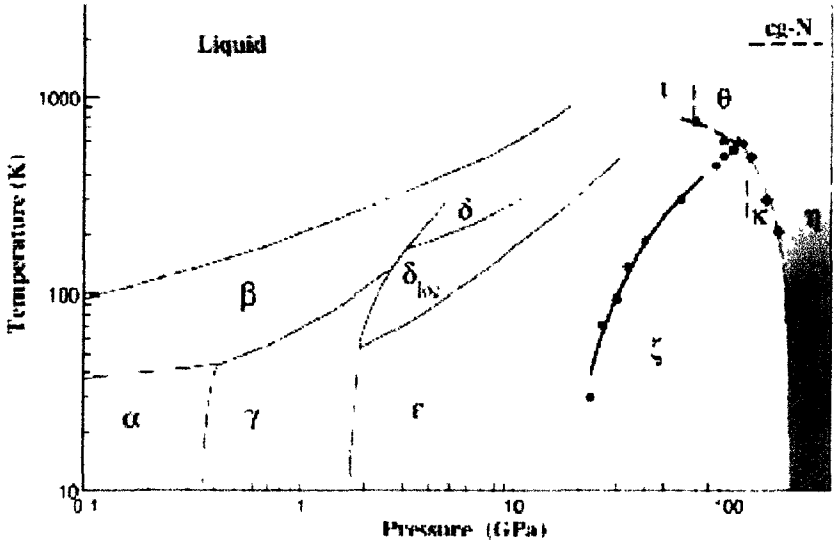

Figure 2.6: Phase diagram of nitrogen [Gregoryanz, 2007].

Since the nitrogen-nitrogen triple bond represents a large amount of energy, the ability to harness this energy is highly desired. Obtaining nitrogen in a state that is primarily single-bonded would represent a significant amount of energy and an important application to energetic materials. For this purpose, nitrogen and nitrogen-rich materials have been studied at very high pressures and high temperatures in hopes of discovering a phase which can be retrieved at ambient conditions. This is one of the applications that motivate the extension of the phase diagram of solid nitrogen [Eremets, 2004].

The complexity of nitrogen's solid phases is emphasized by the fact that papers are currently being published, attempting to fully describe their structures, yet still there are unanswered questions [Stinton, 2009]. The room temperature phases of solid nitrogen up to 16 GPa are described in detail in the following sections. Only a brief summary of the lower temperature and higher pressure phases is provided.

2.4.1 The Extensive Nitrogen Phase Diagram

The phase diagram displayed in Fig. 2.6 shows the polymorphism of nitrogen. At ambient pressure, nitrogen solidifies at 63 K into the β phase and upon further cooling transforms into the α phase at 36 K [Zinn, 1987]. The β phase also exists at higher temperatures under low pressures. Under low pressures and low temperatures, the γ phase exists. These low temperature phases have well-established structures of high symmetry. The α phase structure is face-centered cubic, *Fm3m*, the β phase is hexagonal-close packed with space group $P6_3/mmc$, and the gamma phase is tetragonal with space group $P4_2/mnm$ [Quentrec, 1975], [Mills, 1985].

At room temperature, nitrogen solidifies into the β phase at 2.4 GPa and upon further compression transforms into the δ phase at 4.9 GPa, moves into the intermediate δ_{loc} phase at 10.5 GPa, then into the ε phase at 16 GPa. The δ_{loc} phase was only introduced to the phase diagram in the 1990's, well after the δ and ε phases were known. Although the δ, δ_{loc} and ε unit cells are related, differences arise in the molecular orientation and ordering.

At very high pressures, nitrogen exists in other phases with different crystalline and amorphous structures. The ι and θ phases exist under high pressure and high temperature. The κ and ζ phases require high pressure, but temperatures lower than the ι and θ phases. Due to their relatively recent discovery, there has not been extensive work done to precisely define the phase boundaries of these structures. The η phase represents a nonmolecular phase of nitrogen [Gregoryanz, 2002].

2.4.2 β-N_2

Nitrogen exists in the β phase above 2.4 GPa at room temperature and between 63 K and 36 K at room pressure. The β phase is characterized by a hexagonal unit cell with two molecules, a c/a ratio close to the ideal ratio and space group $P6_3/mmc$ [Zinn, 1987], [Schiferl, 1983].

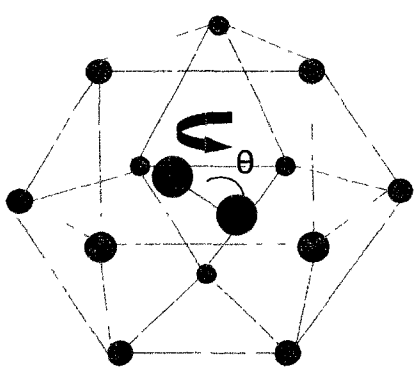

Figure 2.7: The structure of β-nitrogen. The nitrogen molecule is disordered in the hexagonal unit cell. The nature of disorder is difficult to define. It is possible that the molecules precess about θ [Hemley, 2000], [Streib, 1962].

Swenson [Swenson, 1957] summarized the structure of β nitrogen to have a structure that is dynamically disordered; the molecules precess about their center of gravity. Later experiments by Schuch and Mills in 1970 find that the c/a is constant with pressure up to 0.4 GPa, which is actually

very close to the ideal ratio. They remark that even with increasing pressure, the molecules in the β phase do not possess a higher degree of order than in the structure at ambient pressure [Schuch, 1970].

A single crystal XRD experiment [Streib, 1962] proposed a modification to the structure of β-nitrogen. He suggested that the centers of the molecules in the structure were situated at an angle with respect to the c axis. The angle given of 54.5° was later refined to 56°. Whether or not the molecules were static and disordered or precessing could not be concluded. Of the two molecular orientations proposed, it is extremely difficult to distinguish [Press and Huller, 1978].

2.4.3 δ-N_2

From the β phase, nitrogen transforms into the δ phase at 4.9 GPa. This phase is well known to possess a cubic structure with space group *Pm-3n.* In spite of this, the orientation of the molecules has been debated. Despite the similarities between O_2 and N_2 molecules, it is the only isostructural phase common to the two elements.

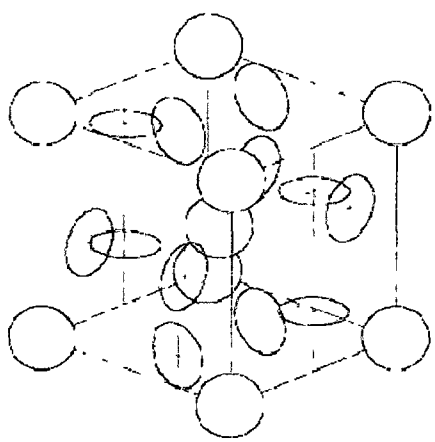

Figure 2.8: The structure of δ -N_2 The molecules on the Wyckoff 2a sites at (0,0,0) and (½, ½, ½) are spherelike disorder and the molecules on the Wyckoff 6d sites at (0, ¼, ½) possess disklike disorder [Mulder, 1998], [Stinton, 2009], [Mills, 1986].

The transition into the δ phase as a function of pressure at room temperature is apparent from the splitting of the Raman stretching vibron. The splitting into two modes signifies the two types of molecular disorder present. Cromer *et al* describes the structure of this phase to have spherelike and disklike disorder on different symmetry sites of the cubic lattice. The spherelike molecules exhibit spherical disorder on the Wyckoff 2a sites at (0, 0, 0) and (½, ½, ½) and the disklike molecules are on the Wyckoff 6d sites at (0, ¼, ½) [Stinton 1998], [Stinton, 2009], [Cromer, 1981]. The structure is shown in Fig.2.8.

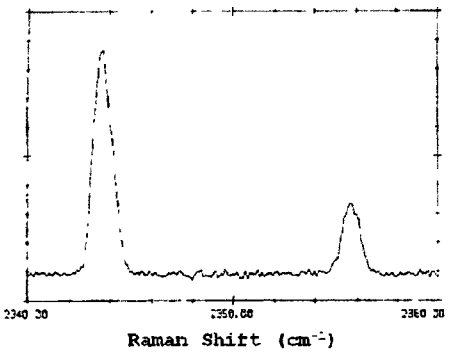

Figure 2.9: The Raman spectrum of the v_2 (more intense) and v_1 (less intense) modes of nitrogen in the δ phase. This spectrum is taken at 15 K and 5.5 GPa but appears similar at room temperature [Buchscbaum, 1984].

The two spherelike molecules on the a sites result in the v_1 band, and the six disklike molecules on the d sites give rise to the v_2 band of the Raman spectrum. As there are three times as many molecules occupying the 6d sites than in the 2a sites, the v_2 mode is about 3 times more intense than v_1 (Fig. 2.9) [Hellwig, 2001].

Several studies (Mulder, 1998, Belak, Westeroff and Feile, Stinton 2009) attempt to describe the structure of the δ phase by going beyond the time- and space-averaged XRD results (Fig. 2.10) and provide a depiction of the dynamic molecular orientation. Some of the studies proposed a preferred orientation for the spherelike and/or disklike molecules. These studies are summarized in Table 2.3, indicating which alignment, if any, is preferred for orientation of each type of disordered molecule.

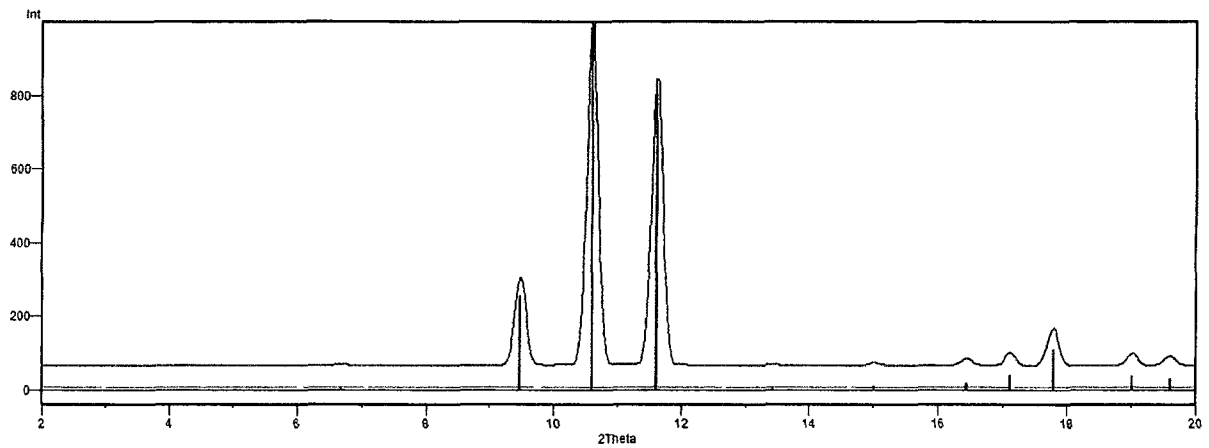

Figure 2.10: XRD pattern of δ-nitrogen at room temperature, generated based on the atomic positions and unit cell described by [Cromer, 1981] with λ = 0.509176 Å at 4.9 GPa.

Table 2.3: Dynamic Orientational Preferences of Molecules in δ-Nitrogen

Study	Orientational Preference	
	Spherelike Molecules	**Disklike Molecules**
Westeroff and Feile	-No preference: complete disorder	-Preference for 45° to faces of unit cell -Dynamic disorder caused by the low energy required to prompt rotation
Belak	-Possibly favours perpendicular or parallel alignment with faces of unit cell	-Possibly favours perpendicular or parallel alignment with faces of unit cell
Mulder	-Weakly prefers <111> direction	- Somewhat favours perpendicular or parallel alignment with faces of unit cell
Stinton	-Particularly avoids aligning with <001> direction	-No preference: disordered over many sites

Table 2.3: Orientational preferences proposed by [Westerhoff, 1996], [Belak, 1990] [Mulder, 1998], [Stinton, 1998], and [Stinton, 2009].

2.4.4 δ_{loc}-N_2

The existence of an intermediate phase between the δ and ε phases of nitrogen was first proposed during a Raman spectroscopy study by Scheerboom and Schouten, who noticed a subtle change of slope of the frequency of the v_1 and v_2 vibrons at 210 K around 6 GPa [Scheerboom, 1996] as shown in Fig 2.11.

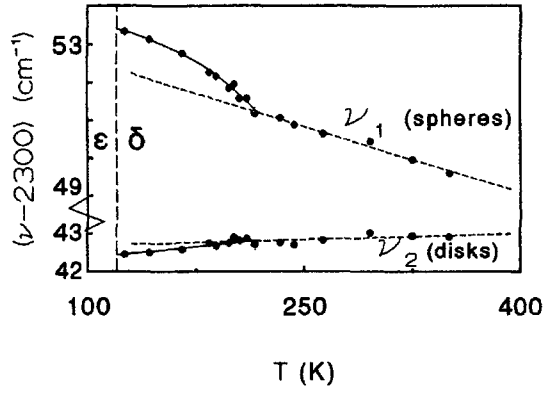

Figure 2.11: Frequency of Raman modes that indicate the existence of an intermediate phase between δ and ε phases [Scheerboom, 1996].

At that time, no structural change was noted in the stability range of δ nitrogen. In 1998, Hanfland performed an XRD study that confirmed the presence of a structural change when he observed the appearance of additional weak reflections (Fig. 2.12). The XRD pattern was clearly related to that of the δ phase, so this new phase was referred to as δ*, or δ_{loc} and described as a distortion of the cubic lattice of the δ phase (here, it will be referred to as δ_{loc}). He proposed a tetragonal unit cell with the a parameter extended to √2 of the δ lattice parameter, and c to be similar to an extrapolation of the δ phase, containing 16 molecules [Hanfland, 1998].

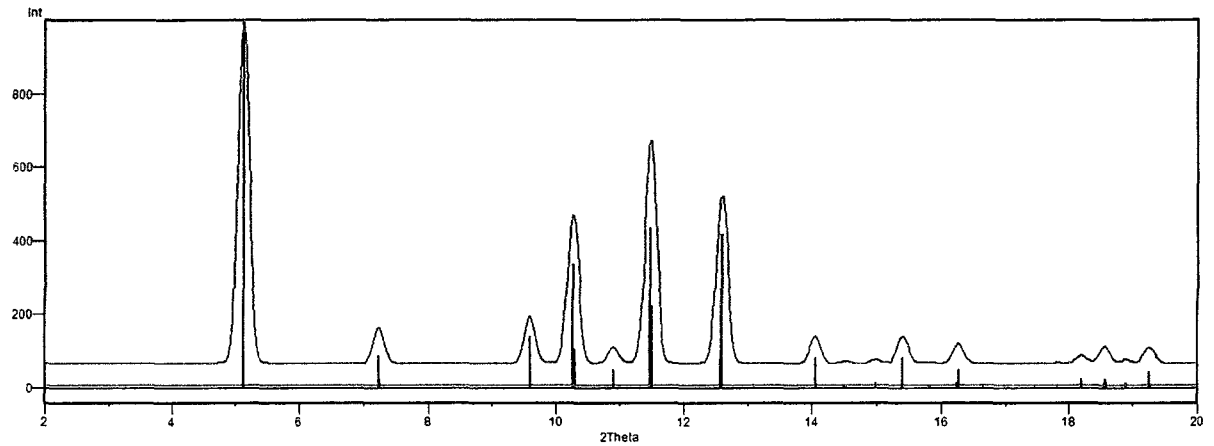

Figure 2.12: XRD pattern of the δ_{loc} phase generated based on the atomic positions and unit cell proposed by Stinton, 2009] with λ = 0.509176 Å at 14.5 GPa.

Different structures and space groups have been proposed for this phase in attempts to explain the number of Raman and IR-active modes as well as the XRD reflections observed. The model proposed by Hanfland [Hanfland, 1998] has been one of the more popular, and has been supported by Stinton [Stinton, 1998], [Stinton, 2009], and Hellwig *et al.* [Hellwig, 2001], to name a few. Other proposals include an expanded cubic lattice of 32 [Bini, 1998] or 64 [Mulder, 1998] molecules. These have been discounted by recent studies [Stinton, 2009] although very few XRD studies have been performed since that of Hanfland. The recent study by Stinton *et al.* predicts the structure of δ_{loc} nitrogen to be that of Fig. 2.13. Although such detailed information about the orientational order of the molecules can be obtained, Stinton *et al.* remarks that the question regarding the number of spectroscopic modes observed has not yet been answered and the proposed structures cannot account for this discrepancy [Stinton, 2009].

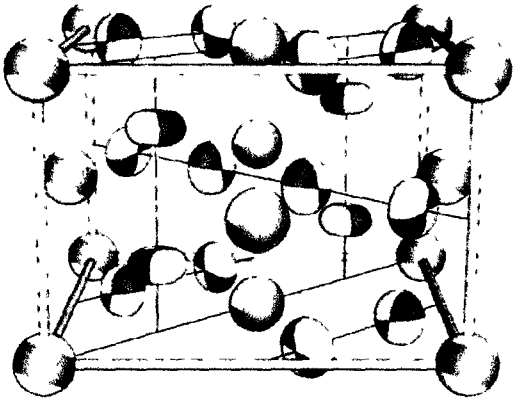

Figure 2.13: The structure of the δ_{loc} phase determined after performing extensive study on the orientational order. The molecules here possess the same disorder as in the δ phase the shaded areas represent the preference for orientation [Stinton, 2009].

2.4.5 ε-N_2

The ε phase of nitrogen, existing above 16 GPa at room temperature, can be described by the *R-3c* space group and a rhombohedral unit cell. The transition into this phase is evident based on the Raman spectrum, in which there is splitting of the v_2 mode [Hellwig, 2001].

The structure of the ε phase (Fig. 2.14) can be obtained from a distortion of the δ phase and moving the molecules into new positions with full order. The transition into the rhombohedral cell requires a distortion of the 90° angle of the cubic unit cell. At 16.3 GPa, the rhombohedral angle becomes 84.8° [Olijnyk, 1990]. The previously spherically disordered molecules in the δ phase become aligned along the body diagonal (111). The molecules that were previously described as having disklike disorder align on the face in the plane of the "disk", 45° relative to the normal of the face. These molecules rest at an angle θ_d to the normal of the disk, which depends on the angle of the rhombohedral cell [Mulder, 1998]. The XRD pattern for this phase is shown in Fig. 2.15.

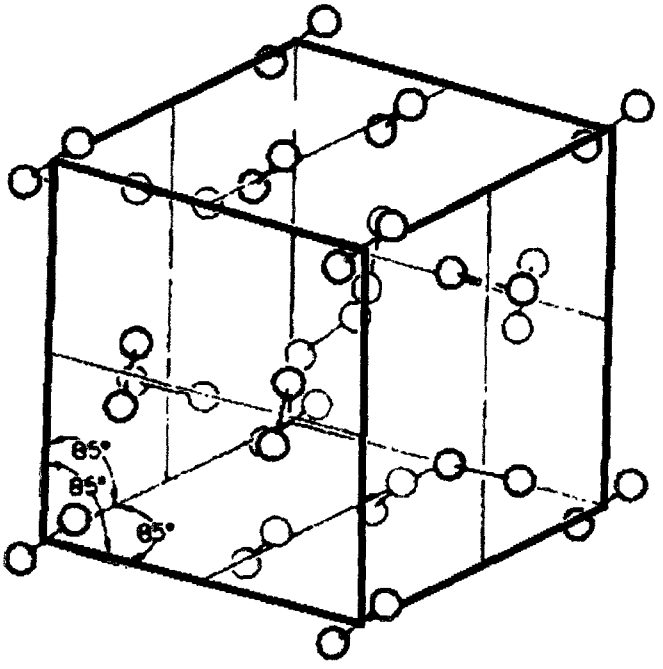

Figure 2.14: Structure of ordered ε phase [Mills, 1986]

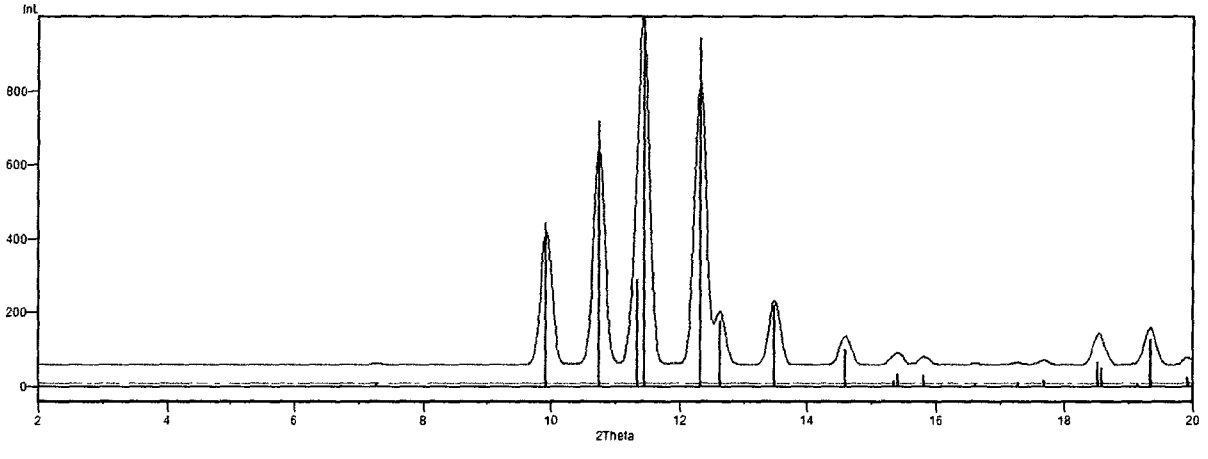

Figure 2.15: XRD pattern of ε-nitrogen generated from the atomic positions and unit cell given by [Mills, 1986] with λ = 0.509176 Å at 7.8 GPa and 110 K (the structure is basically the same at room temperature, with the lattice parameters and atomic parameters varying slightly).

2.4.6 Raman Spectrum of Solid Nitrogen

The Raman-active modes of solid nitrogen in the room temperature phases undergo multiple splittings, indicative of transitions into structures with different types of molecular order. The fluid and β-nitrogen Raman spectra display a single stretching mode with little difference in position, though the crystallization causes a sharper peak [Zinn and Schiferl, 1987]. The δ phase has a second mode, arising from the two different types of disorder in the structure. The difference in the Raman spectra of the δ and δ_{loc} phases is characterized by a change in slope of the Raman vibron over the transition pressure or temperature. The ε phase sees a splitting of the v_2 band [Schneider, 2992]. These features are summarized in Fig. 2.16.

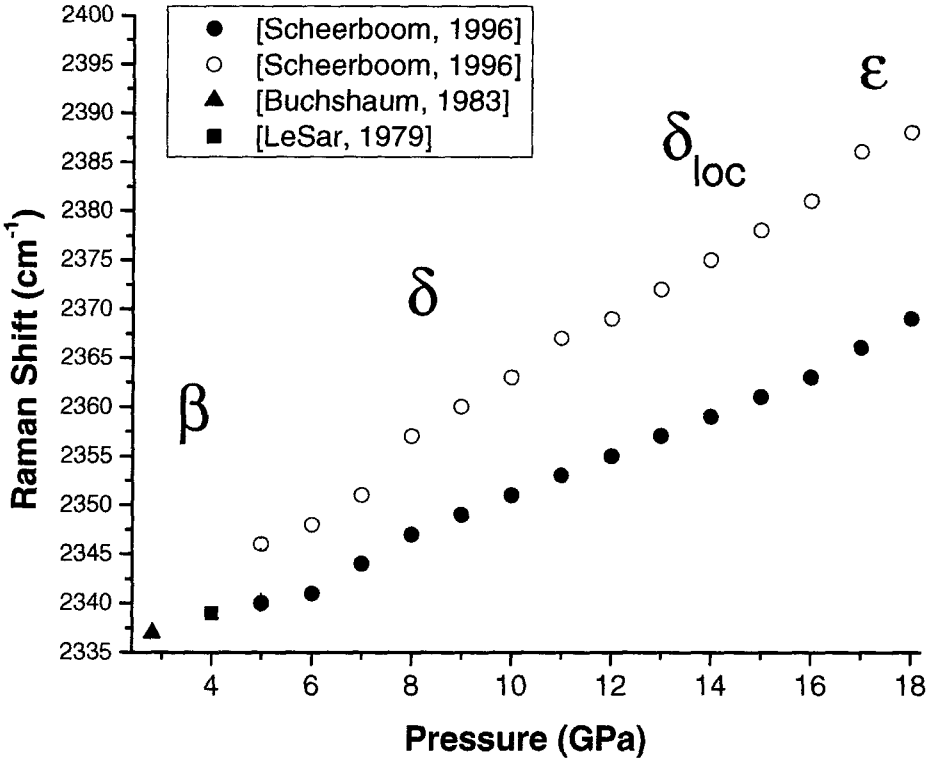

Figure 2.16: The Raman shift of the v_2 (solid symbols) and v_1 (hollow symbols) in the relevant pressure range. The splitting of the vibron in the ε phase occurs at higher pressures.

2.4.7 The Equation of State of Nitrogen

Fig. 2.17 shows the volume of solid nitrogen over the relevant pressure range from multiple sources. Since there is very little published data on the volume of the δ_{loc} phase, the values were extrapolated from [Hanfland, 1998] which states that the lattice parameters of δ_{loc} are related to δ by $a = \sqrt{2}a_\delta$ and $c = a_\delta$ and assuming 16 molecules per unit cell. A small molecular volume change occurs between each phase.

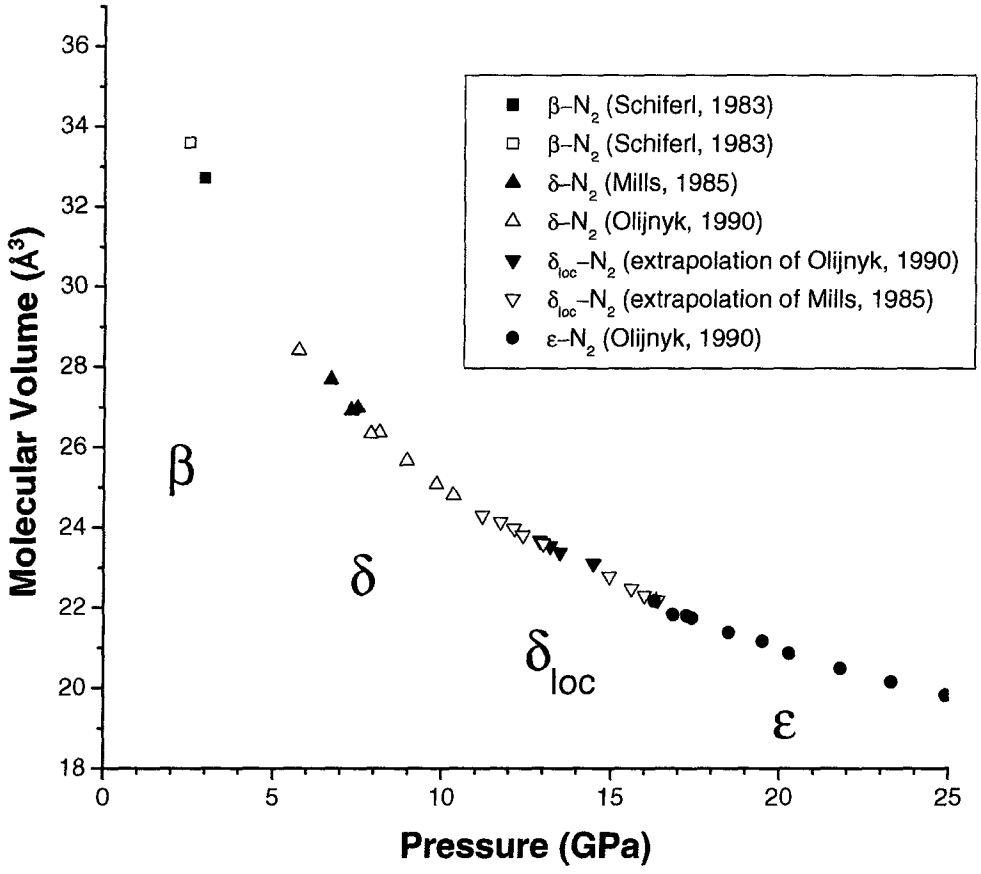

Figure 2.17: Equation of state of nitrogen. Note: the molecular volumes for the δ_{loc} phase were extrapolated from results for the δ phase with the relationship between the two phases and their lattice parameters proposed by [Hanfland, 1998].

2.5 The Solid Phases of Methane

Methane is the simplest hydrocarbon, and like nitrogen, possesses a large amount of polymorphism in its complex phase diagram. It was originally thought to possess phases similar to that of a noble gas due to its neutral charge and symmetry, causing it to be approximately "spherical". For this reason, the final high pressure phase of methane was predicted to be hexagonal close packed. However, it was found that only one low temperature phase was similar to a phase possessed a noble gas [Hebert, 1987] [Bini, 1997] and the complexity of its room temperature phases set it apart from this simple model.

Recent optical and XRD studies on solid methane have claimed to extend the knowledge of the room temperature phase diagram above 300 GPa. The study of methane at ultrahigh pressure is of great interest. Neptune and Uranus contain an abundance of methane and pressures at their center range from 600 to 800 GPa [Sun, 2009]. Other interests in methane are rooted in its high-hydrogen content and possible ability to acquire a metallic phase, although this was found to occur at pressures higher than current capabilities [Martinez-Canales, 2006].

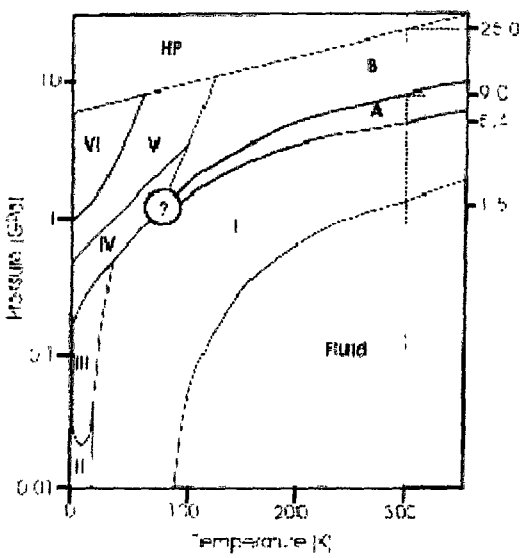

Figure 2.18: The phase diagram of methane [Maynard-Casely, 2010].

2.5.1 The Phase Diagram of Methane

Like nitrogen, much of the phase diagram of methane has been a subject of debate. In fact, only three of its phases have a structure that has been well-defined with complete atomic positions: the low temperature phases I, II and III [Maynard-Casely, 2006].

At room pressure, only phases I and II exist. Below 10 GPa and 100 K, phases III, IV, V and VI exist. The higher temperature phase A was originally thought to be an extension of phase IV [Hebert, 1987] and then later renamed phase A [Bini, 1997] when results could not provide adequate proof of the relationship, and the next higher pressure phase was set to B in the same study. The transition into phase B is sluggish, and the transition pressure is thus often described as a range. Above this phase is the HP (high pressure) phase. This is summarized by the phase diagram shown in Fig. 2.18 [Bini, 1997].

The room temperature phases of methane, A and B, are not well defined. Part of the difficulty in structure determination for the methane phases arise from the "bad" powders it seems to form. It has been noted in studies [Hazen, 1980], [Bini, 1997], [Fabre, 1982] that the transition into phase A creates a polycrystalline sample, and has a tendency of forming a poor powder rather than single crystals. A poor quality sample does not often result in obtaining a well-defined structure. It was only in 2010 that a structure for phase A has been proposed, with phase B still requiring more attention.

2.5.2 I-CH_4

From the fluid phase, methane transforms into phase-I at 140 K and 0 pressure, and at 1.3 GPa at 300 K. In this phase, methane crystals appear to have rounded facets, and are similar to what is observed with the rare gases. This implies complete rotational disorder of the molecules in this phase. Phase I corresponds to a face-centered cubic structure with space group *Fm3m* with one molecule in each unit cell [Hebert, 1987].

Hazen *et al.* performed the first XRD experiments on room temperature methane from 1.6 to 5.2 GPa. The features listed above were confirmed and the relative intensities of the diffraction patterns were published [Hazen, 1980]. These intensities were confirmed in a brief study performed to validate these findings [Maynard-Casely, 2009].

2.5.3 A-CH_4

Hazen *et al.* remarked that, when increasing the pressure above 5.2 GPa at room temperature, their methane samples became polycrystalline [Hazen, 1980]. This next phase along the 300 K isotherm was thought to be phase IV, which was also observed at low temperatures. Optical studies performed by Hebert *et al.* show a sudden change of slope at this transition in the Raman frequency of the v_1 and v_3 modes [Hebert, 1987]. In 1995, Bini *et al.* noted the lack of evidence relating phase IV to the phase observed at room temperature, and thus the room temperature phase is now referred to as phase A. The transition is easily identified using IR spectroscopy, as I-CH_4 exhibits no IR bands and one appears upon the transition into phase A [Bini, 1997].

The structure of phase A was originally proposed to be hexagonal close packed. This claim was based on spectroscopic measurements and the notion that methane could be described as a rare gas model, or at least a "bad" rare gas model. This model predicts the transition from a face centered cubic to hexagonal close packed structure at higher pressures [Bini, 1995], [Hebert, 1987].

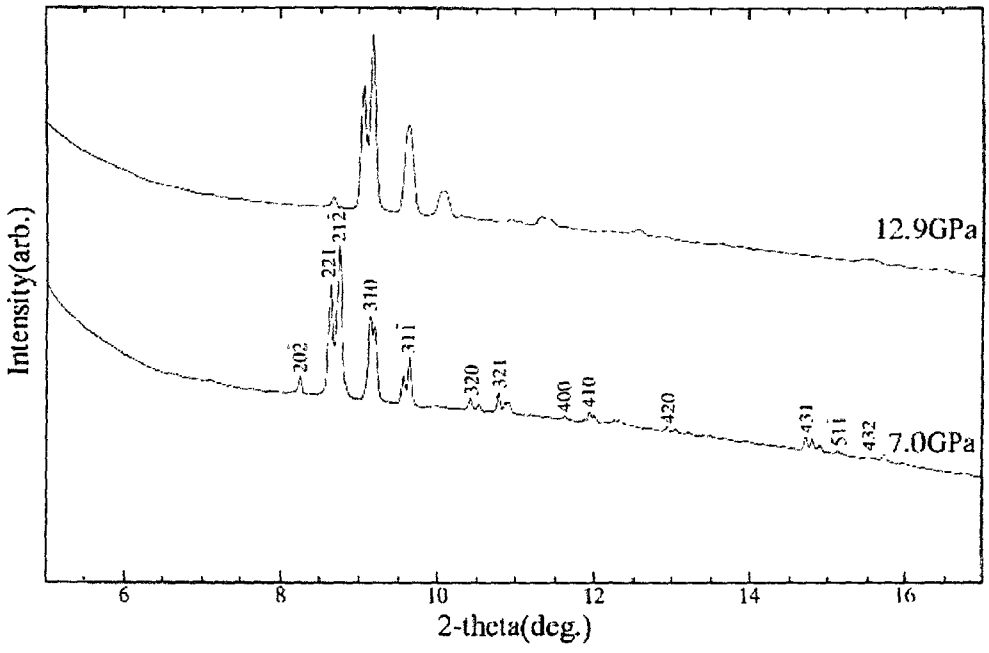

Figure 2.19: XRD patterns of methane in phase A [Nakahata, 1999].

The first structural study performed on phase A was done in 1999 when Nakahata *et al.* conducted XRD on methane at room temperature from 7 to 13 GPa (Fig. 2.19). They described this phase as possessing a rhombohedral structure with a = 8.643 Å and α = 89.40° at 7.0 GPa with 21 molecules per unit cell and possible space groups *R3, R-3, R32, R3m* or *R-3m* [Nakahata, 1999]. Other studies have verified the equation of state [Sun, 2009], [Umemoto 2002] however no structure had been suggested until quite recently.

After an intensive study using complementary single crystal XRD and neutron diffraction techniques, Maynard-Casely *et al.* was able to describe the unit cell of phase A as a strongly distorted version of the face-centered cubic phase I. In phase I, the cubic close packed unit cells can be broken down into layers, which are stacked together to form the overall structure (Fig. 2.20). Phase A can be seen as distorted layers that are stacked together to form the 21 molecule structure (Fig. 2.21). This study also confirmed the *R3* space for this structure [Maynard-Casely, 2010].

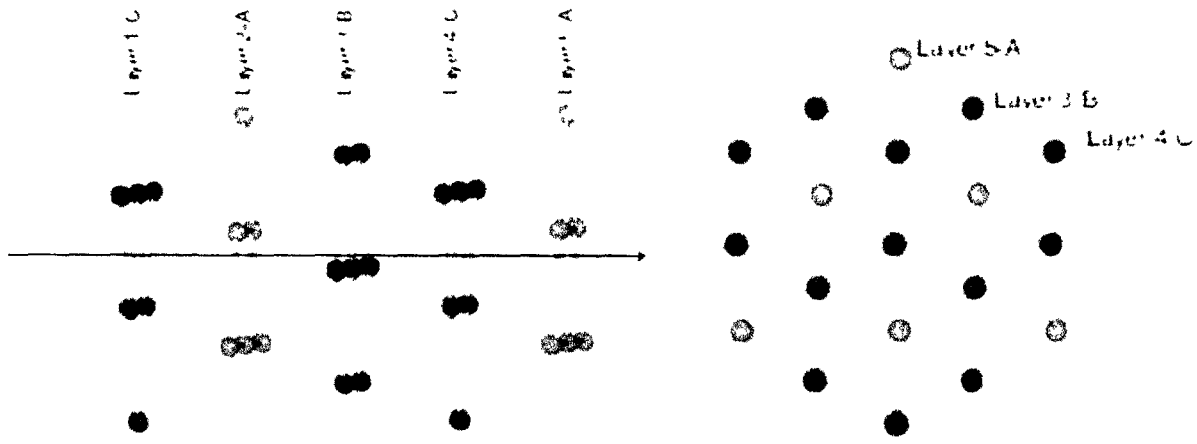

Figure 2.20: (Left) A sequence of layers make up the close packed structure of phase I, shown (right) as viewed through the layers [Maynard-Casely, 2010].

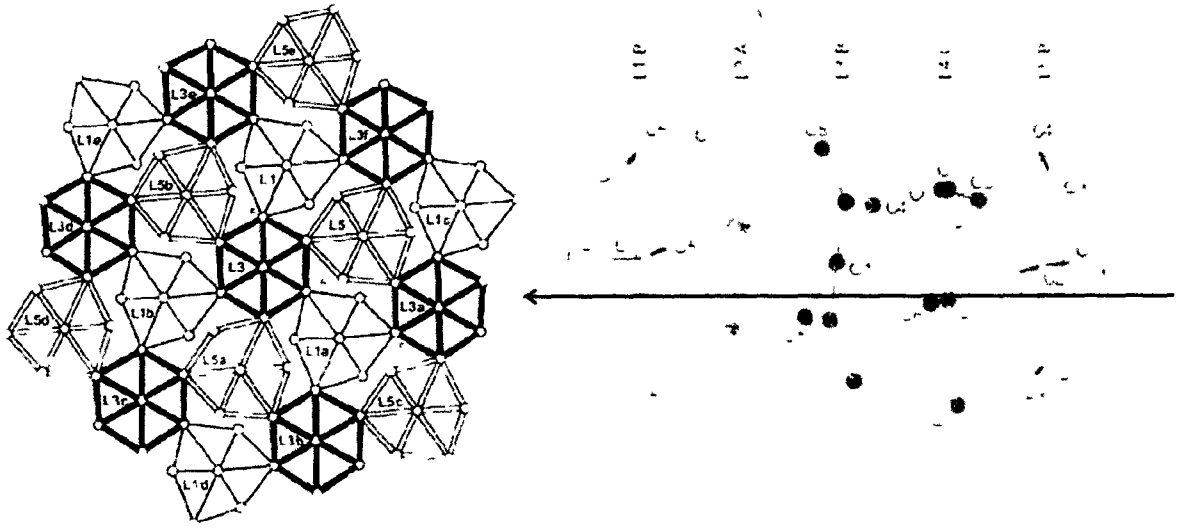

Figure 2.21: The structure of phase A can be described as a distortion of the stacked layers of the close packed cubic structure (right). This results in the rhombohedral lattice (left, as viewed from θ to α) [Maynard-Casely, 2010].

2.5.4 B-CH_4

After a "sluggish" phase transition, methane transforms into phase B. Phase B was described as phase VII [Hebert, 1987] and later renamed, like phase A, to differentiate it from the low temperature phases [Bini, 1995]. It was first identified by the splitting of the v_1 Raman mode around 12 GPa [Hebert, 1987]. It was noticed that the transition has a slow onset and is subject to a great deal of hysteresis, remaining down to 6.6 GPa upon decompression. It was found that the Raman modes shift linearly with pressure up to 25 GPa [Bini, 1995].

XRD measurements were performed on this phase by Umemoto *et al.* in 2002. They suggested that phase B would contain 21 molecules per unit cell based on volume and assigned it to a cubic lattice with a = 7.914 Å at 16.9 GPa. This phase was consistently observed up to 25 GPa, at which a transition into the HP phase occurs [Umemoto, 2002].

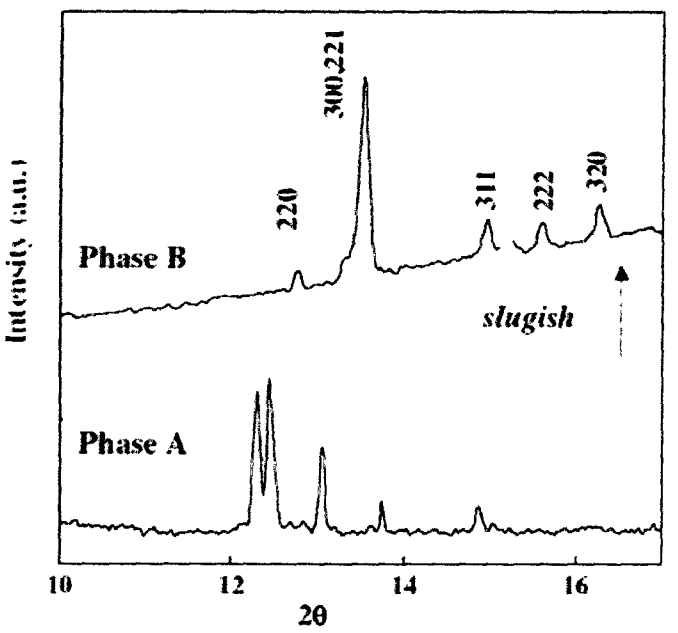

Figure 2.22: XRD patterns displaying the A to B transition adapted from [Hirai, 2008]; λ = 0.6198 Å. The XRD pattern of the B phase is displayed at 22.4 GPa.

The structure of phase B is not well known and there have been few studies that present ideas about it. To describe the A to B transition, Hirai *et al.* suggest an intermediate phase [Hirai, 2008]. However, this was discounted by following works [Sun, 2009]. Maynard-Casely suggested that phase B must be modified to an extended cubic lattice, proposing a lattice parameter that is √2 times the previously published results. This is based on the appearance of very weak diffraction peaks, made possible by carefully ensuring a good quality sample. In this larger unit cell, a body-centered cubic unit cell with space group *I23, $I2_13$, Im-3, I432, I-43m* or *Im-3m*, that could hold 56 to 64 molecules [Maynard-Casely, 2009]. No other studies have been performed to debate or confirm the claim of a larger unit cell.

2.5.5 Raman Spectrum of Solid Methane

The methane molecule exhibits several modes: the fully symmetric stretching mode v_1, the doubly degenerate v_2, the triply degenerate v_3 (the antisymmetric stretching mode) and v_4. This discussion is restricted to v_1 and v_3, as v_2 is not strongly affected by pressure and v_4 is overpowered by the first-order diamond peak [Hebert, 1987], [Bini, 1995]. The I-A transition is marked by a change of slope of the frequency of vibration for both v_1 and v_3 modes over pressure. Between phases A and B, splittings occur for both modes. The v_1 mode develops a shoulder on the low frequency side and the v_3 is split into at least three bands. The weak intensity and broadness of the v_3 modes make it difficult to distinguish the number of bands present and their specific position [Bini, 1995]. The frequencies of these modes are displayed in Fig. 2.23.

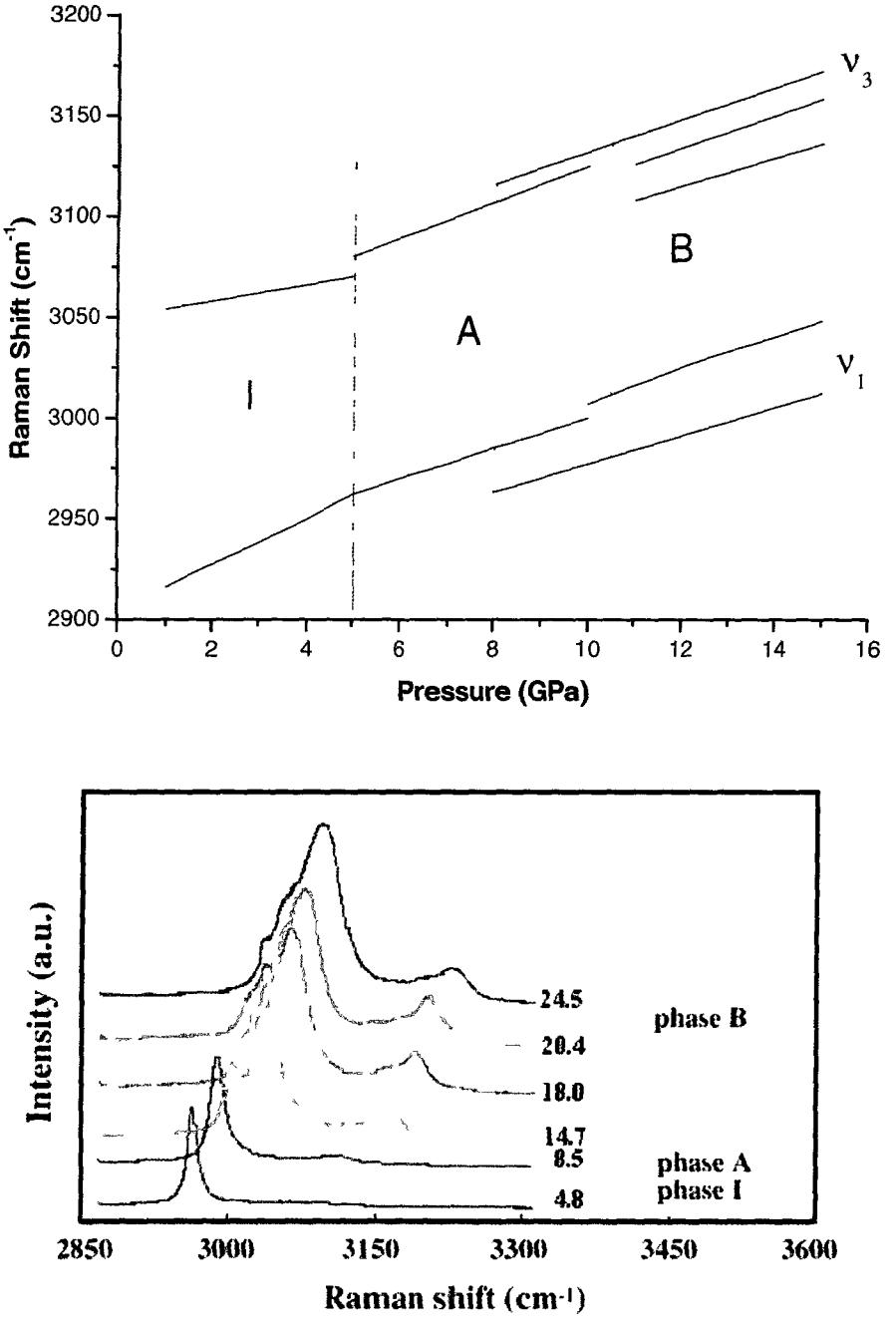

Figure 2.23: (Top) The Raman shift of the ν_1 and ν_3 modes of pure methane plotted over pressure. The dashed lines outline the region affected by hysteresis [Hebert, 1987]. (Bottom) The Raman spectra are shown for each of these phases [Hirai, 2008].

2.5.5 The Equation of State of Solid Methane

The molecular volume of methane plotted over the relevant pressure range at room temperature is shown in Fig. 2.24. The hysteresis between the A to B transition is represented by the shaded box. The dashed lines designate the published transition values [Maynard-Casely, 2009].

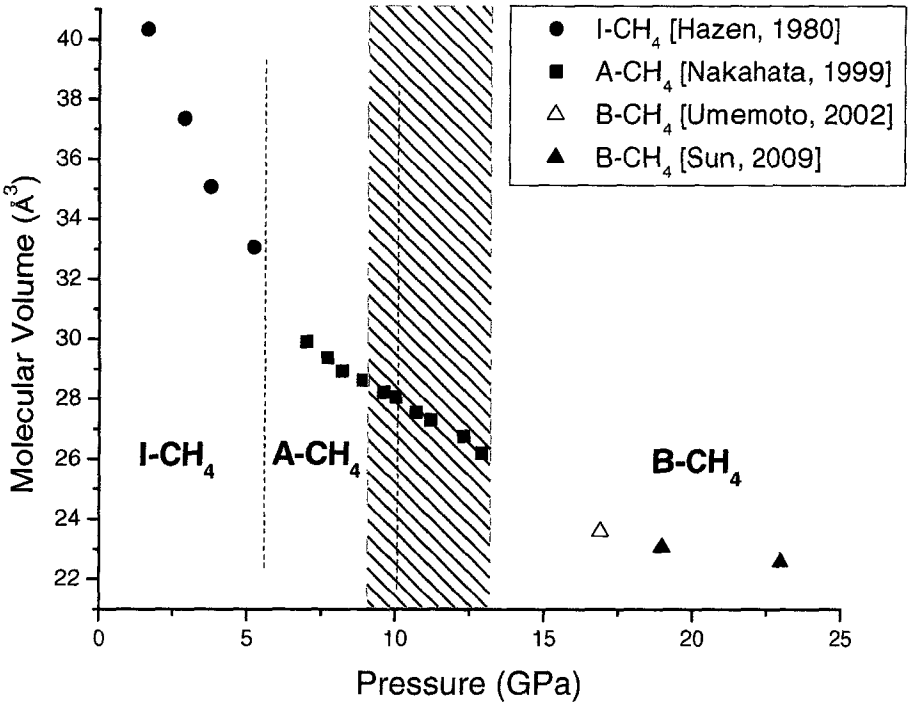

Figure 2.24: The equation of state of methane. The box represents a transition greatly affected by hysteresis, making it difficult to define the exact phase boundary.

3. Experimental Techniques

3.0 Introduction

A phase diagram provides a summary of all of the structures present inside a sample at a given set of thermodynamic conditions. Hence, construction of a phase diagram requires varying the thermodynamic conditions, and in this case, concentration of the constituents to map out the boundaries between existing phases, and identify the crystalline structure of all phases present. There are several techniques available to fulfill these tasks. This section focuses on the use of Raman spectroscopy and powder X-ray diffraction (pXRD) in order to define phase transitions and structures as a function of pressure and concentration at a given temperature.

Raman spectroscopy probes the vibrational modes of the solids studied. Vibrational modes include the molecular and lattice vibrations of a molecular solid. Changes in the condensed state can be reflected at the molecular level and detected by changes in the corresponding Raman spectrum. Raman spectroscopy, although a powerful tool for studying binary mixtures, is insufficient to fully define the structure of a phase. A structural study is also necessary. In this work, pXRD using synchrotron radiation is employed.

Limitations (described in 3.4.3) imposed by the use of the DAC requires high energy (short wavelength) monochromatic X-rays for diffraction studies. Synchrotron radiation provides this as well as other advantages. XRD using synchrotron radiation allows one to describe the structure with a unit cell and lattice parameters, space group and atomic positions. It also allows one to assess the microstructure of the sample such as preferred orientation and crystallite size. This requires sufficient quality of data obtained through careful sample preparation and XRD images taken under the best conditions.

Raman spectroscopy and pXRD (in this work, all XRD experiments are performed on a powder sample) are discussed in sections 3.1 and 3.2, respectively, describing the technique and its development for studying samples subjected to high pressure in the DAC. Section 3.3 includes the procedures associated with sample preparation for these techniques, including specifications of the DACs used.

3.1 Sample Preparation

A total of 23 samples of varying concentrations were studied in the effort to produce the nitrogen-methane pressure-concentration phase diagram. The quality of results obtained from Raman spectroscopy and, in particular, pXRD strongly depends on the quality of the sample. For pXRD, a good quality powder entails one that contains a sufficiently large amount of randomly oriented small (on the order of μm) crystallites which do not align with a preferred orientation. For optimum results, the largest possible volume of sample should be used. Hence, the sample preparation, loading procedure and growth in the DAC is of great importance for the success of these studies.

Prior to sample loading, the DAC must be prepared. The alignment of the diamond anvils is critical. This is accomplished previously and it suffices to state that the diamonds are well mounted with the tables and culets of each anvil parallel to each other. The parallelism is measured to within an angle of 1-2 mrad as assessed using interferometry. The sample loading procedure commences with the preparation of the gasket. The gasket material must be indented, drilled, and mounted on the cylinder anvil to serve as a compression chamber. A ruby microsphere is placed inside the drilled hole for pressure calibration. A liquid mixture of nitrogen and methane is prepared and then loaded cryogenically into the DAC. The details of these procedures are described in more detail in the following sections.

3.1.1 The DAC

In this project, two types of DACs were used; the membrane and the "three-pin" cell. These DACs were selected for their ability to withstand loading at liquid-nitrogen temperatures and their ability to produce pressures in the desired range.

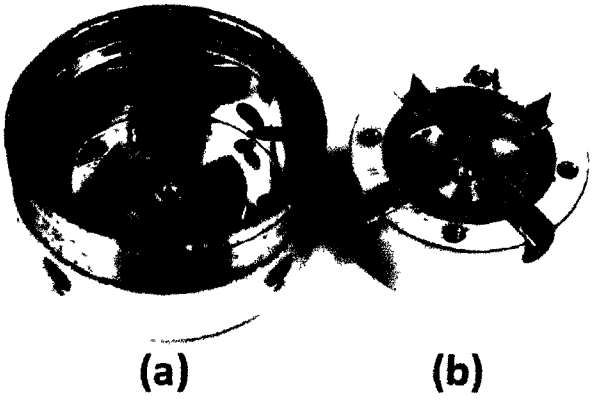

Figure 3.1: The open membrane DAC: (a) is the cylinder and (b) is the piston of the cell.

The membrane DAC consists of a piston and cylinder that make up the cell body. A diamond anvil is mounted on each half of the cell body, which are precision-machined out of strong, stainless steel (see Fig. 3.1). The flat diamond culets have a diameter of 300 μm. The generation of pressure is accomplished by placing the piston into the cylinder and turning four screws to bring the piston diamond anvil into the cylinder diamond anvil in a controlled manner.

In the piston and cylinder, the diamond anvils are mounted on seats of different materials to provide versatility in the study of a sample contained within the DAC. On the piston side, seen in the left frame of Fig. 3.2, the seat is made of tungsten carbide. This material is very strong and rigid, so that it can provide support and still allow for a large optical opening for visual and spectroscopic measurements. The right frame of Fig. 3.2 shows the cylinder side. The anvil on the cylinder side is mounted on a beryllium hemispherical seat. Although beryllium is not as hard as tungsten carbide, it is nearly transparent to hard X-rays (high energy X-rays), and thus, it does not hinder XRD experiments.

In order to make adjustments to the alignment of the diamond anvils the seats must allow translational and rotational motion. The hemispherical shape of the piston anvil seat and the flat shape of the cylinder anvil seat allow for the necessary motion in alignment. Metallic holders securely fasten the anvils to their respective seats and remain stable, even at low temperatures.

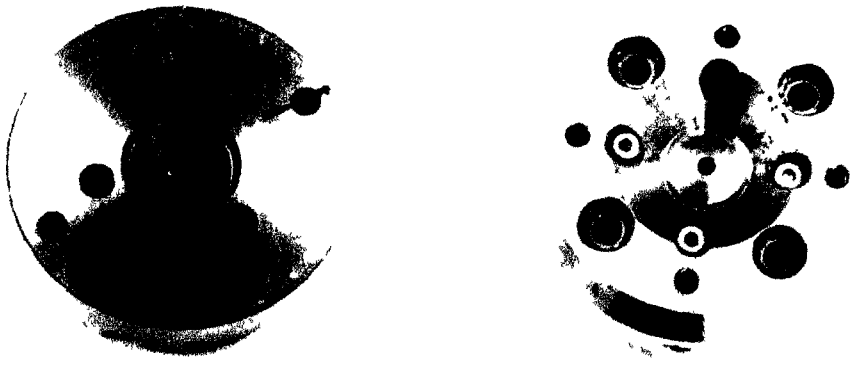

Figure 3.2: (Left) The piston side and (right) the cylinder side of the membrane DAC with a large opening for optical measurements and XRD measurements, respectively.

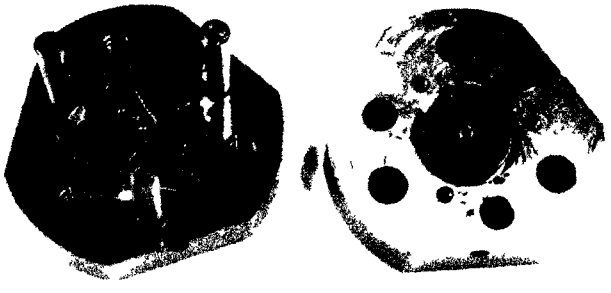

Figure 3.3: The three-pin DAC. A prepared metal gasket is mounted on the half shown on the left.

The second type of DAC used, the three-pin cell, is shown in Fig. 3.3. This DAC has pegs on one side that can be inserted into holes on the other side, and three screws that bring the anvils together to generate pressure. When put together, the DAC appears as in the right frame of Fig. 3.4. As in the membrane cell, the openings on each side of the cell are different; the larger aperture

provides an opening for visual and spectroscopic measurements and the smaller aperture provides an opening for XRD measurements since the seat surrounding the aperture is made of beryllium.

Figure 3.4: (Left) One side of the three-pin cell has a small opening and three pegs which can be inserted into the (right) other side of the three-pin cell, which has a larger opening and three holes for pressure screws.

The membrane cell has several advantages over the three-pin cell. First, the opening for optical measurements is much larger in the membrane cell. Second, the tight-fitting piston-cylinder design of the membrane cell enables the generation of higher pressures than the three-pin cell. This design also promotes the production of high quality samples, as the three-screw design of the three-pin cell often causes the sample to shift and the compression chamber to distort.

3.1.2 Gasket Preparation

The majority of samples studied in this project were contained in full-hard ANSI T301 stainless steel gaskets, with an initial thickness of 250 μm. Some of the later samples studied were contained in rhenium gaskets with the same initial thickness. The first step in gasket preparation is the indentation of the gasket material. A rectangular sheet of gasket material is placed over the diamond on the cylinder side of the cell. Putty is previously placed on either side of the diamond to

add support to the gasket sheet and hold it in place, as in Fig. 3.5. The piston is then inserted into the cylinder and pressed down to apply a small amount of pressure. The gasket sheet is then indented by driving the diamonds into the material by tightening the pressure screws.

Figure 3.5: The gasket sheet in the center, supported by putty, is placed over the cylinder anvil. Inserting the piston and applying pressure causes the extrusion of the gasket material over the sides of the culets, resulting in an indentation due to the plastic formation of the material.

The gasket material extrudes around the diamond culet and becomes plastically deformed. The extrusion can be monitored through one of the anvils using a suitable microscope, as in Fig. 3.6. The diameter of the extrusion is measured in order to obtain the gasket thickness, a procedure which has been previously calibrated. After the desired thickness is reached, the gasket sheet is removed from the cell and the actual thickness is measured with a micrometer to within 1 μm. Typical final gasket thicknesses used in this project range from 80 to 150 μm. One sheet of gasket material is often indented 3 – 5 times across the sheet. The indentation of the gasket material allows for it to be easily mounted on the cylinder anvil, as well as hardens the material through strain hardening as it is reduced to the desired thickness. Furthermore, the extrusion of the gasket material provides radial support to the culets.

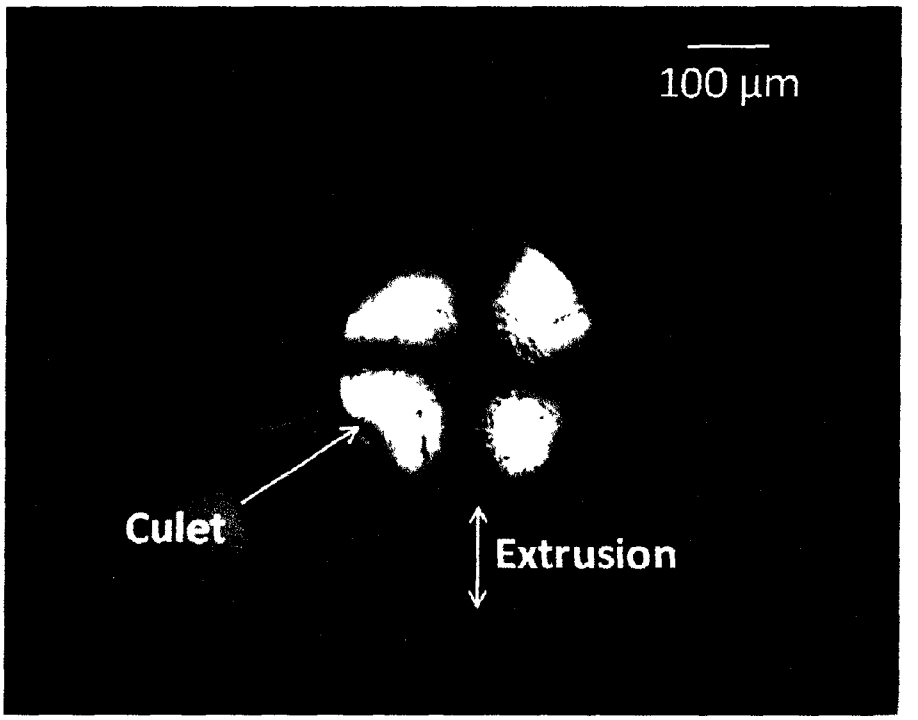

Figure 3.6: Extrusion of gasket over the diamond culet. In this figure, a 16-facet diamond anvil is indenting a rhenium gasket. Typically, in this work, 8-facet diamond anvils are used. The final thickness of the gasket under the anvil culet is estimated from the extent of the extrusion.

Each indentation must then be precision drilled (Fig. 3.7). The precision drilling is accomplished by using tungsten-carbide bits for stainless steel. Rhenium gaskets are drilled with a micro-spark erosion device. The drilled hole becomes the compression chamber, which holds the sample. The compression chamber must hold the sample in place under the force of the diamonds as well as provide more-or-less uniform stress in the radial direction as the diamonds apply axial stress along the load axis. The larger the hole, the larger the potential sample volume is for a given thickness. However, this increases the possibility that the compression chamber will shift away from the center upon the application of pressure, resulting in the loss of the sample. The size is thus chosen as a compromise between volume and constraining the sample. A typical compression chamber size should be about one third of the culet size.

The compression chambers used in this project range in diameter from 90 to 135 μm. It is typical to drill a 150 μm hole, then apply additional pressure by pressing the diamonds on the

seated gasket. This can reduce the hole diameter by the desired amount and cause additional hardening of the gasket material. A clean, well-centered hole drilled in one of the indentations is chosen as the compression chamber for the sample. An example of the prepared gasket is shown in Fig. 3.7.

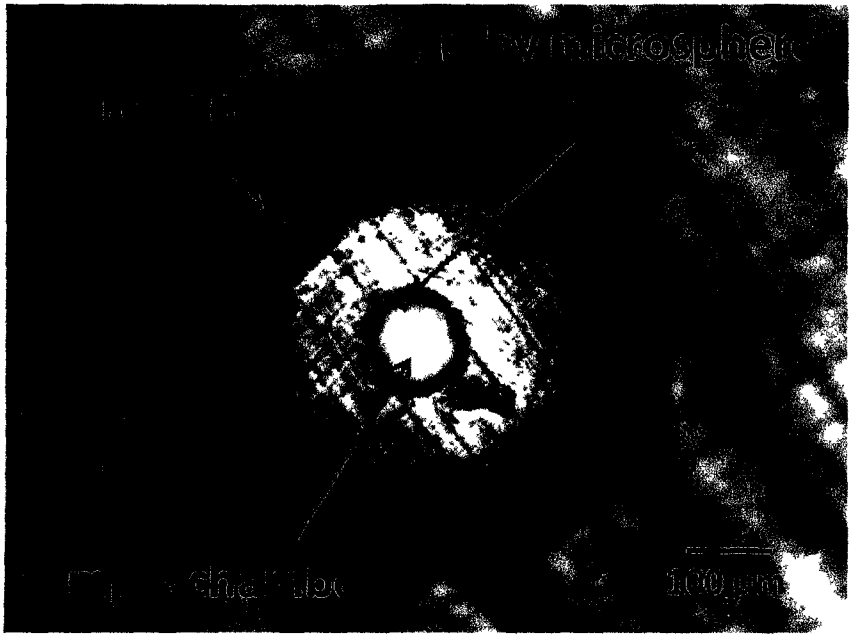

Figure 3.7: A prepared rhenium gasket. The ruby microsphere is between 5 and 15 μm in diameter. In this case, the compression chamber is not perfectly centered on the anvil culet.

Although most of the samples studied in this project were prepared with stainless steel gaskets, rhenium gaskets were used in the last samples. Rhenium was used in attempt to achieve higher pressures, as it is a stronger metal. The compression chambers in rhenium were about 90 μm in diameter and 100 μm in thickness.

3.1.3 Pressure Monitoring

A ruby microsphere of 5 - 15 μm in diameter is placed inside the compression chamber for in situ pressure monitoring using the calibration of equation 2.1 from section 2.1.4. The indented and drilled gasket is mounted on the cylinder anvil, supported by the putty, and the ruby microspheres are directly placed into the hole prior to loading. Two ruby microspheres are used since loading liquid mixtures may result in flushing one of them out. The ruby microspheres are moved from a slide using a thin needle, monitored under a microscope, into the compression chamber. Once placed, luminescence is measured to obtain the ambient pressure wavelength of the R_1 line, designated as λ_o.

The use of a ruby microsphere assumes only a small fraction of the sample space. It is ideal to have the ruby microspheres outside of the center of the sample, which is often used as the focus for spectroscopic and XRD measurements, while avoiding direct contact with the edge of the compression chamber. When the sample is compressed, the compression chamber distorts, shrinking or expanding in response to the applied pressure. If the ruby microsphere is in contact with the edge it is possible that the distortion causes the ruby additional compression or buries the ruby microsphere under the gasket material. This results in the loss of the pressure calibrant's integrity.

3.1.4 Loading Procedure

After the gasket containing the compression chamber is mounted and ruby microspheres are inserted, the piston is placed into the cylinder so that the diamonds are approximately 1 mm apart and the cell is ready for loading. Liquid methane is produced by flowing methane gas (99.95% pure, Linde Gases) into a flask, cooled in a bath of liquid nitrogen. The flask is pre-cooled, so when there is a sufficient density of methane gas in the flask, it condenses into liquid. The flask is partially sealed by a rubber stopper. The stopper has a tube inserted into it to allow for the inflow of gas

from the methane gas cylinder and a small vent to prevent pressure build up inside. The gas flow is shut off after the desired amount of liquid methane is produced, generally 150 – 250 mL, and the stopper is replaced by one that is solid to prevent contamination from the liquid nitrogen bath.

After the methane is liquefied, the glassware used for holding and measuring the mixture is flushed with liquid nitrogen and kept in a nitrogen bath for cooling. The DAC is also cooled. The DAC can be moved safely in and out of a nitrogen bath by inserting a screw into the side of the cell and clamping a "vice grip" onto it. It is important that the cell is not placed in liquid nitrogen below the opening, as the ruby microspheres may be flushed out by the boiling liquid (the boiling results from contact with the room temperature DAC).

After the glassware is sufficiently cooled, liquid methane and nitrogen are measured using a graduated cylinder and mixed in a Pyrex bowl sitting in a nitrogen bath. The pre-cooled DAC is then transferred into the liquid mixture so that the opening is completely immersed. This requires a total volume of 100 mL to 200 mL. After the boiling slows, two pressure screws in the DAC are tightened using a hexagonal key, trapping the mixture. The screws are further tightened to ensure the liquid mixture has solidified and that sufficient pressure is applied to keep the sample from melting as the DAC warms to room temperature.

The compression chamber is observed through the microscope to ensure that a sample is present and sufficient pressure has been applied. If the compression chamber has shifted significantly towards the edge of the culet or has been reduced to a small fraction of the desired size, the sample is re-loaded. Ideally, the sample is well centered and circular (indicating that the gasket material has not started to run or collapse). The cell is placed inside a helium environment to discourage frost accumulation on the optical openings and it is carefully monitored under the microscope as it warms back to room temperature. Loading pressures are generally a few GPa. With this well-practiced procedure, the sample loading success rate is around 80%.

3.1.5 Sample Concentration

Sample concentration is based on the amount of nitrogen in the N_2-CH_4 mixtures by volume. This defines the convention used to describe concentration throughout this thesis. This concentration can be roughly obtained using the measured volume of the liquids that are poured into the mixture. Unfortunately this method is associated with several possible errors. These errors provide a large uncertainty range, estimated to be about ±10%. These errors are discussed below after which, a more accurate concentration measurement technique is presented.

Methane liquefies at 110 K, solidifying at 90 K [Hebert, 1987] and liquid nitrogen boils at 77K. With the glassware in a bath of liquid nitrogen, it often freezes the methane, making it difficult to determine the exact amount of liquid poured into the mixture. The different boiling temperatures of nitrogen and methane also cause a potential issue in concentration determination. To avoid additional boiling, liquid nitrogen is always poured into cooled liquid methane. Although the glassware is also pre-cooled to minimize boiling, the ambient conditions surrounding the loading equipment causes inevitable boiling. When glassware is removed from its cold bath to measure or pour the liquids, it heats up fairly quickly and unequal boiling of the components occurs. When producing the mixture, nitrogen is poured into the liquid methane, which has been cooling to liquid nitrogen temperature. The mixture has a boiling temperature that is in between the boiling points of the components and which is dependent on concentration. It should be noted that liquid nitrogen and liquid methane are highly miscible and solid methane dissolves readily in liquid nitrogen.

More problems in concentration arise from the procedure used for preparing liquid methane. The use of a nitrogen bath for condensing the methane gas causes contamination in the resultant liquid, as these liquids are highly miscible. It turns out that methane picks up a large amount of nitrogen vapour as the cold bath boils off. This effect is emphasized when multiple loadings are performed with the same batch of liquid methane since, with time, more nitrogen contamination occurs. Thus, it is not possible to solely rely on the measured volumes in order to describe the sample concentration.

When Raman spectroscopy is performed on a mixture of nitrogen and methane, the characteristic stretching vibrations (vibrons) for the nitrogen and methane molecules present in the

sample can be observed. The relative intensity of these vibronic peaks at a given pressure depends on the abundance of that molecule in the sample (Fig. 3.8). This can be used in order to determine the concentration more accurately. The peak intensity ratio of the Raman v_2 mode for nitrogen and v_1 mode for methane was calculated for all samples over each pressure studied with Raman spectroscopy. This assumes that the Raman scattering cross sections for both molecular species are independent of pressure, as observed in Fig. 3.9. The results have been plotted and used for calibrating the concentration.

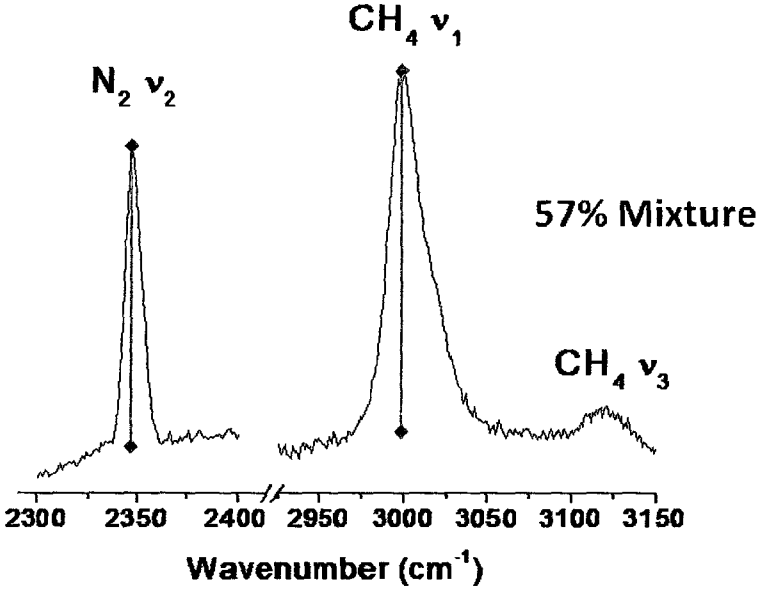

Figure 3.8: A Raman spectrum of a 57% nitrogen-methane mixture displaying the vibrons of nitrogen and methane used for determining the concentration from the intensity ratio.

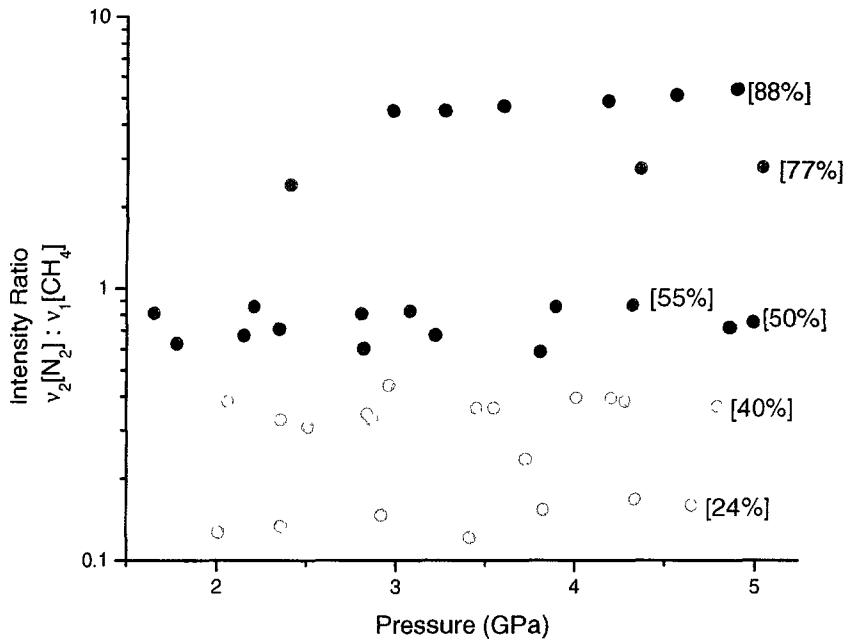

Figure 3.9: The plot displays the intensity ratio over pressure for some nitrogen-methane mixtures. In the pressure range shown, up to 5 GPa, the ν_2 mode of nitrogen and ν_1 mode of methane are single modes. Above this pressure, splitting occurs (and thus the peak intensity is based on the superposition of two peaks, making direct comparison more difficult). Note: a logarithmic scale is used for the intensity ratio.

Since the absolute intensity of each peak also depends on things like the sample volume and laser power, this method can offer a relative comparison. In order to use the intensity ratio as a concentration monitor, one must assume that some of the measured volumes provide an accurate concentration. The other concentrations are estimated relative to those calibration points.

The loadings of five selected samples were done quickly and carefully to minimize the effects of unequal boiling and nitrogen contamination, and were assumed to have an accurate concentration. The intensity ratios of these samples were plotted over the pressures studied. These plots were fit to both a linear and exponential function, and parameters were used to formulate functions that could deliver the pressure if given the intensity ratio. The ratios of all other samples were used to determine a concentration by averaging the results from each calibrating parameter. The resultant concentrations were reasonable based on their relative positions in the intensity ratio vs. pressure plot. The error for this technique is about ±5%.

3.1.6 Sample Loss and Experiment Termination

There are several reasons the study of a sample must be terminated. These are the results of problems with the DAC itself, gasket failure, or the loss of the ruby or loss of the sample.

The DAC can fail in several ways. The seats may no longer be able to withstand the necessary stress associated with the use of the DAC. The anvils may become cracked or the surface of the culet may develop chips or small craters. Improper alignment of the faces can cause the sample to be lost by producing a lower pressure area in the compression chamber through which the sample can escape, or by inducing the translation of the gasket.

Under compression, the gasket can shift or distort. Shifting can translate the sample space toward the edge of the culet. Once the sample can move outside of the area on which pressure is applied, it can escape. Nitrogen and methane change into the gaseous state when the pressure is lowered and thus lost quickly. The sample is more likely to escape if the diamond culet contains chips, particularly near the edge. The distortion of the compression chamber also puts the ruby at risk of loss or being confined to areas of higher or low compression. The study of the sample should not continue without proper pressure calibration.

The maximum pressure achieved depends on the DAC specifications: the size of the culets, gasket material, compression chamber dimensions and the sample itself. Assuming the proper preparation of the DAC, as described in sections 3.1.1 and 3.1.2, pressures of 15 GPa are routinely produced for a well-centered symmetric sample. Attempts were made to exceed this value by using rhenium gaskets, a stronger metal, and reducing the sample diameter slightly. This was unsuccessful, and pressures above 16 GPa were not generated. To obtain substantially higher pressures, it may be necessary to select diamonds with smaller culets. Higher pressures may also require the use of a smaller sample volume. Unfortunately, this reduces the signal achieved for the different measurement techniques.

Finally, pressure cycling may induce the loss of a sample. The gasket material becomes plastically deformed and the sample space is often gradually reduced with each pressure increase. After many pressure changes and cycles, the sample can become unusable based on the remaining volume.

3.2 Sample Inventory

In order to construct a pressure-concentration phase diagram, it is necessary to prepare multiple mixtures and study them over the appropriate thermodynamic range. Table 3.1 describes the samples prepared for this project. It includes a range for which Raman spectroscopy and pXRD were performed to give an idea of how each sample contributed to the phase diagram. It is clear that the concentration measured by volume is often inaccurate compared to the corrected relatively determined concentration (using the technique explained in section 3.1.5).

The pressure range for which each sample was examined is based on a number of factors: the reliability of the ruby microsphere as a pressure calibrant, and the size, position and distortion of the compression chamber. In general, a well-prepared sample with a stainless steel gasket using the particular membrane cells described should allow for the study of up to 16 GPa. Using the three-pin cells, the maximum pressure is often somewhat lower, about 13 GPa.

Over the course of this research, slight changes to the sample preparation were made to improve sample and data quality. One notable change was the amount of sample contained in the compression chamber. The samples (NMe200 – NMe600) were originally prepared with a compression chamber approximately 90 μm thick and 100 μm in diameter. To acquire a better signal in Raman spectroscopy and XRD measurements, this size was increased to 120 μm and 135 μm, respectively.

Table 3.1: Sample Inventory

Series	C[Vol]	C[Raman]	Raman Studies (GPa)	XRD Studies (GPa)
NMe000	0.8	0.64	0.38 – 15.75	1.98 – 9.90
NMe200	0.9	0.90	0.87 – 11.20	
NMe300	0.5	0.58	1.22 – 15.41	
NMe400	0.45	0.57	1.78 – 15.68	4.30 – 12.70
NMe500	0.3	0.26	0.67 – 7.49	
NMe600	0.2	0.24	2.01 – 15.01	1.94 – 11.62
NMe700	0.3	0.40	2.06 – 14.01	3.73 – 12.88
NMe800	0.7	0.88	2.97 – 14.82	5.04 – 15.21
NMe900	0.5	0.60	2.52 – 10.89	3.13 – 11.00
NMe1000	0.5	0.58	1.38 – 11.69	
NMe1100	0.5	0.71		1.36 – 7.06
NMe1300	0.25	0.25		6.18 – 10.89
NMe1400	0.15	0.25	2.66 – 8.25	6.69 – 11.39
NMe1600	0.25	0.50	2.74 – 6.70	
NMe1700	0.4	0.54	1.65 – 9.42	
NMe1900	0.25	0.43	1.67 – 11.83	
NMe2100	0.1	0.36	2.23 – 6.49	3.61 – 9.87
NMe2200	0.15	0.45	2.16 – 4.36	3.49 – 6.34
NMe2300	0.5	0.49	4.35 – 9.46	3.22 – 10.87
NMe2400	0	0.10	2.2 – 5.4	4.07 – 12.97
NMe2500	0.5	0.45		4.07 – 16.21
NMe2700	0.6	0.59		7.94 – 3.66
NMe2800	0.5	0.45		6.10 – 9.64

Table 3.1: A list of all the samples studied with the concentration based on volumes (C[Vol]), the concentrations corrected using the Raman spectrum (C[Raman]) and the pressure range for which each sample was studied with Raman spectroscopy and XRD. Note: some series are missing if they were loaded and then discarded or lost before an appreciable pressure range was studied.

3.3 Raman Spectroscopy

This section presents an overview of the theory and experimental technique of Raman spectroscopy as it applies to the high pressure study of solids. This type of vibrational spectroscopy is used in this work to complement results obtained from XRD, and to refine the phase lines in the overall nitrogen-methane binary phase diagram.

In addition to obtaining data sets containing the frequencies of the Raman modes of the sample over pressure, Raman spectra were taken immediately after loading. Based on the intensities of the Raman active modes, it is possible to determine whether the sample was of sufficient size and estimate the relative concentration of the mixture. This ensures that the loading was successful before more extensive studies are carried out. A summary of Raman scattering in the study of solids is presented in section 3.3.1, and then more specific experimental details are presented in section 3.3.2.

3.3.1 Theory of Raman Spectroscopy

Raman spectroscopy, as introduced in section 2.2.3, involves measuring the quasi-elastic scattering of light off a material. This scattering, or the Raman Effect, was first observed in 1928 by C.V. Raman who won the Nobel Prize two years later [Serway, p. A34]. A photon can interact with a molecule, exciting it to a higher rotational or vibrational state. This results in a decrease in frequency of the scattered light (or increase in wavelength), which is referred to as Stokes shift. In anti-Stokes shift, an already excited molecule lowers its energy to contribute to the photons energy, causing an increase in the scattered photons frequency. The resulting Raman spectra appears as bands, separated from the incident exciting line by frequency shifts. These frequency shifts, or Raman shifts, are measured in wavenumbers in units of cm^{-1} [Eremets, 330], [Andersen, vol.1, p.4-5].

The wavenumber is often seen in spectroscopy, as it is directly proportional to the energy of a transition between states in a molecule [Ferraro, p. 3-4]. The wavenumber can be expressed as an energy as well in units of hc since $E(hc)^{-1} = \lambda^{-1}$ = wavenumber.

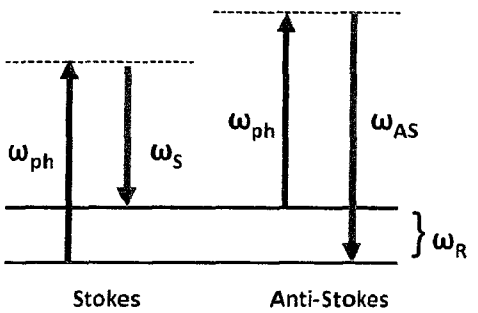

Figure 3.10: The Raman effect: Stokes and anti-stokes scattering involves the incident photon losing and gaining energy, respectively. The inelastically scattered photon has a resulting energy of $\pm\omega_R$ (the subscript R refers to the Raman scattered light).

Raman spectroscopy measures these energy shifts to extract information about the molecule and its environment, based on the number and position of bands. For a solid this is determined by the distribution of atoms in the molecule and in the crystalline environment, including the orientation, order and symmetry of the molecules in the unit cell. The Raman bands representing the intramolecular interactions often appear between 400 and 4000 cm^{-1} [Andersen, v.1, pp. 17-18, 22-23].

Since intermolecular forces in a solid are dependent on molecular and atomic spacing, the frequencies of the vibrational modes become a sensitive monitor of the pressure-induced properties and transitions [Hemley, R.J., 1988]. Thus, transitions can be marked by the appearance or disappearance of modes, or changes in the slope of the frequency over pressure. The Raman spectra can assist in determining the correct space group when used in combination with diffraction experiments [Jayaraman, 1986]. It is also a powerful tool for probing mixtures, as the vibrational spectrum is influenced by its environment [Schouten, 1995]. It is for these reasons that Raman spectroscopy is used to investigate the nitrogen-methane system.

3.3.2 Experimental Overview for Raman Spectroscopy

The technique has advanced significantly since its original design employing sunlight to excite the material, and visually observing the resulting spectrum through a telescope. The use of a laser as the excitation source has been an important development, as are spectrographs capable of gathering a large amount of light while discriminating against unwanted Rayleigh scattering [Raman Effect, vol. 2, p.759-760]. These developments have overcome the fact that Raman scattering is up to 6 orders of magnitude weaker than Rayleigh scattering.

All Raman spectroscopy measurements performed in this work were done in our laboratory at the University of Ottawa. The excitation source was either a tunable Argon ion laser with wavelength of 488 nm or 514.5 nm or a frequency-doubled Nd-YAG laser with a wavelength of 532 nm. An Andor spectrograph with a focal length of 0.3 m was employed with a grating of 1800 lines/mm and connected to a thermoelectrically cooled (-70°C) CCD for light detection.

Excitation power ranges from 10 to 15 mW at the sample. Filters may be used to protect the sample from melting if the pressure is near the melting line of the sample. An edge filter is used to filter out some of the intensity of the direct beam. The laser spot size was ~5 μm. Since this is a small fraction of a typical sample diameter, the uniformity of the sample can be monitored.

The acquisition parameters (exposure length, number of accumulations, slit width) were varied, although most spectra were taken between 2 and 20 minutes. The data extracted from the spectra were the peak positions and intensity. It was important to resolve whether the peaks were multiplets. This information was obtained using XRDA [Desgreniers, 1994] which allowed for the peak fitting using the Pseudo-Voigtian fitting function.

3.4 X-Ray Diffraction using Synchrotron Radiation at the Canadian Light Source

XRD is vital in properly describing the nitrogen-methane phase diagram. Not only does it offer the identification of phase transitions like Raman spectroscopy, but it also distinguishes the number of phases present and allows for structure determination. All XRD experiments are performed at the Canadian Light Source (CLS) in Saskatoon with the use of high-energy X-rays from the Hard X-ray Microanalysis (HXMA) 06-ID beamline. A wavelength of 0.509176 Å, or an energy of about 24.35 keV, was used for all XRD experiments, except for the NMe400 series, for which a wavelength of 0.51595 Å was used.

There are several difficulties associated with performing XRD at high pressure. As described in section 2.1.3, the DAC can generate high pressures while still allowing for measurements of various types, such as XRD, to be made. Of course, this limits the amount of sample that can be used. Also, obtaining high quality single crystals becomes difficult, as powders are often formed upon compression. The following sections provide a brief overview of XRD and powder X-ray diffraction (pXRD), synchrotron radiation and structure determination.

3.4.1 Brief Theory of X-Ray Diffraction

The discussion of XRD is restricted to diffraction from a crystalline material. X-rays interact with the electron density upon entering the crystal. The diffracted beam results from the constructive interference of the diffracted X-rays off successive planes of atoms. The condition for constructive interference is that the diffracted beams from different planes of atoms are separated by a multiple of the wavelength of incident radiation (it is treated as elastic scattering). This is displayed in Fig. 3.11 and summarized by Bragg's law,

$$n\lambda = 2dsin\theta \qquad \text{(Equation 3.1)}$$

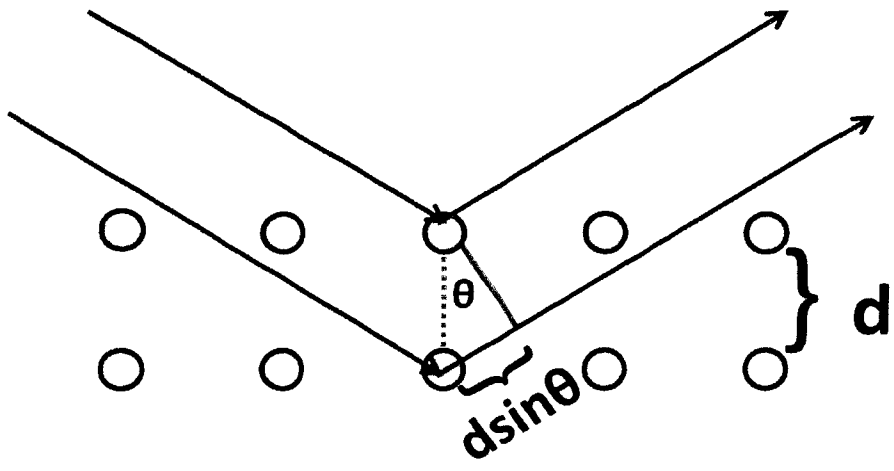

Figure 3.11: X-ray scattering off atoms in successive planes. Note: the X-ray scattering off the lower atom travels an extra dsinθ on each side of the atom, making the path difference between the two beams 2dsinθ.

When many atoms are present, distributed over the unit cell at different sites, diffracted beams of different angles or energies arise and produce a diffraction pattern. The pattern is comprised of a collection of constructively interfering diffracted beams (a Bragg reflection), each one arising from the diffraction of a particular plane of atoms with indices (*hkl*). This pattern can be analysed to extract structural information including the lattice parameters of the unit cell, symmetry group and the positions of the atoms within the unit cell.

As it is the electrons that scatter X-rays, the scattering power of an atom is related to how many electrons it contains. A unit cell is made up of one or more atoms, and a crystal is made up of many atoms. The structure factor, describing the way that the atoms of a unit cell scatter the X-rays, depends on the atomic species and their position. For a specific (*hkl*) plane, the structure factor is

$$F_{hkl} = \sum_{n}^{N} f_n e^{2\pi i(hx_n + ky_n + lz_n)} \qquad \text{(Equation 3.2)}$$

where the nth atom has an atomic scattering power (form factor) f_n and is located at (x_n, y_n, z_n) in the unit cell that contains N atoms. The structure factor, F_{hkl}, must be multiplied by its complex

conjugate, giving $|F_{hkl}|^2$, to obtain a value that is proportional to the scattering intensity. Through this relationship, the observed intensities of the XRD, along with information of the unit cell and atomic species, the atomic positions can be found [Cullity, pp. 128 – 137].

XRD can be divided into two main types: angular or energy dispersive. In the first, which is the focus of the subsequent sections, the wavelength is fixed and the diffraction pattern is obtained over an angular range dependent on the wavelength used and the distance between the detector and sample. In the latter, the wavelength is varied and the XRD pattern is recorded at a constant angle.

3.4.2 Powder X-Ray Diffraction

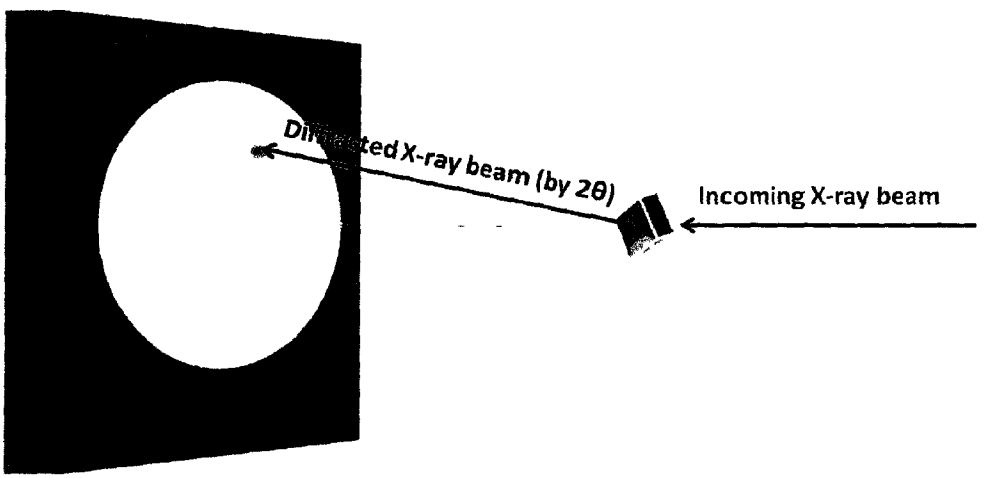

Figure 3.12: The incoming X-ray beam is diffracted off the plane(s) that are in its path. For a single crystal, the diffraction image appears as spots.

When a single crystal plane is exposed to the X-ray beam, the result is a diffracted beam that corresponds to the particular d-spacing of that plane (Fig. 3.11). If that plane is exposed to the X-ray beam at different orientations, i.e., by rotating the crystal keeping the plane of interest

perpendicular to the X-ray beam, the diffraction spots appear along a ring (the Debye ring) at a constant 2θ position on the detector (Fig. 3.12).

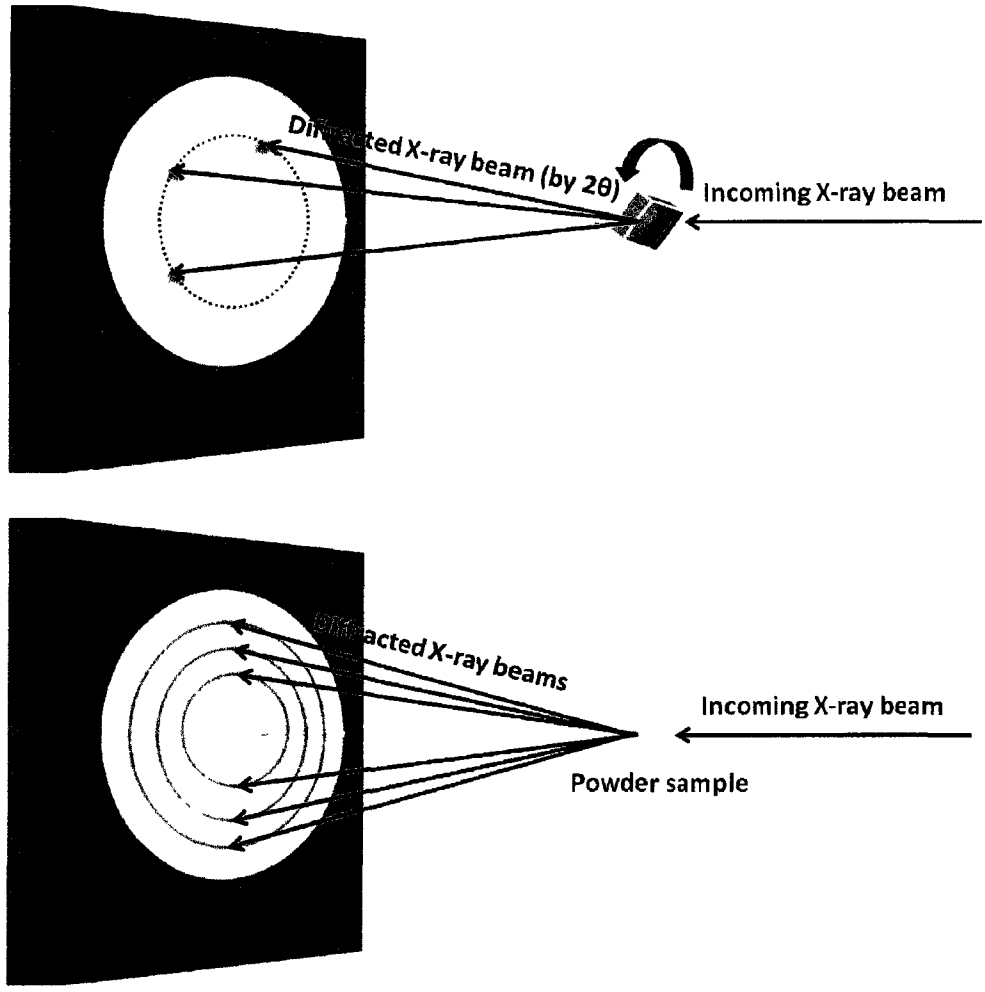

Figure 3.13: (Top) If the single crystal is rotated about the incoming beam, then spots are observed from the different orientations of the same crystal plane(s) along the Debye ring. (Bottom) Powder samples represent many crystals (and thus all crystal planes) with many orientations. The XRD pattern appears then as complete, continuous rings.

When many crystals are present, including all orientations and with all crystal planes exposed to the X-ray beam, a pattern of rings form (Fig. 3.13). These rings are at 2θ as determined by Bragg's law, and correspond to the possible (*hkl*) indices of the planes in the crystal. Unlike single

crystal diffraction, the use of a powder sample eliminates the need to rotate the crystal and the acquisition of many images to account for all orientations and crystal planes.

Before the late 1930's, XRD was dominated by single crystal methods. At that time, pXRD was only beginning to be employed for phase identification. PXRD became a commonly used technique in the 1970's. The development of pXRD caused it to become successful in full structure determination, which was once only possible through single crystal diffraction. Although powder diffraction is more commonly used as a means of structure refinement, it is also important for samples that do not form single crystals, such as those studied under pressure. High pressure pXRD commenced in the 1980's and evolved to allow XRD to be performed on a sample within the DAC [Langford, 1996]. However, pXRD on a sample within a DAC still presents many difficulties. Since the powder quality cannot be easily controlled within the DAC, producing an ideal powder, consisting of many randomly oriented crystallites, is a challenge [Hammond, 2009].

3.4.3 High Pressure XRD: Advantages of Synchrotron Radiation

Although the DAC has many favourable features, it also has several qualities that hinder the use of XRD. The diamond anvils absorb the vast majority of X-rays when a conventional copper tube is used. The seats used to support the diamond anvils also limit the angular opening available for diffraction. In order to reach sufficiently high pressures, only a small amount of sample can be used, greatly reducing the amount of crystals which form the diffraction pattern. Thus, with conventional X-ray sources with Cu and Mo radiation targets and X-ray point detectors, the scattered intensity and range is severely restricted.

Synchrotron light sources became available in 1961 and today there are over 40 globally [CLS, www.lightsource.ca]. This opened many new possibilities and improved already established techniques due to its many advantages [Langford, 1996]. Synchrotron radiation results from the use of magnetic fields to curve the path of particles moving at close to the speed of light. The relativistic particles emit an intense, continuous spectrum of light ranging from microwaves to hard X-rays

[Cullity, pg. 25]. This range brings about the tunability of synchrotron sources, with possible wavelengths ranging from near IR to high energy X-rays [Hammond, 2009, pp. 239-240].

At the Canadian Light Source, electrons are injected into a linear accelerator in which electrons are accelerated to 99.9998% the speed of light. The electrons are accelerated further in the booster ring, from an energy of 250 MeV when they leave the linear accelerator to 2900 MeV. The electrons are then injected into the storage ring. In the storage ring, powerful magnets bend the path of the electrons, resulting in the generation of synchrotron light. Insertion devices (wigglers and undulators) further accelerate the electrons producing intense synchrotron light [CLS website, www.lightsource.ca].

Synchrotron radiation sources offer X-rays at high energies that are far more intense than X-rays provided by conventional sources. Today, third generation synchrotron radiation sources are available that provide at least 7 – 8 orders of magnitude more hard X-ray flux than a conventional source [CLS website, www.lightsource.ca]. Other advantages include the high degree of polarization and a very low beam divergence [Massa, 2004, p. 16].

The high energy X-rays produced with synchrotron radiation helps to alleviate the limitations imposed by the DAC. The high flux and low divergence ensure that a sufficient number of photons reach the sample. Referring to Equation 3.1, Bragg's law, it is clear that the atomic spacing, d, and maximum angle, θ, allowed by the DAC are fixed. By decreasing the wavelength of radiation used, more reflections are available that satisfy this condition. For these studies, wavelengths on the order of 0.5 Å are typically used. Section 3.4.4 provides a discussion on the specific set-up at the Canadian Light Source (CLS) used in this work.

3.4.4 The Hard X-Ray Microanalysis (HXMA) Beamline at CLS

All XRD experiments performed for this work were conducted at the HXMA beamline at the CLS. This beamline includes a 63 pole superconducting wiggler and the Si(111) or the Si(220) plane

of a double crystal monochromator that is used to select wavelengths from 0.3 to 2.5 Å for various experiments.

The synchrotron radiation passes through an optics hutch prior to the experimental hutch. In this, the components focus and control the beam and the desired wavelength is selected. The beam is further focused within the experimental hutch, and components are present to monitor the beam intensity and energy. Radiation shields and helium filled flight tubes reduce scattering off air and upstream components prior to reaching the sample and detector.

The experimental set-up for high pressure XRD at HXMA is shown in Fig. 3.14. The X-ray beam enters the set up and passes through a collimator assembly (45 to 60 μm in diameter) and then through the sample. After the beam of x-rays diffracts off the sample, it reaches an area detector. A beamstop (not shown in the Fig. 3.14) is situated in the path of the direct beam to protect the detector. The beamstop also includes a Si PIN diode to monitor the scattered intensity of the direct beam through the sample at all times.

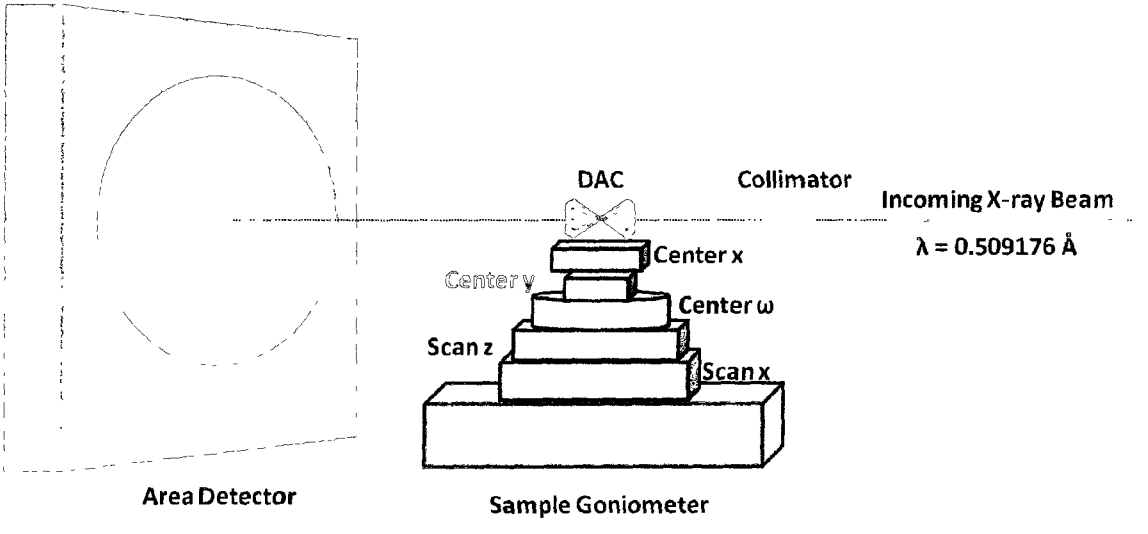

Figure 3.14: The basic idea of the experimental configuration at HXMA.

The sample is mounted on a set of motorized stages that can be controlled from outside the hutch. A reproducible sample centering method is required for working with samples within a DAC, as it is not feasible to visually observe the sample. A method, described in [Smith, et al., 2008], has been devised that compares the x-ray transmission profile of a sample over a range of positions. The intensity of X-rays transmitted through the sample is compared as x, y, z and ω are scanned. Observing optimal values generally implies that the sample is well centered.

The sample is generally placed approximately 400 mm away from the Marresearch mar345 area detector. This, along with the wavelength, determines the maximum scattering angle recorded by the detector. Based on these quantities the maximum 2θ (measured radially outward from the direct beam position) is about 30°, which is reasonable considering that the angular limitations imposed by the DAC are similar. The mar345 detector records diffraction images 345 mm in diameter with a pixel resolution of 100 μm x 100 μm.

Although area detectors are common for the XRD of samples under high pressures, other detectors include photographic film, CCDs, and other photon counting detectors [Langford, 1996], [Massa, 2004, pp. 81-83]. Area detectors are employed because they allow for numerous reflections to be recorded in each exposure. From the position of the reflection or ring of reflections, the (*hkl*) of the reflection can be calculated. [Ladd, 2003, p.269] Additionally, an area detector is well suited for pXRD since it allows for the collection of data over the entire Debye ring, which is important when the powder is not ideal. This also gives an immediate indication of the quality of the sample [Smith, 2008].

3.4.5 Structure Determination with XRD

A major contribution to the development of pXRD techniques was the introduction of the Rietveld method for structural refinement in 1967 [Langford, 1996]. This method, commonly used to refine powder patterns, compares experimental and calculated trial diffraction profiles using a least squares approach. The trial diffraction pattern is refined to minimize a residual function r:

$$r = \sum_j w_j (y_j - y_{c,j})^2 \qquad (4)$$

where y_j and $y_{c,j}$ are the intensities of the experimental powder pattern and calculated powder pattern, respectively, of the jth point which has a weighting factor of w_j. The goodness of fit can be determined by an R-factor, of which there are different kinds. The weighted profile R-factor, R_{wp}, is defined as

$$R_{wp} = \frac{\sum_j w_j (y_j - y_{c,j})^2}{\sum_j w_j (y_j)^2} \qquad (5)$$

[Ladd, 2003 pp. 589-590].

This method is used only after a structure has been proposed. The complete structure determination process includes indexing a unit cell, assigning a space group, determining atomic positions and then refining the structure (using methods such as Rietveld). To carry out this process, the best possible quality of data is required. The methods used to acquire pXRD data were summarized in the preceding sections.

An XRD image acquired at HXMA using the mar345 detector can be integrated using Fit2D software to produce the one-dimensional XRD pattern [Hammersly, 1996]. This pattern is then analysed using XRDA [Desgreniers, 1994] with the assistance of indexing programs, such as the Crysfire suite of indexing programs [Shirley, 2000]. Possible space groups can be assigned and verified using Chekcell or reflection conditions. This is demonstrated here for the case of LaB_6.

It is important to ensure proper alignment, optimization and calibration of the XRD experimental set-up. To do this, an XRD image of a standard is taken. By analysing the resulting diffraction image, the accepted lattice parameters should be obtained within 0.001 Å. For this work, LaB_6 (at ambient pressure) is used. A five minute X-ray exposure is acquired and the diffraction image should appear as well defined Debye rings, shown in Fig. 3.15.

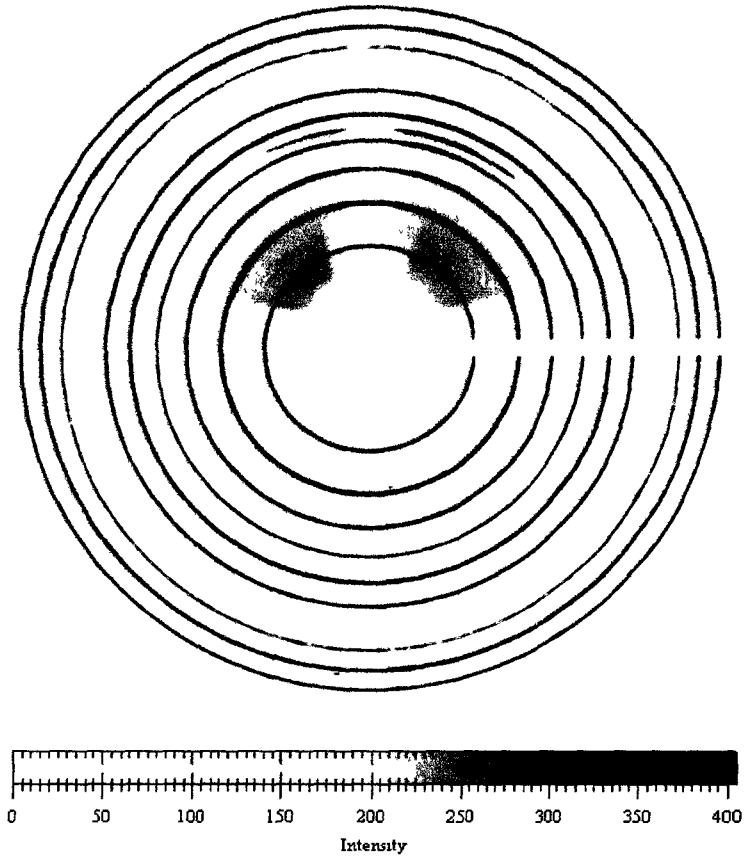

Figure 3.15: Diffraction image of LaB_6 and the corresponding intensity scale (the intensity is arbitrary and measured by the number of counts). The background is uneven because the sample mount shields the lower portion from incoherent X-ray scattering that is not from the sample.

The Debye rings are integrated over the azimuthal angle using Fit2D (Fig. 3.16). This is especially helpful if a powder sample contains larger grains. Instead of well defined rings, large grains produce a "spotty" pattern, since not all crystal planes are represented evenly. Integrating the intensity over the Debye ring is beneficial in this case. In order to further improve the image quality, the sample can be rocked over a small angular range (usually less than 8° on either side). This increases the uniformity of a spotty Debye ring since it introduces planes of crystals to the X-ray beam that may not otherwise be accounted for in the diffraction image. Fit2D also refines the sample-to-detector distance and beam center, parameters that are necessary to convert a spatial position from Cartesian to polar coordinates.

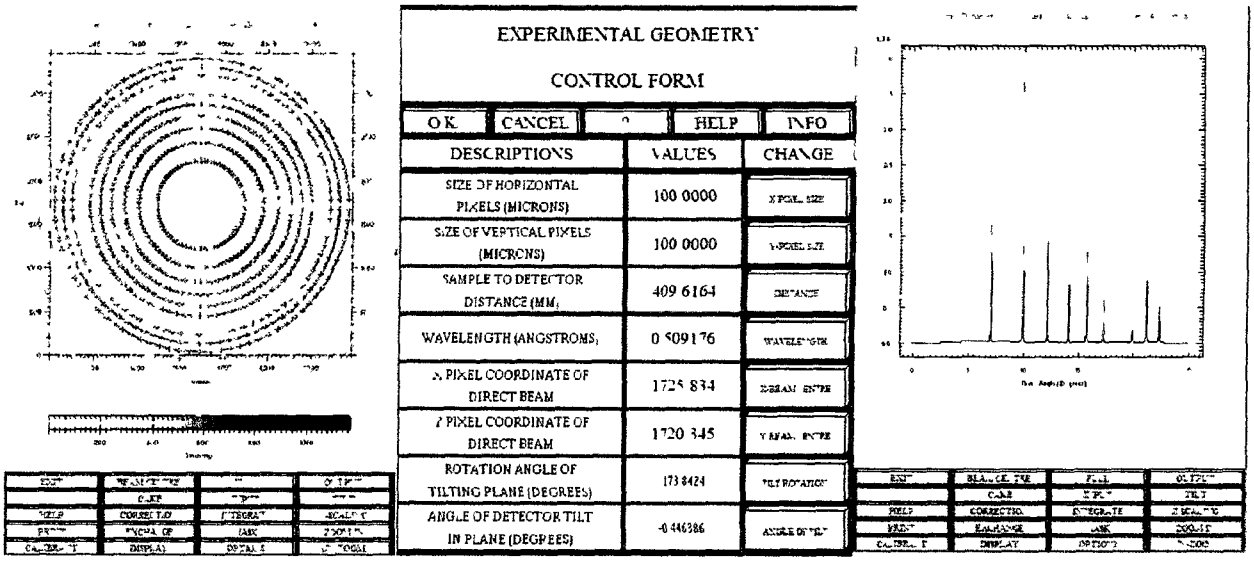

Figure 3.16: The XRD image of LaB_6 (left panel) is used for a calibration image. Using Fit2D software (shown) the image is analyzed to determine the geometrical parameters in the center panel (beam center, sample-to-detector distance, tilt and rotation of the detector). Once calibrated, the image can be integrated to form the XRD pattern (right panel).

The positions (2θ) of the reflections can be input into the Crysfire suite of indexing programs. This suite includes several algorithms for proposing unit cell parameters based on the given reflections and provides these solutions ranked with a figure of merit. This program is described elsewhere [Shirley, 2000]. Using the proposed solutions, XRDA [Desgreniers, 1994] can illustrate the fit by displaying the calculated reflections of the specified unit cell and estimate the difference between the calculated and experimental patterns, Fig 3.17.

If there is an excess number of calculated reflections that do not match up with any of those observed experimentally, a better fit of the data can be found when a proper space group is selected. Different space groups have different conditions for systematic absences. Accidental absences can also occur due to the distribution of atoms through the unit cell.

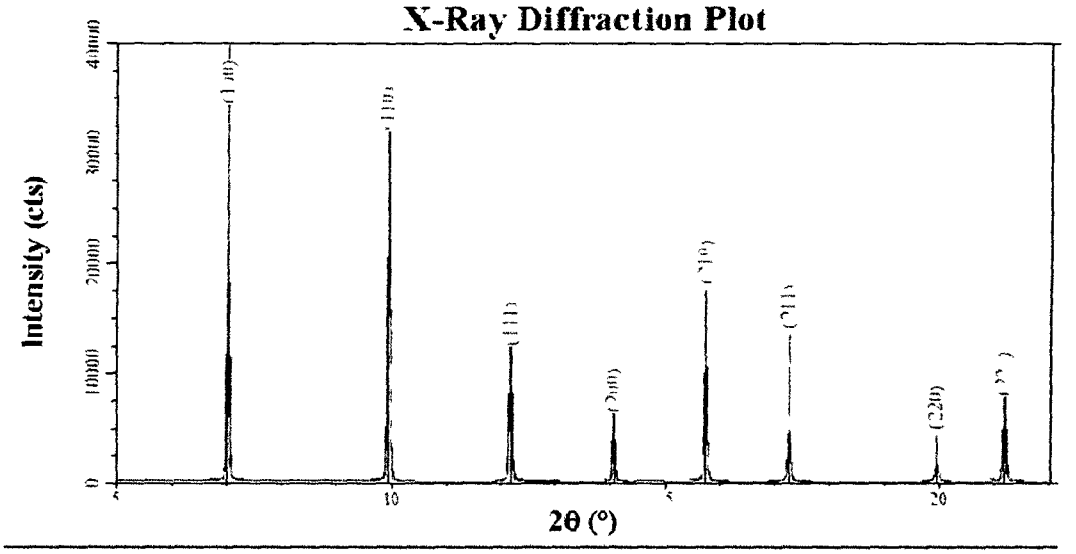

Peak Fitting

lambdaO = 0.5092±0.0005 A C:\Users\owner\Documents\MSc\CLS June 2010\LaB\LAB14062.XRD C:/Users/owner/D

	#	hkl	d (Å)	2*theta (°)	Area	fwhm	diff	type	comment	offset	slope	quad
		cubic										
	0	100	4.1581	7.020±0.000	919±3	0.045±0.000	0.00085	gl		473	22.48	
	1	110	2.9396	9.937±0.000	1841±5	0.051±0.000	-0.00019	gl		916	12.72	
	2	111	2.4005	12.176±0.000	690±3	0.051±0.000	0.00012	gl		2218	158.31	
	3	200	2.0789	14.069±0.000	719±7	0.049±0.000	0.00009	gl		1687	102.86	
1	4	210	1.8592	15.711±0.000	771±3	0.055±0.000	-0.00012	gl		2473	171.39	
	5	211	1.6972	17.255±0.000	814±2	0.061±0.000	-0.00014	gl		814	35.64	
	6	220	1.4699	19.949±0.000	103±1	0.069±0.001	-0.00010	gl		544	18.01	
	7	300	1.3858	21.172±0.000	444±2	0.056±0.000	-0.00002	gl		2165	-9.07	
	8	310	1.3147	22.238±0.000	244±2	0.066±0.000	-0.00001	gl		3057	-157.49	

Figure 3.17: The integrated image is then indexed. The program XRDA allows one to plot the pattern and overlay the calculated pattern of the input unit cell. Unfortunately, the intensities it calculates are not necessarily accurate.

In order to determine the coordinates of the atoms in the unit cell, the diffraction data must include accurate intensity values. This is not possible with the methods used for this work, so it is not described further. However, without atomic positions, a Le Bail fit can be done. A Le Bail fit basically calculates the best possible set of intensities for a given observed diffraction pattern and proposed space group and lattice parameters. Although it does not directly confirm a proposed unit cell and space group, a small deviation between calculated and observed intensities can provide confidence that it is plausible. If a proposed structure is available, powder diffraction data can be used to refine the positions using Rietveld methods, which is incorporated into the codes of Fullprof [Rodriguez-Carvajal, 2006] and Rietan [Izumi, 1985].

4. Results

4.0 Introduction

The main objective of this work was to construct a phase diagram to represent the solid phases of the nitrogen-methane binary system under high pressure at room temperature. This was completed through the study of 23 samples of varying concentration using pXRD, Raman spectroscopy, and visual observation. These techniques were described in chapter 3.

This chapter outlines the results that contributed to the construction of the nitrogen-methane binary phase diagram. The proposed phase diagram is summarized in section 4.1. In the subsequent sections, the evidence for each phase is presented. In sections 4.2 and 4.3, the pure phases of nitrogen and methane are described. Finally, the novel vdW compounds discovered in this system are described in section 4.4 and 4.5.

4.1 The N_2-CH_4 Binary Phase Diagram

The phase diagram in Fig. 4.1a displays different regions in which a phase or phase mixture is observed by pXRD. The phase lines show the concentration and pressure estimated for a transition to occur from one phase region to another. These phase lines were extrapolated based on pXRD results and were refined using Raman spectroscopic measurements. A discussion on the validity of these phase lines is given in Chapter 5, section 5.3. Mixtures were studied between 10% and 90% nitrogen. In some phase regions, phases were observed that resemble a pure phase of either nitrogen or methane. By adding one molecular component into the structure of the other, the lattice parameters change. This is noted by changing the name of the phase from the previous label (A) to the label with an asterisk (e.g. A*).

Above the melting line and fluid-solid (I*-CH_4 + fluid) region, a solid-solid region exists (these regions are described in section 4.2). The phases in this solid-solid region are referred to as the first solid phases. In the first solid phase regions, the system adopts a phase similar to that of the pure species in that pressure range. This region also contains the only phase line that indicates a co-existence. The line separating the I* phase and the β* phase represents a concentration at which both phases are observed. Above the first solid region, phases resembling the pure phases of nitrogen and methane are observed in phase mixtures (described in section 4.3).

In the pressure-concentration range studied, two phases are observed in which the XRD patterns are unique from those of the pure species. These phases represent novel molecular vdW compounds named T_1 and MR described in section 4.4 and 4.5, respectively. For these compounds, a unit cell is proposed and an equation of state is presented along with possible space groups and number of molecules.

The methane-rich portion of the phase diagram represents a particularly complicated collection of phase mixtures. Below concentrations of 50%, the B*, T1, and MR phases exist in all combinations of two phase mixtures. This side of the phase diagram, as is with pure methane, seems to be strongly affected by hysteresis and the thermodynamic path taken. This is discussed in more detail in section 5.1.

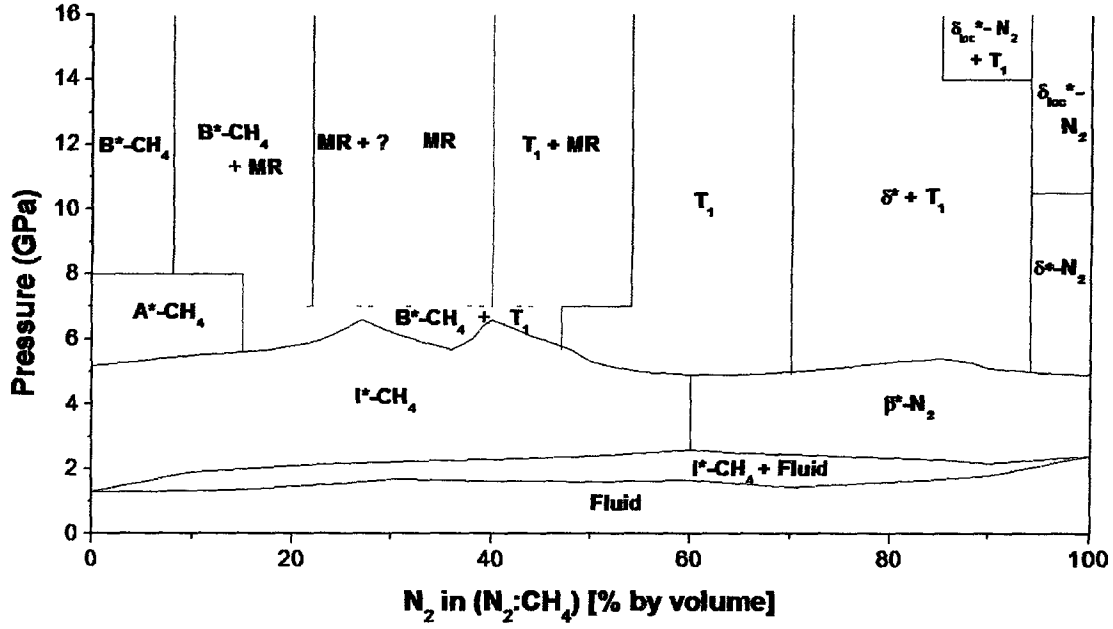

Figure 4.1a: The proposed nitrogen-methane binary phase diagram. The dotted line between MR + ? and the MR phase represents an uncertain phase line, and the dashed horizontal phase line represents a region whose vertical phase line is strongly affected by hysteresis.

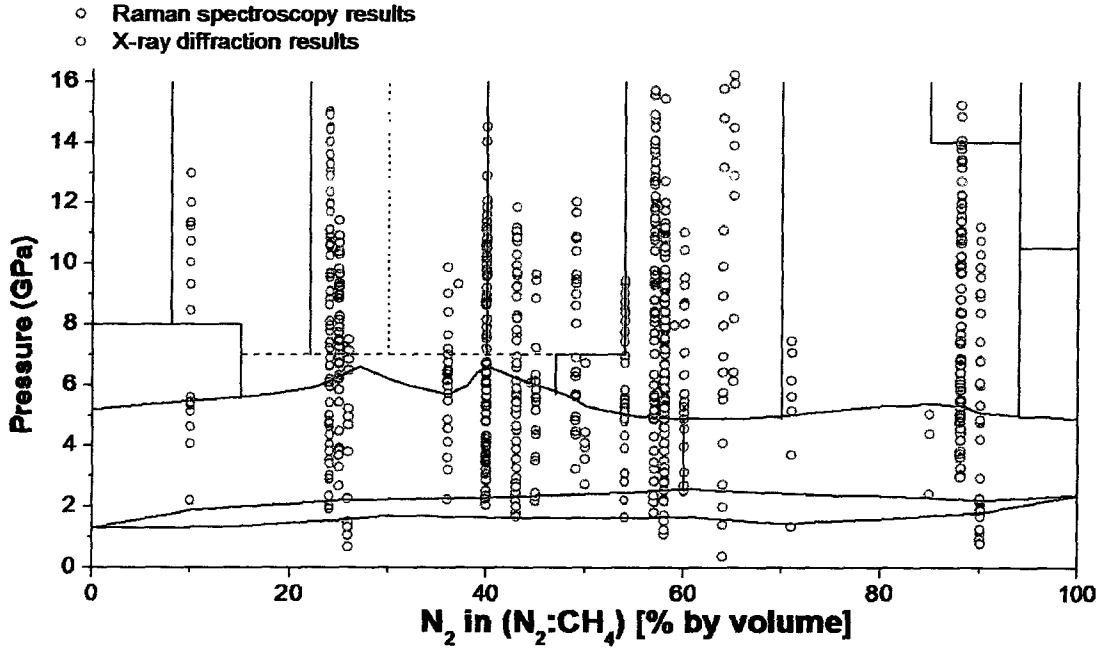

Figure 4.1b: The proposed phase diagram displaying the pXRD and Raman spectroscopy measurements taken.

Fig. 4.1b displays the data points taken using pXRD and Raman spectroscopy. These include data sets of both compression and decompression. In order to determine a transition pressure, several things are taken into account: the Raman spectra and/or diffraction pattern, how long the sample had to settle into equilibrium, whether it was upon compression or decompression, and the visual appearance of the sample. This data is also compared to data taken at higher and lower pressures in order to confirm whether a phase transition has indeed occurred.

The transition pressure is narrowed down to a small range (generally less than 0.5 GPa), usually through Raman spectroscopy measurements, since we have limited time at the HXMA beamline at CLS for XRD. Raman spectroscopy studies complemented by visual measurements (the phase transitions are observable – these measurements are not displayed in Fig. 4.1b) are used to refine the shape of the melting lines and the transition from the I*-CH_4/β*-N_2 phases to the higher pressure phases.

The vertical (concentration) phase lines are much more difficult to refine. Since we are not able to vary the concentration within the sample, the vertical phase lines must be estimated based on the concentrations studied. Throughout a region in which a phase mixture is observed, changes in concentration are often accompanied by changes in the relative intensities of the diffraction patterns from one phase to the other. Using this, the transition concentration can be estimated.

The vertical phase lines separating the B*-CH_4 and B*-CH_4 + MR and δ*/δ_{loc}*-N_2 and δ*/ δ_{loc}*-N_2 + T_1 phase regions are estimated based on the predicted saturation point of the pure phases. As no concentrations above 90% or below 10% have been studied, an estimate must be made based on the relative intensity of the diffraction pattern of the pure phase to the compound. For example, the diffraction peaks from the B*-CH_4 phase are significantly more intense than those of the MR phase at 10%. Thus, the concentration for which B*-CH_4 can no longer hold any nitrogen molecules should be very close to 10%.

The following sections describe each observed phase, presenting evidence and discussion on the implications of the interactions between nitrogen and methane molecules under pressure. For the first solid region, the fluid-solid region and the melting line, comparisons are made between the room temperature and low temperature phase diagrams.

4.2 The Phase Diagram below 5 GPa

The phase diagram below 5 GPa represents the first solid regions, the solid-liquid region and the liquid-liquid region. This area represents the only portion that has received previous attention in literature [Connolley, 1980], [Prohvatilov, 1983], [Omar, 1962]. These works were introduced in section 2.3. The melting line and solid-fluid region exhibit some differences between the room temperature and low temperature phase diagrams. The first solid region shows increased solubility for each component. In addition to the mixed system in this pressure range, pure β-nitrogen was also studied, as few room temperature lattice parameters are published [Schiferl, 1983], [Cromer, 1980].

4.2.1 The Melting Line and Solid-Fluid Region

No XRD results were used to produce the melting line or the fluid-solid phase line. This was done using visual observation and Raman spectroscopic measurements. Changes in the Raman modes of nitrogen or methane, including broadening and wavenumber shift, indicate the transition between the solid and liquid state and are used to establish points on the melting curve.

Although the melting line is not entirely smooth, the melting line of both nitrogen and methane appear overall as an increasing line from the melting point of pure methane to that of pure nitrogen. The melting line in the low temperature range and at very low pressures appears somewhat different. The melting line is constant over the nitrogen-rich side of the phase diagram then increases steadily towards the melting point of methane. The concentration for which the melting line is no longer constant is represented in different studies from approximately 60% [Omar, 1962] to 80% [Prokhvatilov, 1983]. Although the data around the nitrogen-rich side at these pressures is limited, it is clear that the melting pressure does not remain constant. Rather, the melting point increases from the melting pressure of methane to that of nitrogen, with the solid-fluid region in between over the entire range of concentrations.

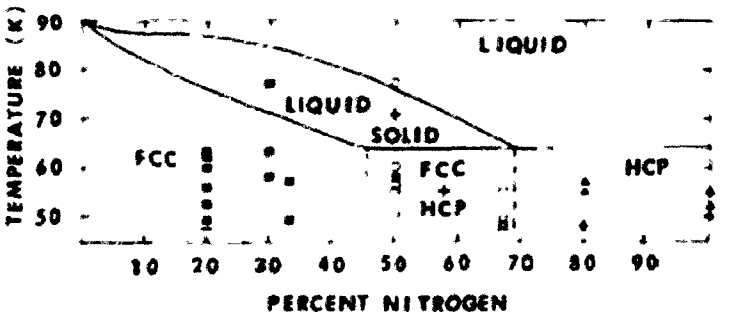

Figure 4.2: A portion of the nitrogen-methane binary phase diagram at low temperature displays the melting line, liquid-solid region and a portion of the solid-solid region [Connolley, 1980].

Figure 4.3: A 54% mixture in the solid-fluid region, around 1.78 GPa.

In the pure species at room temperature, methane solidifies at 1.3 GPa [Maynard-Casely, 2009] and nitrogen at 2.4 GPa [Hellwig, 2001]. Since the melting pressures differ by over 1 GPa, the separation of solid methane and fluid nitrogen can be expected and is easily inferred visually. Fig. 4.3 shows the fluid-solid separation. As the mixture enters the first solid region, this separation no longer occurs and it appears uniform and textureless. When both species are in the liquid state, the appearance is also smooth and no liquid-liquid separation is observed. The two components seem to be highly miscible in the liquid state.

The solid-fluid region in the low temperature phase diagram [Connolley, 1980], [Prohvatilov, 1983], does not span the entire concentration axis, and the system adopts the hexagonal close-

packed structure (the β-N_2 phase) around 62 K without any fluid methane. This deviates from the observed fluid-solid region from this work, in which the fluid-solid separation occurs for all studied concentrations. The fluid-solid separation is more stable than the dissolution of fluid methane in the β-structure below its freezing pressure.

4.2.2 Pure β Nitrogen

Despite the many reports written on β-N_2, very few room temperature studies provide lattice parameters of this phase [Cromer, 1980], [Schiferl, 1983]. Thus, a sample of pure nitrogen was loaded and studied with pXRD in order to obtain the room temperature equation of state. The sample was prepared using a similar procedure for the loading of nitrogen-methane mixtures, in which the DAC, prepared with a compression chamber with ruby microspheres, is immersed into a bath of the liquid and then pressure is applied. This sample was loaded into a membrane DAC using a stainless steel gasket. Upon loading, a few single crystals were grown. Unfortunately, a good powder was not obtained due to time constraints. However, the sample was of sufficient quality to obtain XRD images as a function of pressure, from which the lattice parameters were extracted.

XRD images of β nitrogen were recorded from 3.44 GPa to 4.71 GPa. An image taken at 4.93 GPa confirms the transition into the δ phase around this pressure. The molecular volume is plotted over pressure with the two published volumes [Cromer, 1980], [Schiferl, 1983]. The measured molecular volumes follow the equation of state of the reported values and allow more direct comparison between pure nitrogen and the mixed system.

In Fig. 4.4, the data points do not follow the expected curvature. This is in part due to the quality of the powder: the large crystals in the sample caused intense diffraction spots, saturating the detector. When integrated, this resulted in broad, intense peaks. As this high symmetry phase has an XRD pattern with few reflections, any error in the observed position of a reflection has a strong impact on the lattice parameters.

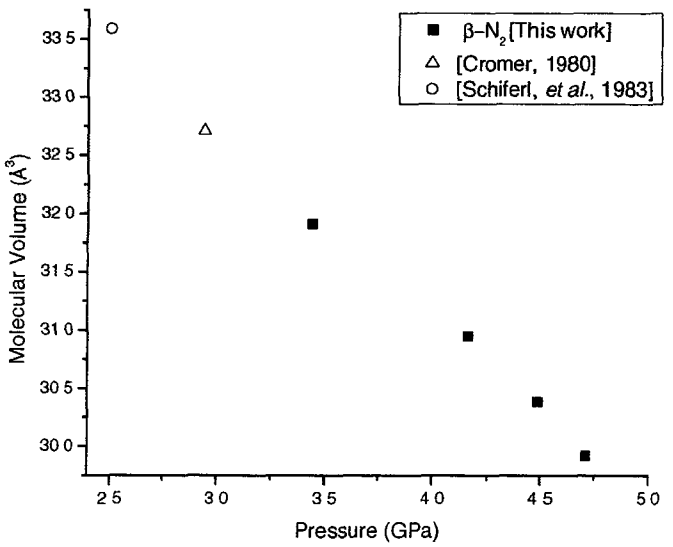

Figure 4.4: The equation of state of β-N_2 from this work and published results [Cromer, 1980], [Schiferl, 1983].

4.2.3 The β* phase

The β* phase of nitrogen exists in nitrogen-methane mixtures above 60% in the first solid region. Very few diffraction images were taken of this phase. Hence, the comparison of volume between the pure and mixed phase is qualitative only.

The Le Bail fit of an 88% mixture in the β* phase is shown in Fig. 4.5. Preferred orientation and large grains are a problem in this phase, and thus Rietveld refinement is unsuccessful. However, the XRD pattern can be calculated based on the observed cell parameters with excellent agreement to the observed pattern. The molecular volume of the β* phase in this mixture is sensitive to methane substitution. The substitution by 12% methane in the nitrogen lattice causes an increase in volume as a function of pressure, shifting it up towards the molecular volume of pure methane. Although few data points were taken, the increase in volume places the β* phase approximately halfway between β-N_2 and I-CH_4 volumes in terms of density. The increase of lattice parameters is also observed at low temperatures at similar concentrations [Connolley, 1980].

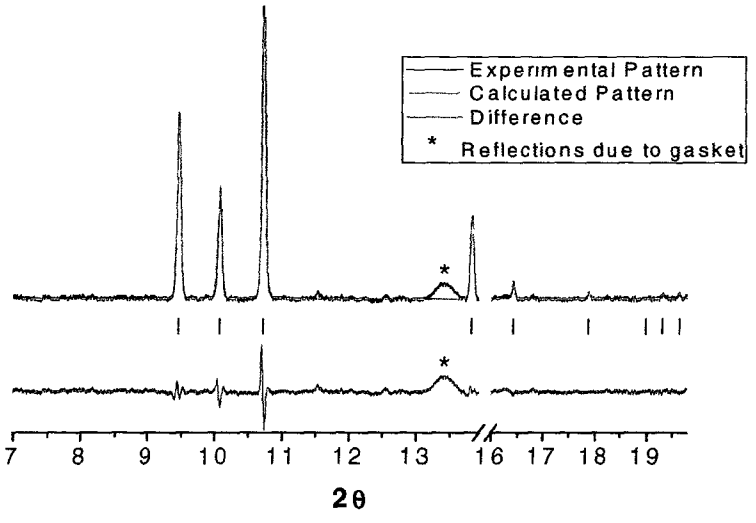

Figure 4.5: Le Bail fit of the β* phase in the 88% mixture. The tick marks note the positions of the predicted reflections based on the unit cells and space groups. The vertical axis is omitted since it represents a linear, normalized and arbitrary intensity scale. This is similar for all subsequent diffraction patterns.

The β-δ transition in pure nitrogen occurs at 4.9 GPa, whereas it seems to be shifted for the 88% mixture. Most of the samples studied showed this transition as occurring slightly above 5 GPa. The addition of methane molecules slightly increases the stability range of this structure, shifting the transition pressure closer to that of pure methane (5.2 GPa).

4.2.4 The I* phase

The I* phase exists in all mixtures below 60% in the first solid region of the phase diagram. Although the transition out of this phase occurs at 5.2 GPa for pure methane, this phase line is extended to higher pressures in the mixtures with concentrations under 50% . For a sample of 40%, this phase persists just above 6 GPa during both compression and decompression. The transition pressure does not appear smooth, and consistently occurs above 6 GPa for concentrations of 25%

and 40%. Up to 25% the transition pressure increases steadily, after 40% it declines closer to 5 GPa, and is reduced in between these concentrations. These fluctuations could be a result of hysteresis; after a pressure change, the system may require time to settle into its equilibrium state. If the pressure is changed again before sufficient time has elapsed, the transition pressure or the volume of the phase may not be representative of its equilibrium value.

Up to concentrations of 40%, the volume of the I* phase is similar to pure methane, as indicated by comparing values to those of Hazen *et al* [Hazen, 1980], shown in Fig. 4.6. As the concentration increases above 40%, however, the lattice parameter experiences a shift to lower values. This can be attributed to there being sufficient nitrogen substituted into the I-CH_4 lattice to cause a volume reduction, as nitrogen has a smaller molecular diameter than methane. The data plotted for the 49% mixture sits nearly halfway between the molecular volumes of pure methane and pure nitrogen. This structure is much less sensitive to nitrogen substitution than β-N_2, in which less than 12% methane induces a similar shift in molecular volume.

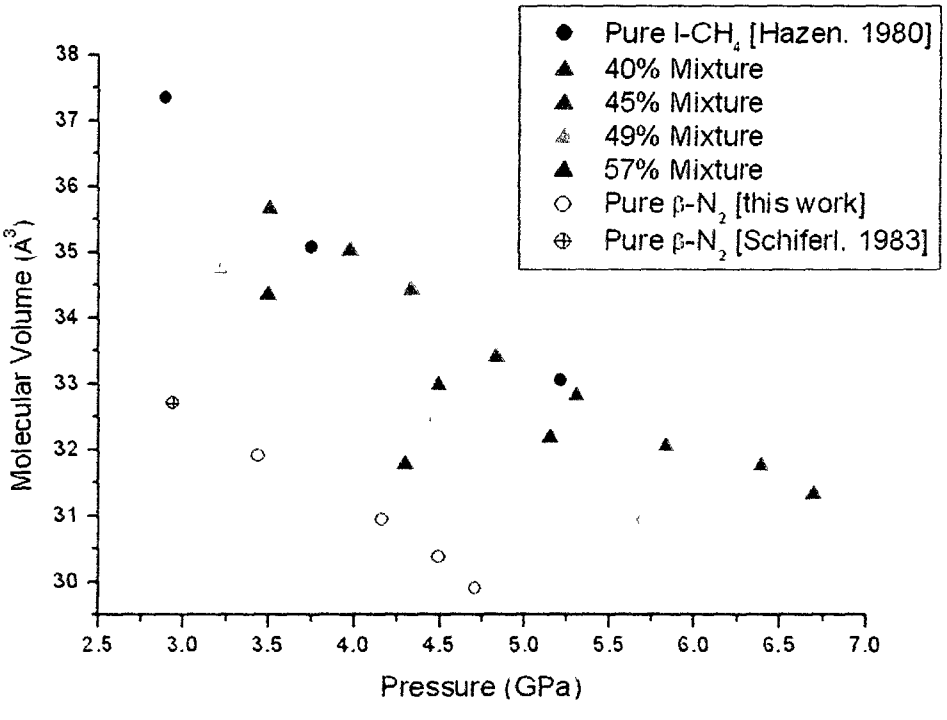

Figure 4.6: Molecular volume of the I* phase compared to that of pure I-CH_4 and β-N_2. The uncertainty on volume is approximately 0. 5 Å^3 and for pressure it is about 0.1 GPa.

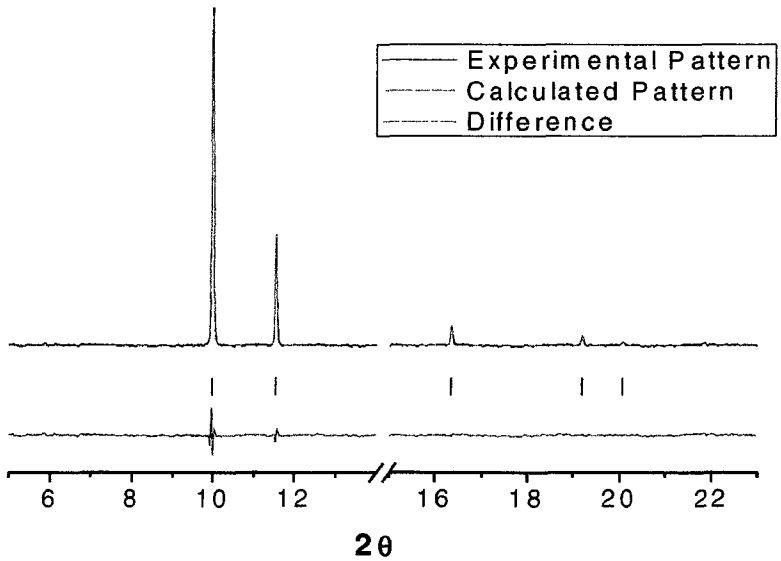

Figure 4.7: Le Bail fit of the XRD pattern of a 10% mixture in the I* phase

Fig. 4.7 shows a Le Bail fit of the XRD pattern of the I* phase. The reflections calculated based on the unit cell parameters and space group account for all observed reflections. This proves that it is the sole phase existing at these conditions. A Rietveld refinement is not completed, due to the unknown preferred orientation and unknown nature of the nitrogen substitution. In a previous study by Hazen *et al.* it was noted that each increase in pressure caused the creation of a new crystal with a different orientation [Hazen, 1980]. This is also observed in the mixtures.

This phase is observed over a wider concentration range than the first solid phase of nitrogen, indicating that it is more stable with nitrogen substitution than the nitrogen structure is with methane substitution. This was also observed at lower temperatures, where the face-centered cubic structure (fcc) typical of methane spans a wider region of the phase diagram than the hexagonal close packed (hcp) phase typical of nitrogen.

In addition to the I* phase being more stable than the β* phase, it does not have a high sensitivity to nitrogen substitution. Since 40% nitrogen can be substituted into this structure without significant changes, the nitrogen molecule must appear physically similar to the methane

molecule. The methane molecule exhibits rotational disorder in this structure. It can therefore be expected that the nitrogen molecule also possesses a high degree of spherical disorder. Although there is a slight size difference, the disorder would remove the difference in apparent geometry. This hypothesis is supported by the fact that nitrogen molecules in the pure β phase exhibit spherical disorder.

4.2.5 The Co-existence of the I* and β* Phases

In only one mixture were the I* and the β* phases observed to co-exist. This appears in the phase diagram as the coexistence line between the two phases. It is possible that there is a concentration range for which both phases exist, or that the presence of both phases results from the system being in a state outside of equilibrium. It was confirmed in mixtures of 57% and 64% that the system adopts either the I* or β* phase, respectively. In the low temperature phase diagram, this co-existence exists between roughly 50% and 70% [Connolley, 1980], although few concentrations were studied. As the solubilities of each component in the first solid phase of the other is greater at higher temperatures, it is expected that the co-existence range is reduced. The occurrence of both phases indicates that the concentration represents a solubility limit for one or both of the structures. At room temperature this limit is reduced from a 20% range to a narrow range of at most, 3%.

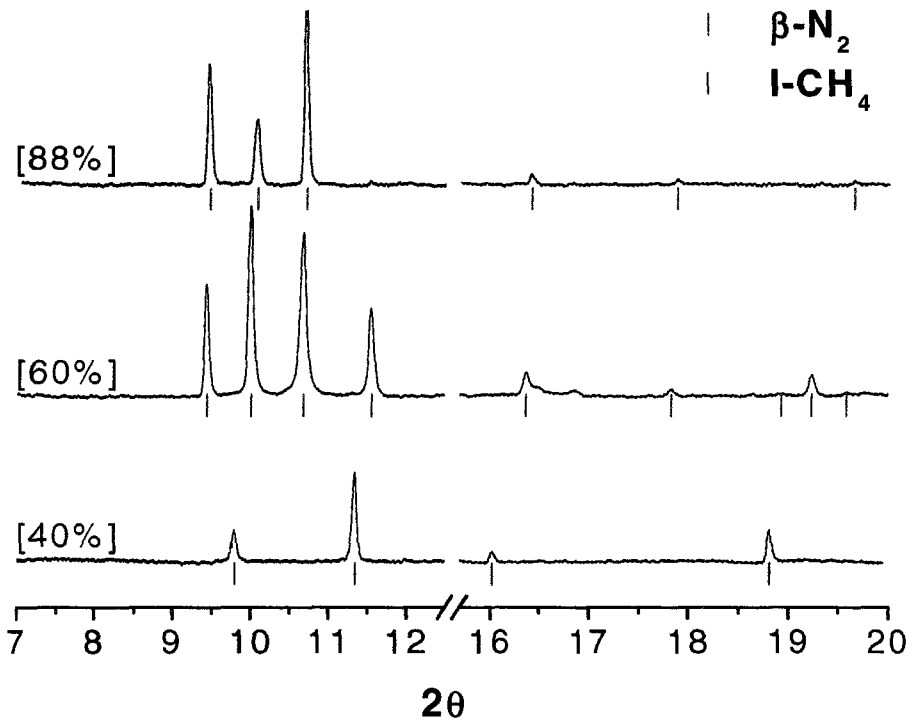

Figure 4.8: XRD patterns of different mixtures to display the three different observations: the β* phase, the I* phase, and a mixture of both occurring only in the 60% mixture. The red tick marks represent reflection positions of the β-nitrogen phase and the blue tick marks show the reflection positions for phase I of methane. All XRD patterns are acquired at approximately 4.7 GPa. Slight variation in pressure and concentration (thus affecting the lattice parameter) cause a shift in peak position.

Typically, the XRD image is acquired a short time after the pressure is changed on the DAC containing the mixture. The XRD pattern displaying reflections from both phases could be a result of the mixture settling into its equilibrium state, which could consist of one of these phases. This could also result from the existence of regions in which the concentration differs. Overall, it cannot be determined whether a mixture of phases *should* exist at these thermodynamic conditions (p, T, x), however, reflections from both phases are present. Fig. 4.8 shows the XRD pattern of three different mixtures around 4.7 GPa and the corresponding reflections for each phase. It is apparent that the diffraction pattern of the 60% mixture requires indexing of both phases to account for all reflections.

4.3 Nitrogen and Methane Phases in the Mixed System

Nitrogen and methane experience a phase transition from the first solid phase at 4.9 GPa [Schneider, 1992] and 5.2 GPa [Bini, 1995], respectively. In the nitrogen-rich side of the mixed phase diagram, phases resembling the δ and δ_{loc} phases of nitrogen exist (> 70%), though no evidence for the ε phase is observed. Phase A of methane is found only at very high methane concentrations (10% nitrogen) and phase B is seen throughout the methane-rich portion of the phase diagram (as phase B* for concentrations < 50%).

4.3.1 The δ* Phase

In pure nitrogen, the δ phase exists above 4.9 GPa at room temperature [Schneider, 1992]. This phase is also seen for mixtures of high nitrogen concentration. Although possibly existing at lower concentrations, it has been observed as the predominant phase in a mixture of 88% along with the T_1 compound. The solubility of methane molecules in the δ* phase of nitrogen is appreciably lower than in the β* phase, which could hold up to 40% methane. Even a small amount of methane dissolved into the δ* structure causes an increase in volume (refer to Fig. 4.9.).

This shift in molecular volume (Fig. 4.9) for high nitrogen concentrations implies that there is some, although low, solubility of methane in δ-nitrogen. This low solubility could result from the different types of disorder of nitrogen molecules within the δ-structure. In this, two of the eight nitrogen molecules possess spherelike disorder and the remaining six possess disklike disorder. The substitution of methane molecules on sites with disklike disorder would thus create a significant difference in effective geometry, causing the packing efficiency to be lowered and the molecules to be closer together. This is less energetically favourable and could cause the expansion of the lattice as the methane molecules are slightly larger. This unfavourable substitution also leads to a low solubility compared to the β-structure, in which all molecules exhibit spherical disorder.

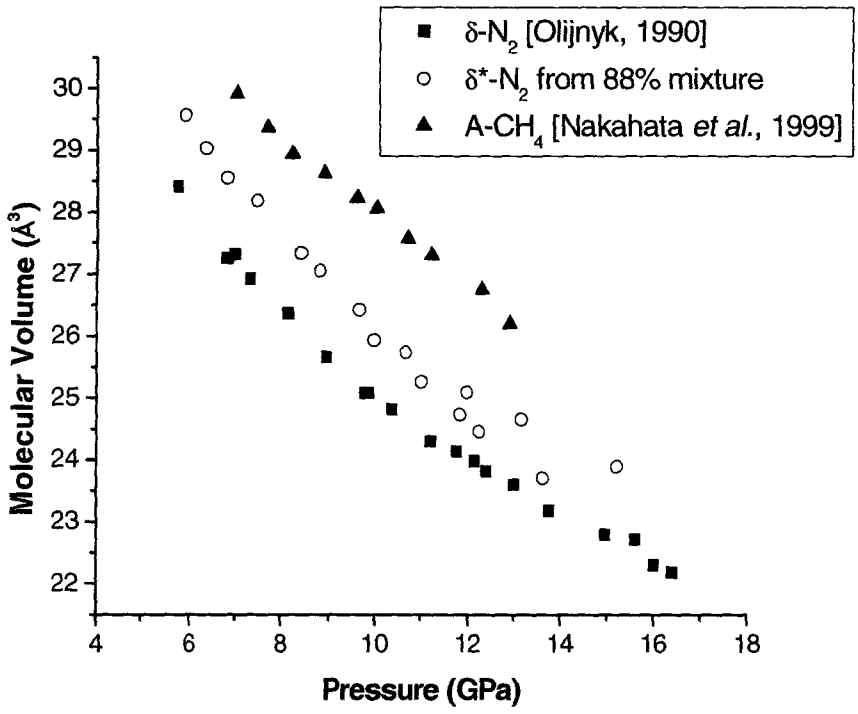

Figure 4.9: The molecular volume of δ*-N_2 in the 88% mixture (this work) compared to the published values of the pure molecular volume of nitrogen and methane. The inconsistency observed above 11 GPa for the mixture is due to hysteresis, as this includes results from compression and decompression.

The exact concentration of methane that can be dissolved in the δ* phase is unclear. With 12% methane, the T_1 phase is formed as a minor phase. So, the amount of methane in the δ* phase must be less than 12%. The amount of the T_1 compound relative to the δ* phase cannot be determined due to the overlap of reflections, as shown in Fig. 4.10. However, in order to form the T_1 compound, there must be very little methane in the δ* phase.

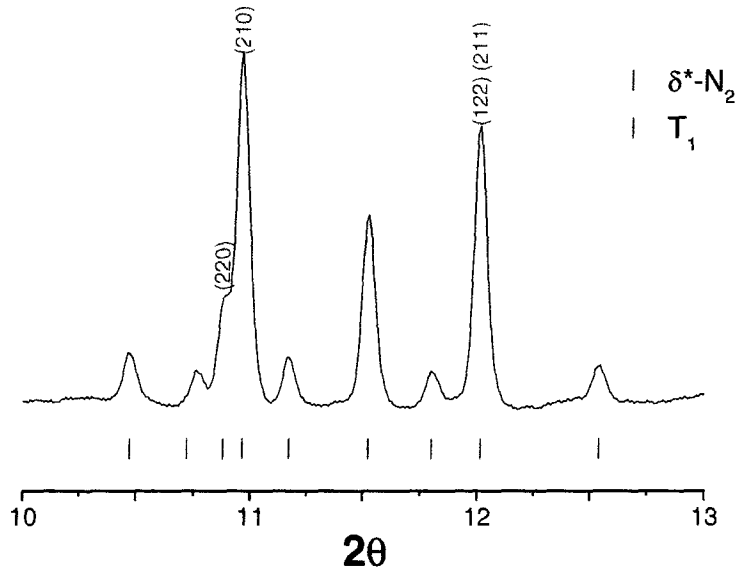

Figure 4.10: The XRD diffraction pattern of the 88% mixture at 9.67 GPa shown to highlight the unambiguous existence of the δ* phase. The tick marks, representing the reflections of each phase, are predicted based on the lattice parameters of a = 5.957 Å for the δ* phase (red tick marks) and a = b = 11.504 Å, c = 6.075 Å for the T_1 phase (blue tick marks).

The overlap of reflections, seen in Fig. 4.10, occurs because the lattice parameter of δ nitrogen is similar to the c parameter of the T_1 compound (here, a(δ) = 5.957 Å and c(T_1) = 6.075 Å). The two most intense, the (210) and (211) reflections of the δ* phase are shown. These appear very close to the (220) and (122) reflections of T_1. Consequently, it is difficult to distinguish the relative amounts of each phase. From the XRD pattern of the 88% mixture, it is clear that the δ* phase is the predominant phase. For mixtures of lower nitrogen content, the contribution from the δ* phase will be smaller, and accordingly these reflections may not be decipherable from the reflections of the T_1 phase. The Le Bail fit of this phase mixture is shown in Fig. 4.11 for an 88% mixture and confirms the existence of this phase mixture.

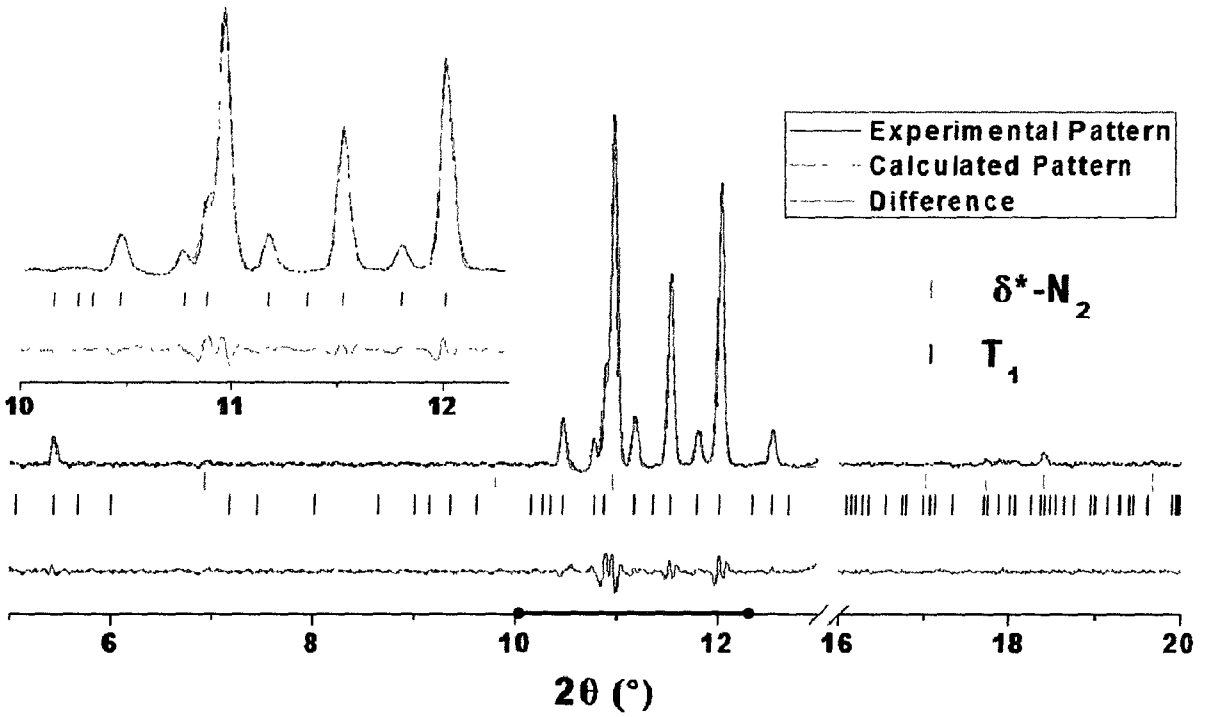

Figure 4.11: Le Bail fit of the XRD pattern of the δ* and T_1 phases at 9.67 GPa for the 88% mixture. The plot in the top right corner represents an expanded view from 10° to 12.2°.

Other nitrogen-rich concentrations studied include 71%, 64% and 60%. Because of the few reflections associated with the δ* phase and the coincidence with reflections from T_1, the existence of both phases cannot be ruled out. In the 71% mixture, the reflections that would be coincident in both phases are somewhat asymmetric (Fig. 4.12) implying that some crystals or crystal regions may assume the δ* structure. This occurs only at two of the pressures studied, both around 7 GPa, which is the maximum pressure studied. Diffraction patterns at lower pressure show no suspicious asymmetry. Hence, at these lower pressures the existence of δ*-nitrogen cannot be verified. The resolution may not be significant enough to distinguish between the two phases. However, this could also imply that nitrogen becomes less soluble in T_1 as the pressure increases, causing the system to form a phase mixture above 7 GPa.

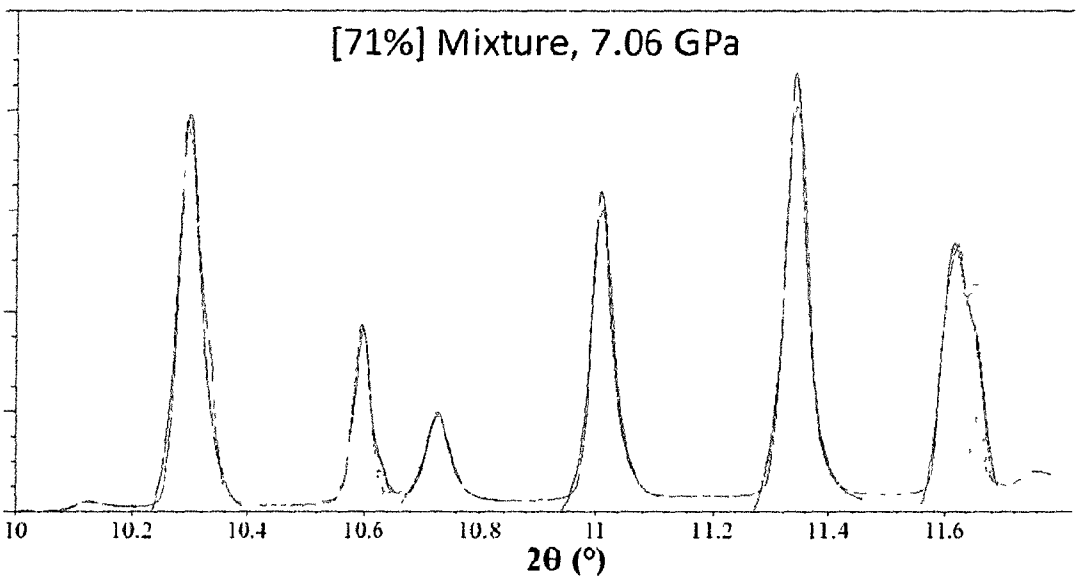

Figure 4.12: This is an image taken from XRDA indexing software of a 71% mixture. The two (*hkl*)s indicated correspond to reflections from δ-nitrogen. Note the asymmetry in reflections fit in red and the remaining reflections from the T_1 phase fit in green for visual comparison.

Because the lattice parameter of δ-N_2 is close to the c parameter of the T_1 phase, the two phases may be related. It is possible that, after substituting a sufficient amount of methane into the δ-N_2 structure, the structure distorts, expanding along the a and b axes, and appears as the tetragonal phase observed. The presence of both phases in the nitrogen-rich mixture may be explained by the existence of regions of varying nitrogen concentration as opposed to a true phase mixture. In some regions, a smaller amount of methane could result in the stability of the δ* phase. Other regions higher in methane concentration could cause the distortion of the δ* phase and result in the T_1 compound. This, however, cannot be confirmed.

4.3.2 The δ_{loc}* Phase and ε Nitrogen

In pure nitrogen, the δ phase is observed until 10.5 GPa at which additional reflections appear [Hanfland, 1998]. This phase represents a tetragonal distortion of the δ phase. The 88% mixture was the only mixture in which the δ phase was confirmed without doubt and studied above this pressure. The additional reflections distinguishing the δ and δ_{loc} phases are weak. Thus if these reflections overlap with any of the reflections from the T_1 compound, the transition would be difficult to confirm. In spite of this, evidence shows that for the 88% mixture at 15.21 GPa, the δ_{loc} phase is observed (Fig. 4.13).

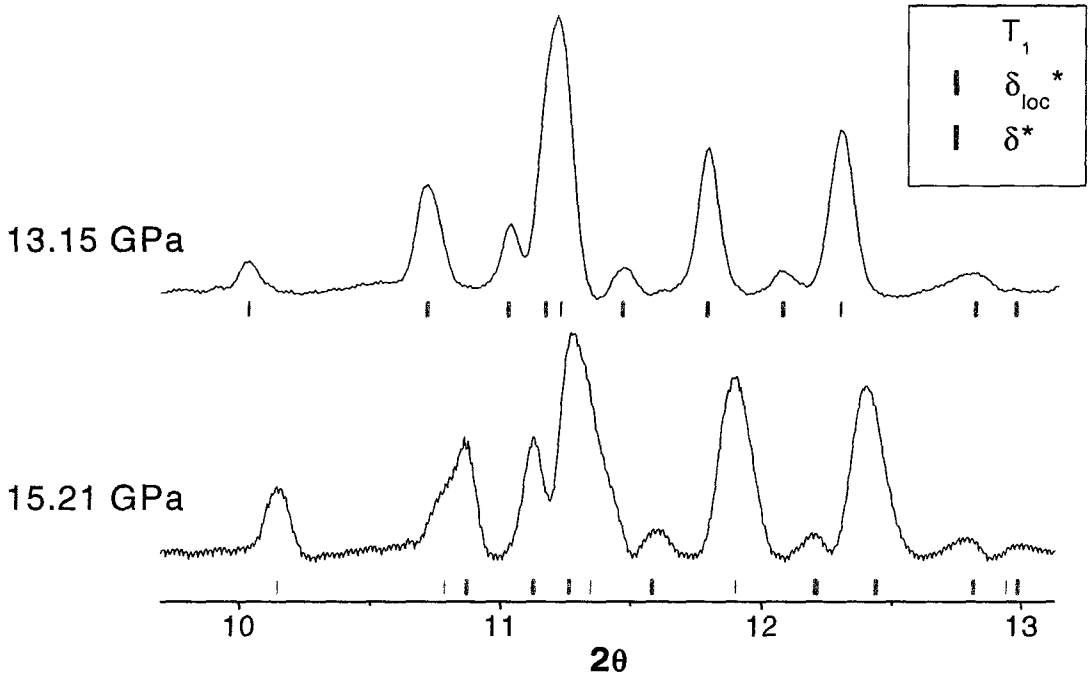

Figure 4.13: XRD images of the 88% mixture. The increase to 15.21 GPa indicates the existence of the δ_{loc} phase.

The pronounced asymmetry of the reflection at 10.9° coincides with one of the additional reflections that mark the transition into the δ_{loc} phase. This is seen only at this pressure, above which no data was acquired. This pattern is also subject to a large amount of broadening due to the

stress on the sample, which normally fails prior to reaching this pressure. In spite of the broadening, the asymmetry of the peak appears to be due to an additional reflection.

The data taken of the 88% mixture at 15.21 GPa was during compression. An XRD pattern acquired at 13.62 GPa upon decompression shows no signs of the δ_{loc} phase. Thus, the transition into the δ_{loc} phase likely occurs between 14 and 15 GPa in the mixture, a few GPa above the transition in pure nitrogen. The molecular volume determined for the δ phase around 15 GPa is 22.786 $Å^3$/mol [Olijnyk, 1990] which should be similar to the δ_{loc} phase. Here, the molecular volume is 23.871 $Å^3$/mol, which is slightly higher. This would imply that the methane substitution causes the lattice to expand in the δ_{loc} phase, as it does in the δ phase.

The ε-nitrogen phase exists above 17 GPa and possesses a rhombohedral structure [Olijnyk, 1990]. It is not observed in this work, as it is outside the relevant pressure range. Furthermore, based on the upward shift of most transitions observed compared to the pure species, this phase would likely not be observed until even higher pressures.

4.3.3 The A* Phase

Phase A of methane was observed in only one XRD image in a 10% mixture. Indexing was done using a hexagonal lattice and a Le Bail fit (Fig. 4.14) of the XRD data confirms that the fit is successful. The XRD image was composed of many spots, indicating that the powder contained large grains, which is described as typical of methane.

The XRD pattern here matches that of A-CH_4. This phase is not observed for any other pressure or mixture. Hence it appears that the substitution of nitrogen decreases the stability of phase A, relative to phase B, which is observed over a wide range of concentration and pressure. Nevertheless, a concentration of 10% nitrogen does not affect the molecular volume of the A phase. The molecular volumes for I- and A-CH_4 are plotted in Fig. 4.15 with the observed results. It fits into the equation of state without any notable volume reduction, as seen in the I* phase.

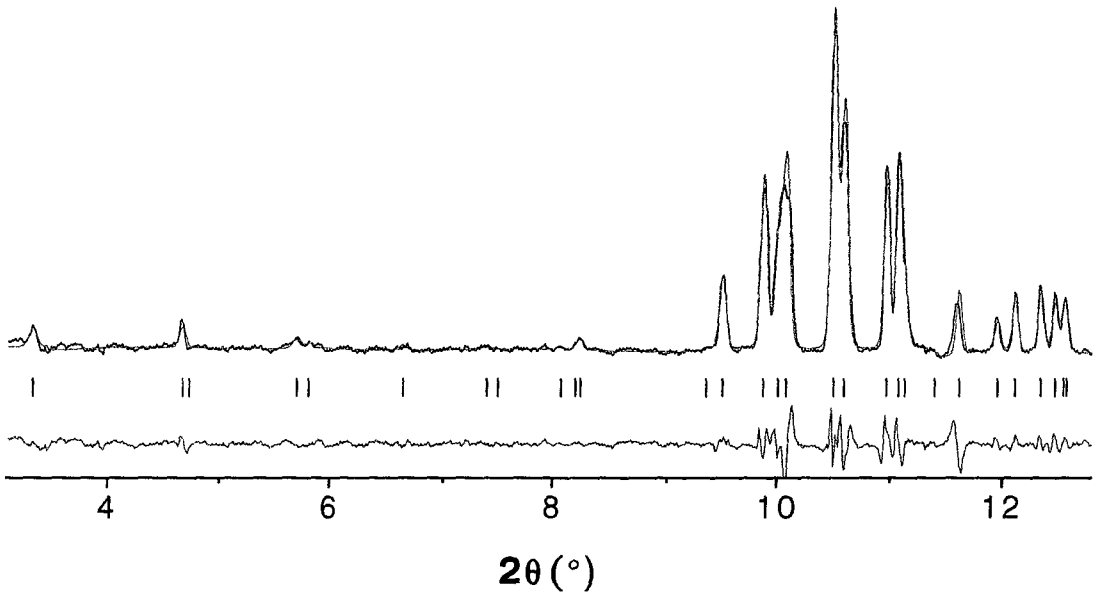

Figure 4.14: A Le Bail fit of the XRD pattern of a 10% mixture at 5.6 GPa in the A* phase. The fit used a hexagonal unit cell in the R3 space group with a = b = 12.298 Å and c = 15.383 Å. The peak around 11.8° may be superimposed with a contaminant peak from the diffraction of ruby or water (which explains why the A* lattice cannot properly describe this peak).

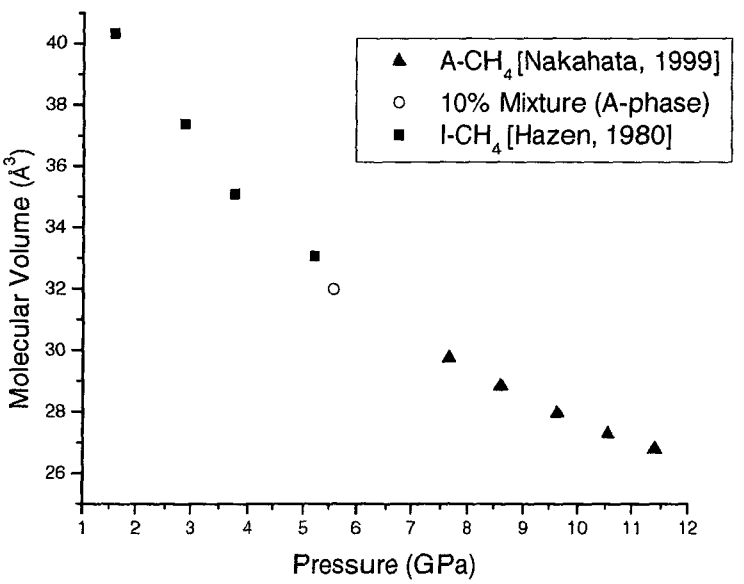

Figure 4.15: The molecular volume of methane compared to the observed molecular volume of the A phase at 5.6 GPa, as seen in a 10% mixture.

4.3.4 The B* Phase

Phase B of methane has not been given much attention in terms of structural study. In the nitrogen-methane mixtures, its unit cell is identified over a range of concentrations and it appears as a predominant phase for mixtures below 20%. It appears with both compounds, but it does not exist with any pure nitrogen phases. The addition of nitrogen molecules seems to promote the formation of the B* structure over the A* phase, which is not seen above 10%. Yet, the significant hysteresis involved in the A to B transition could also be responsible for this.

Between 10% and 50%, the B* phase co-exists with one compound or the other in a phase mixture that depends on pressure and concentration as well as kinematics. The results differ for compression and decompression and this is likely due to the strong hysteresis and the observation that the B* + MR to B* + T_1 transition is time-dependent. This is discussed in section 5.1.3.

Recent studies [Sun, 2009] agree with the unit cell of B-CH_4 bring indexed as a cubic structure with lattice parameter 7.914 Å at 16.9 GPa [Umemoto, 2002]. Conversely, Maynard-Casely claims that there is evidence for a larger unit cell. Based on additional weak reflections, it was concluded that the lattice parameter needed to be extended by approximately √2 [Maynard-Casely, 2009]. As the B phase is not observed as a single phase in any of the mixtures studied, this cannot be confirmed or debated.

The 10% mixture contains a phase mixture of B* and the MR compound above 8 GPa. The XRD pattern of the MR compound is extremely weak in comparison with the B* phase, and so it makes up a small fraction of the sample. The XRD pattern clearly matches that of a 36% mixture containing the MR compound, shown in Fig. 4.16. The Le Bail fit of this XRD pattern is presented in Fig. 4.17.

As with methane in δ-N_2, the solubility of nitrogen in the B-CH_4 structure is low. It is difficult to estimate the relative amounts of both phases. In the 10% mixture, a minor amount of the MR compound is observed in addition to B*-CH_4. This minor amount is defined by the fact that the diffraction peaks are very weak compared to those of B*-CH_4. It is estimated that the solubility of nitrogen in B-CH_4 is about 8%.

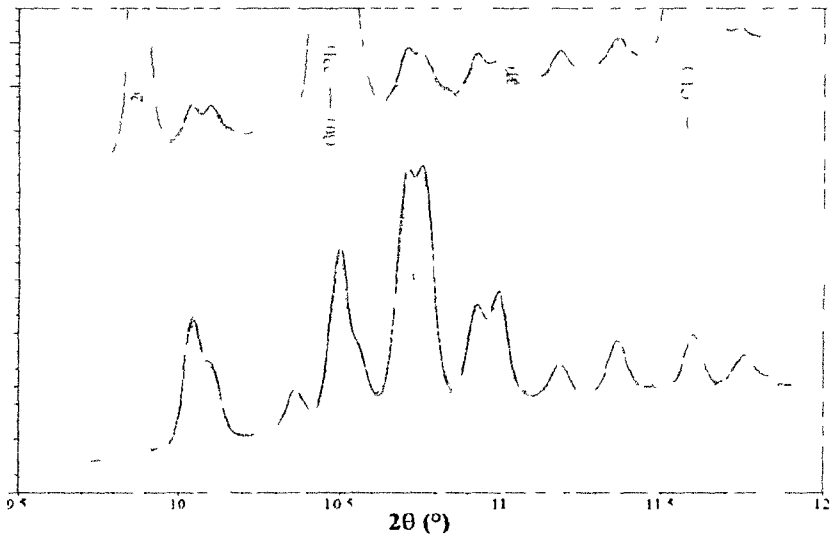

Figure 4.16: Comparing the XRD pattern of a 10% mixture at 9.30 GPa (top – B*-CH_4 + MR) with an XRD pattern from a 45% mixture at 9.00 GPa (bottom – MR phase only). The Miller indices are those of the B* phase, corresponding to a cubic cell length of 8.373 Å. This is observed over a range of pressures, from 8.46 GPa to 12.97 GPa. Note: the dotted lines represent the deconvoluted peaks that are overlapping, and in some cases they display the background level (when they are along the bottom of the peaks).

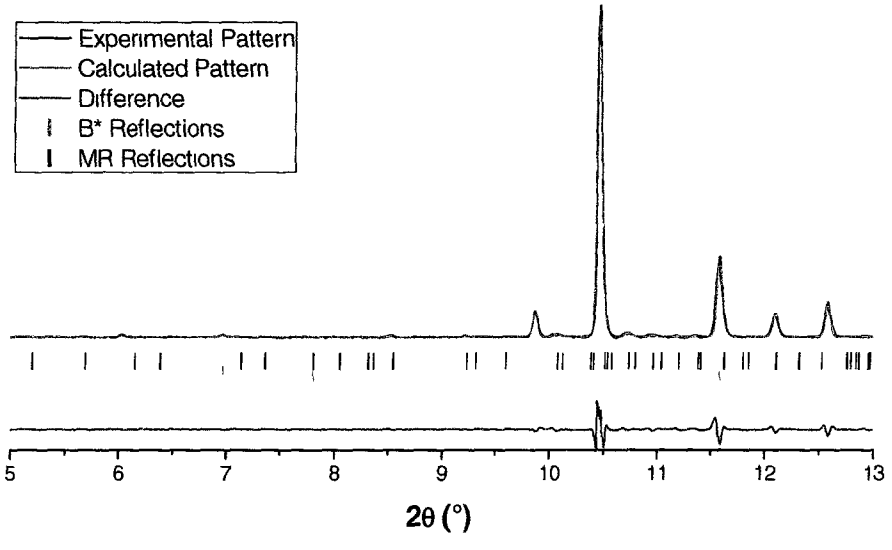

Figure 4.17: A Le Bail of the XRD pattern of a 10% mixture at 8.46 GPa in the B* + MR phase mixture.

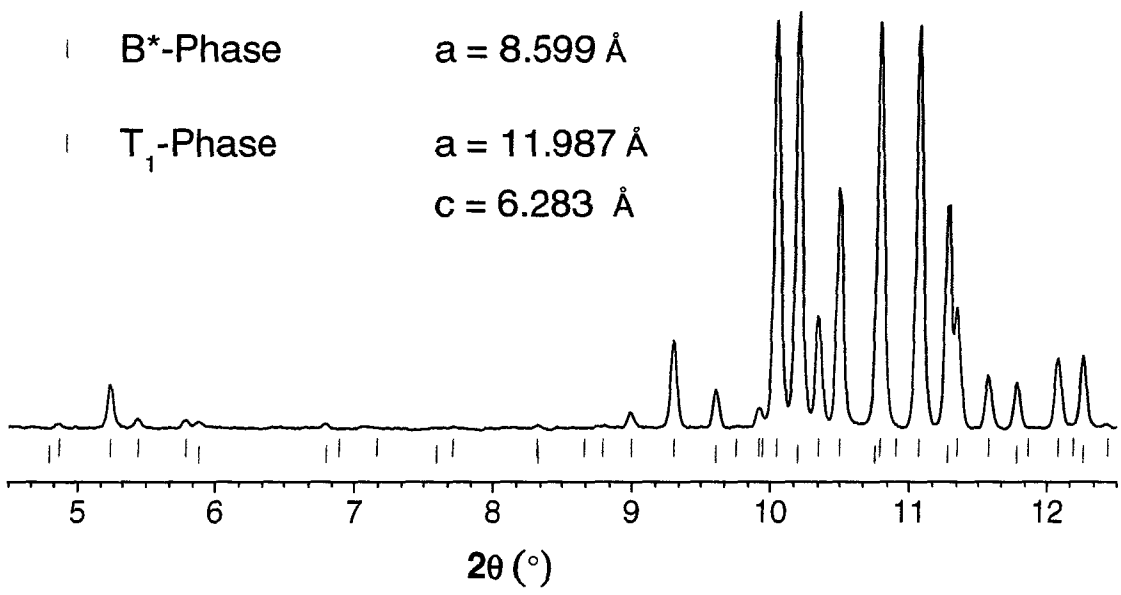

Figure 4.18: The XRD pattern of a 45% mixture at 6.12 GPa. Indexing provides evidence of the coexistence of the B* phase with the T_1 compound. The *P42/mnm* space group is assumed for T_1 and the *Pm3m* space group used for the B* phase.

The B* + T_1 mixtures (Fig. 4.18) are observed consistently between the first solid region and up to 8 GPa (although this transition is subject to hysteresis – see section 5.1.3). Fig. 4.18 shows the indexed pattern of this phase mixture. All observed reflections can be accounted for using a unit cell similar to B-CH_4 as proposed by Nakahata *et al.* [Nakahata, 1999], and do not require the additional reflections predicted for the larger unit cell proposed by Maynard-Casely [Maynard-Casely, 2009].

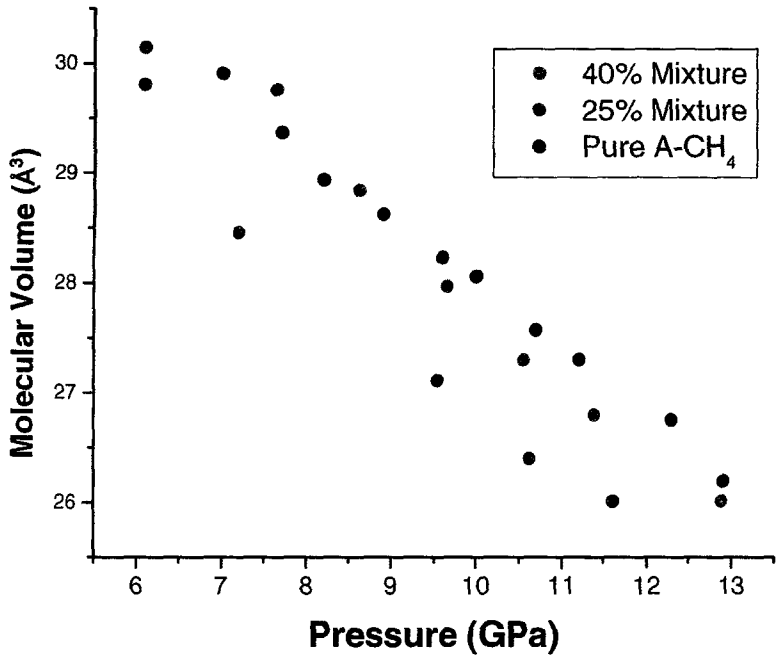

Figure 4.19: The molecular volumes of the B* phase compared to the pure molecular volumes of A-CH_4 [Nakahata, 1999] which is normally observed in this pressure range. The B* phase is observed with the T_1 compound.

Fig. 4.19 shows the molecular volume of the B* phase in the B* + T_1 phase mixture. The molecular volume is compared to that of the A phase since this is the phase observed in this pressure range for pure methane. In the 25% mixture, the B* phase is the predominant phase (the reflections from this phase are much more intense from those of T_1) and in the 40% mixture the two phases exist in similar amounts. As the T_1 compound is nitrogen-rich, we can conclude that there is more nitrogen substituted in the B* lattice in the 25% mixture than in the 40% mixture (as most of the nitrogen is contained in the T_1 compound, thus the B* phase has a molecular volume similar to that of pure methane).

4.4 A Novel van der Waals Compound: The T_1 Compound

The T_1 phase exists over a wide range of concentrations and pressures in the nitrogen-methane binary system. It is observed in mixtures as low as 25% with an additional pure methane phase, as a single phase, with the second (MR) compound, and with a pure nitrogen phase to concentrations up to 88%. This phase is stable at pressures above the first solid-solid transition and above 40% remains stable up to the highest pressures studied, i.e. 16 GPa.

In the described range, the XRD pattern does not correspond to that of either pure phases of nitrogen or methane, or any combination of them. This is clear simply by visual comparison (see Fig. 4.20). Although it may appear that reflections from δ-N_2 could account for a small number of peaks, A-CH_4 is not an appropriate candidate to account for the rest. Additionally, the reflections of both δ-N_2 and A-CH_4 cannot account for the number of reflections observed at low angles (not shown). Low angle reflections are important in defining a unit cell. Moreover, reflections from δ_{loc}-N_2 and B-CH_4 cannot explain the observed XRD pattern either.

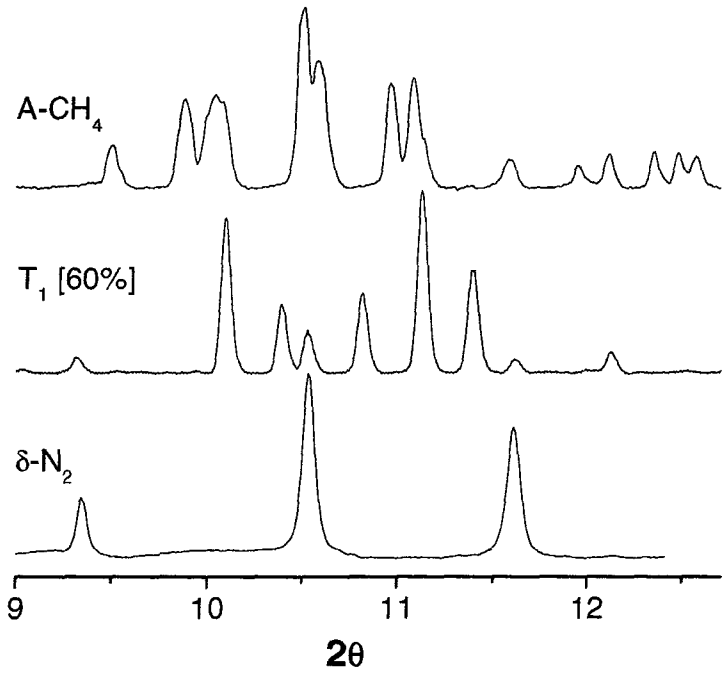

Figure 4.20: Comparison of the XRD patterns of pure nitrogen and pure methane to that of the proposed T_1 compound. The pattern of A-CH_4 is that from a 10% mixture, which has been confirmed as solely the A phase and the pattern of δ-N_2 is taken from a pure nitrogen sample. Inspecting these patterns leads to the conclusion that the phases of the pure components that are expected in this pressure range at room temperature are insufficient for describing the observed XRD pattern of T_1.

4.4.1 Proposed Unit Cell

From the evidence presented above, the observed XRD pattern is not that of a mixture consisting of the pure phases of nitrogen and methane. Using the Crysfire suite of indexing programs [Shirley, 2000], many solutions for possible unit cells are generated. The unit cell that was chosen as the best candidate is a tetragonal cell with parameters a = 11.924 Å and c = 6.266 Å at 7.06 GPa for a 60% mixture, which is consistent with multiple data sets for different mixtures. Most of the other generated solutions include lattice parameters that are multiples of this unit cell or very similar. Along with the solutions, a figure of merit is offered as an indicator of the "goodness of fit" provided by the unit cell (solutions with a merit above 50 are considered good fits).

Table 4.1 displays an example of unit cell solutions proposed by Crysfire after inputting the positions of the reflections observed in an XRD pattern of a 60% sample at 7.06 GPa. The majority of these solutions have lattice parameters that are very similar to those chosen; the orthorhombic solutions with a high figure of merit include two very similar lattice parameters that are close to the a and the other close to c of T_1. The Crysfire program contains several different codes (representing different algorithms) for determining unit cell parameters. Therefore, similar sets of lattice parameters can be assigned different figures of merit. The figure of merit indicates the plausibility of a solution based on the fact that there is agreement between its calculated reflection positions and those that were input. These values are affected by the number of reflections input and the volume of the solution (generally a higher volume unit cell contains more possible reflections and thus it is easier to match observed and calculated reflections—Crysfire gives a lower figure of merit for higher volume solutions to account for this). It therefore requires further analysis to choose a solution: by manually indexing the pattern using the proposed solutions one can make a more informed decision on which solution to choose. After fitting the pattern, the lattice parameters for the tetragonal cell were determined to be 11.924 Å, 11.924 Å and 6.266 Å.

The goodness of fit of the choosen solution is demonstrated using a Le Bail fit in Fig. 4.21, Fig. 4.22 and the corresponding d-spacings are presented in Table 4.2. All observed reflections are accounted for, and the average difference between the observed and calculated d-spacings is about 0.00050 Å (or ± 0.02%), which suggests with high confidence that this unit cell is correct.

Table 4.1: Proposed Solutions from Crysfire

Merit	Volume (Å^3)	Unit Cell	a (Å)	B (Å)	c (Å)	α (°)	β (°)	γ (°)
77.6	890.9	Tetragonal	11.925	11.925	6.265	90	90	90
73.1	890.9	Tetragonal	11.924	11.924	6.266	90	90	90
67.8	890.9	Orthorhombic	6.266	11.922	11.927	90	90	90
67.7	890.9	Orthorhombic	6.266	11.922	11.927	90	90	90
67.5	890.8	Orthorhombic	6.266	11.920	11.927	90	90	90
67.2	890.8	Orthorhombic	6.266	11.920	11.927	90	90	90
58.6	484.4	Monoclinic	6.815	11.922	6.486	90	113.2	90
50.6	890.3	Orthorhombic	11.922	11.922	6.264	90	90	90
49.7	890.3	Orthorhombic	11.922	11.922	6.264	90	90	90
49	891.2	Tetragonal	11.924	11.924	6.268	90	90	90

Table 4.1: The solutions for possible unit cells obtained after running Crysfire. Solutions of lower merit (< 49) are discarded. The second solution is chosen after indexing. The first and second solution, however, have parameters that differ by 0.001 Å, which is on the order of uncertainty, and thus are effectively the same.

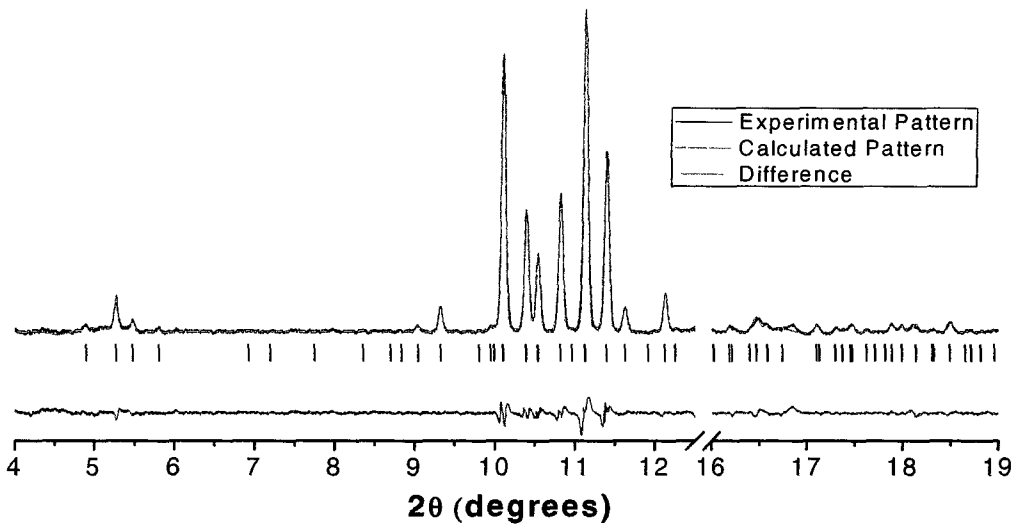

Figure 4.21: Le Bail fit of the XRD pattern of the T_1 phase (60% mixture) at 7.06 GPa with a = b = 11.924 Å, c = 6.266 Å.

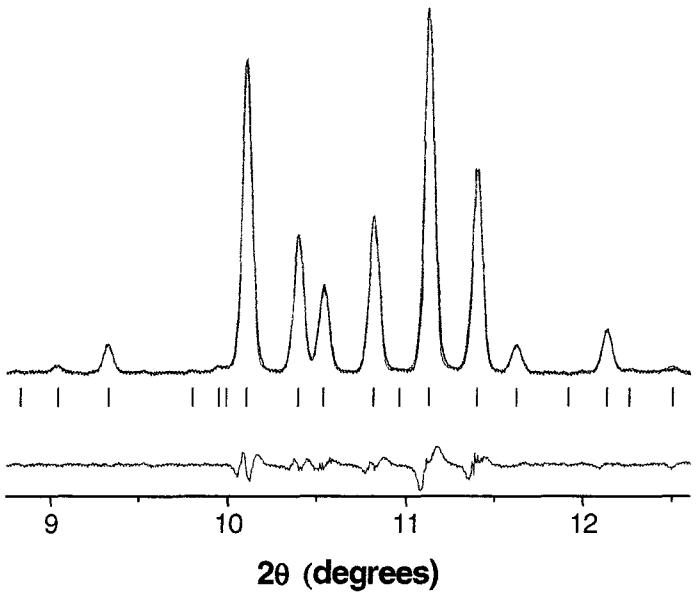

Figure 4.22: Expanded view of the Fig. 4.21 to highlight the goodness of fit provided by the proposed unit cell.

Table 4.2: The tabulated observed and calculated d-spacings (Å) for the fit provided by the proposed unit cell. The difference between the observed and calculated d-spacings (Å), displayed in the rightmost column, are quite small, averaging only a ± 0.02% deviation.

Table 4.2: Observed and Calculated d-Spacings for the T_1 compound			
hkl	d_{obs}	d_{calc}	$d_{obs} - d_{calc}$
200	5.9639	5.9656	0.00171
011	5.5475	5.5480	0.00046
210	5.3323	5.3318	-0.00050
111	5.0301	5.0308	0.00064
221	3.4988	3.4997	0.00087
311	3.2308	3.2307	-0.00013
002	3.1329	3.1327	-0.00025
400	2.9818	2.9825	0.00069
112	2.9375	2.9380	0.00052
410	2.8922	2.8924	0.00013
330	2.8106	2.8105	-0.00007
202	2.7729	2.7722	-0.00065
212	2.7009	2.7005	-0.00047
411	2.6253	2.6247	-0.00061
331	2.5639	2.5634	-0.00055
222	2.5141	2.5135	-0.00063
312	2.4094	2.4090	-0.00045
500	2.3856	2.3863	0.00072
322	2.2745	2.2744	-0.00006
501	2.2285	2.2281	-0.00040
511	2.1906	2.1903	-0.00034
313	1.8278	1.8285	0.00066
522	1.8077	1.8071	-0.00061
323	1.7667	1.7673	0.00065

4.4.2 Stoichiometry and Equation of State

The T_1 phase is observed over a wide range of concentrations in the phase diagram, as low as 15% to as high as 88%. For concentrations of 57%, 60% and 64% it is observed without indication of a phase mixture. For a 71% mixture, T_1 likely coexists with δ-N_2, and in a 49% mixture, T_1 is seen in addition to the MR compound. The region between these two concentrations mark the stability range of T_1 as a single phase, and thus the concentration of nitrogen in the compound is suggested to be 60%. This gives a stoichiometry of $(N_2)_3(CH_4)_2$, assuming that the volume ratio is approximately equal to the molar ratio (note: this does not imply that there are 3 molecules of nitrogen, but the overall ratio of nitrogen to methane is 3 to 2).

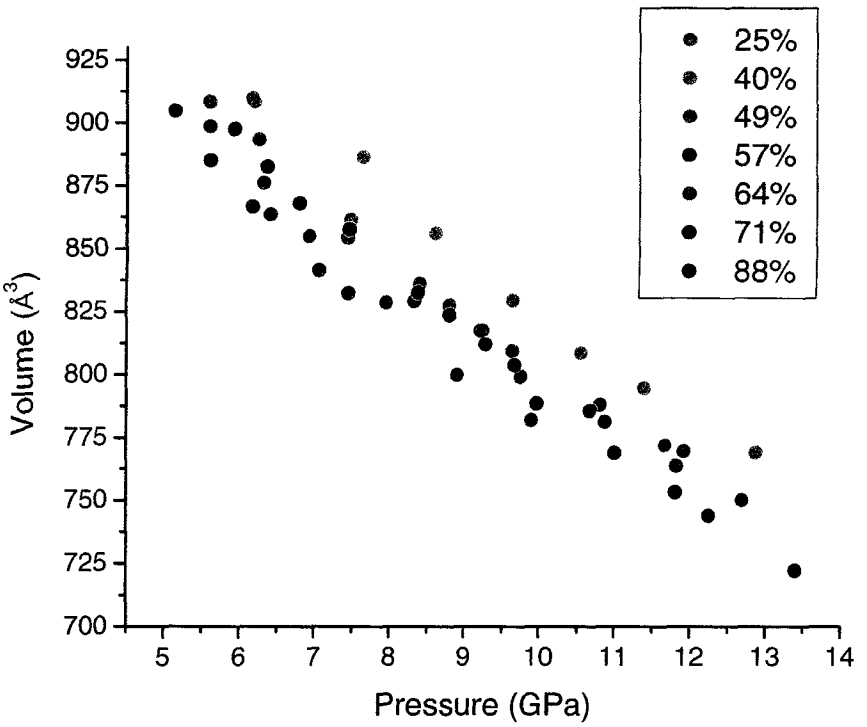

Figure 4.23: Equation of state of T_1 in different mixtures: unit cell volume over pressure.

Fig. 4.23 displays the unit cell volume of the T_1 phase measured for different mixtures. In general, the samples with higher methane concentrations (25%, 40%, 49%) possess larger volumes than those with higher nitrogen concentration (57%, 64%, 71%), as would be expected. However, it cannot be trivially stated that the increase in methane concentration causes a proportional increase in T_1 volume. Due to the existence of different phase mixtures, the concentration of nitrogen of the sample does not directly provide the concentration of nitrogen in the compound.

The unit cell volumes of the 57%, 64% and 71% mixtures show a small, consistent decrease with concentration. This can be attributed to nitrogen molecules replacing some of the methane molecules in the unit cell, just as the addition of nitrogen to B-CH_4 causes a volume reduction. The 88% mixture does not follow this trend, since it contains more δ-N_2 than T_1. The T_1 compound that is observed in the 88% mixture is expected to have the predicted 3 to 2 ratio of nitrogen to methane.

The 49% mixture exhibits a phase mixture of the T_1 and MR compounds and shows a similar equation of state as the 57% mixture. The similar volumes suggest that the stoichiometry in the T_1 compound in the 49% and 57% mixtures are the same. The samples with concentrations of 25% and 40% possess different phases upon compression and decompression. Upon decompression, a mixture of B* + T_1 phases exists (hysteresis is responsible for this, see section 5.1.3).

The 40% sample is particularly interesting. The unit cell volumes for T_1 that co-exists with the MR compound (not shown in Fig. 4.23) are quite similar to that of the 49% mixture. However, the unit cell volume for T_1 in the phase mixture with the B* phase is much larger. In fact, compared to the 57% mixture, the unit cell volume of T_1 (in the T_1 + B* mixture) is consistently 30 Å larger, which is approximately the molecular volume of one methane molecule at these conditions. This implies that the T_1 compound observed with the B* phase in the 40% sample contains an additional molecule; this state is likely less stable and is observed because the sample is not in equilibrium.

In order to compare the volume of T_1 to the pure species, the molecular volume must be calculated from the number of molecules. Taking the quotient of the volume of the unit cell and the weighted molecular volume of the components at the same pressure ($0.6V[N_2] + 0.4V[CH_4]$) yields the approximate number of molecules within the unit cell.

At 7 GPa, methane has a molecular volume of 30.74 $Å^3$/mol [Nakahata, 1999] and nitrogen has a molecular volume of 27.31 $Å^3$/mol [Olijnyk, 1990]. For the 60% mixture at 7.06 GPa, this gives 31 molecules. Using volumes of different mixtures at different pressures yield results from 30 to 32 molecules. Of course, this assumes that the molecular volumes of nitrogen and methane are the same as in their pure form. For this phase to be favoured over the pure structures, the molecules may be arranged with higher packing efficiency than in the pure structures. Furthermore, the best candidates for space groups (section 4.4.3) would not be suitable for a 31 molecule structure. For these space groups, all Wyckoff positions require an even number of molecules based on symmetry. Out of the two remaining possibilities, 30 or 32 molecules, the 32 molecule structure is favoured based on efficient packing.

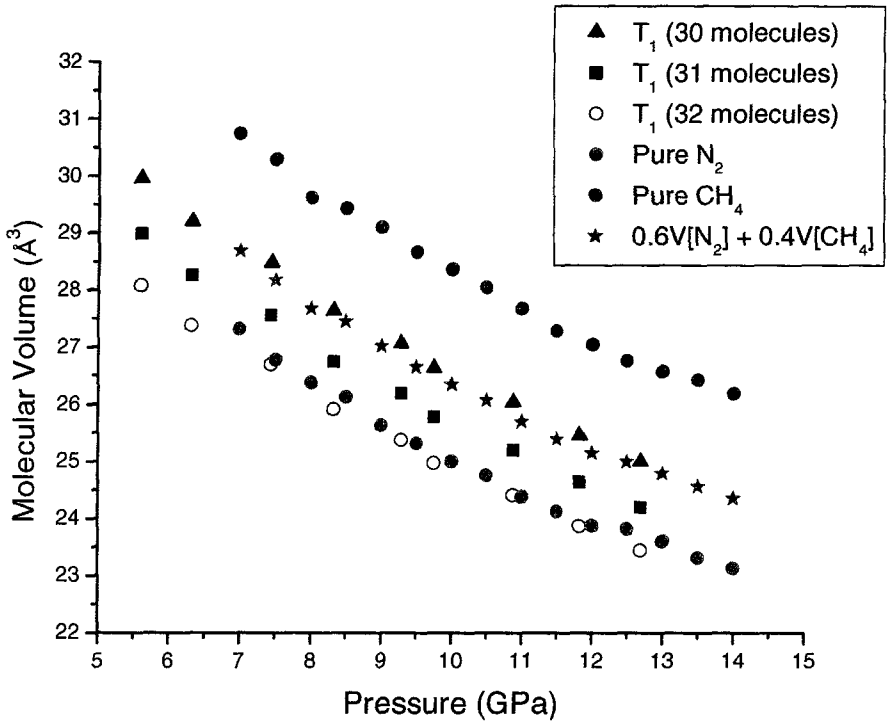

Figure 4.24: Molecular volumes of pure nitrogen [Olijnyk, 1990], pure methane [Nakahata, 1999], and a 57% mixture assuming 30, 31, and 32 molecules per unit cell.

The plot in Fig. 4.24 shows the equations of state for the compound with 30, 31, or 32 molecules in the unit cell compared to that of the pure species and a predicted equation of state for $(N_2)_3(CH_4)_2$. The data assuming 30 molecules is just above the estimated equation of state based on the weighted molecular volumes of the pure species. The volume-pressure relationship is fit in order to obtain equation of state parameters to compare to the pure species. With either a 30 or 32 molecule structure, the isothermal bulk modulus remains the same, but the extrapolated volume at zero pressure differs. The equation of state is fit using the third order Birch-Murnaghan equation of state (equation displayed in Fig. 4.25).

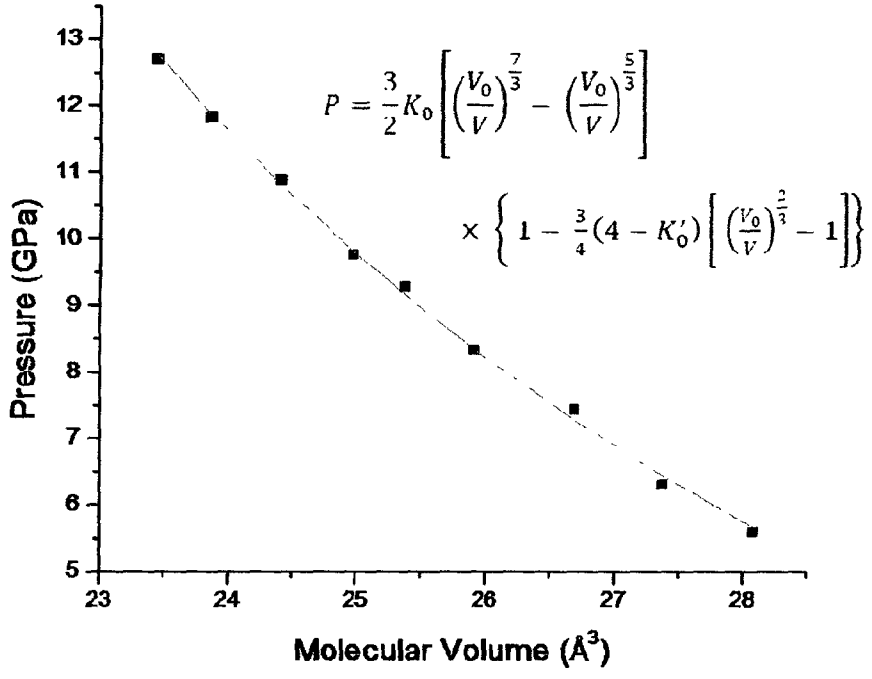

Figure 4.25: The equation of state curve for the T_1 compound in a 57% mixture. In the Birch-Murnaghan equation of state (formula shown) [Nakahata, 1999] the isothermal bulk modulus, K_0, and the volume at zero pressure, V_0 are fit keeping the derivative of the isothermal bulk modulus, K_0', set to 4, which is common for molecular solids. The parameters are listed in Table 4.3. This graph has pressure as a function of volume in order to comply with the form of the Birch-Murnaghan equation of state.

Table 4.3: Equation of State Fit Parameters

	N_2	57% (30)	57% (32)	CH_4
K_0 (GPa)	7.3	9.3	9.3	8.2
V_0 (Å^3)	41.2	41.3	38.7	45.5

Table 4.3: The equation of state parameters based on fitting the data of pure nitrogen from [Olijnyk, 1990], pure methane from [Nakahata, 1999] and the molecular volumes of the T_1 compound based on a 30 and 32 molecule structure.

The equations of state fit parameters are compared in table 4.3. The values for pure nitrogen were fit based on lattice parameters of Olijnyk [Olijnyk, 1990] and for pure methane from Nakahata *et al.* [Nakahata, 1999]. Errors for all parameters were about 0.5 GPa/0.5 Å^3 for all parameters. Results from the other mixtures ranged from 7 to 9 GPa for bulk modulus. In particular,

for the 57% mixture, the K_0 is somewhat higher than that of the pure species, implying that the T_1 compound is somewhat less compressible than the crystal structures of the pure species.

For the equilibrium volume, assuming 32 molecules led to a V_0 of between 40 and 41 $Å^3$, and for 30 molecules V_0 ranges from 41 to 43 $Å^3$. The quality of fit is strongly dependent on the number of data points, and for some mixtures, not many data points are available. Overall, it appears that for a 32 molecule structure, the equilibrium volume is lower than that of methane and close to that of nitrogen, whereas the 30 molecule structure has a zero pressure volume that is somewhere in between the pure species. The equations of state of the T_1 compound containing 30 molecules are consistent with the calculated equation of state for 60% nitrogen and 40% methane.

4.4.3 Space Group

A proposed space group for a structure must predict all observed reflections. Any additional reflections predicted by a space group may be too low in intensity to be distinguished in the experimental pattern or may be absent due to the distribution of atoms within the structure ("accidental absences"). In order to narrow down the space group(s) that best describe the experimental diffraction pattern of the T_1 compound, the lower angle reflections are more strongly considered. Reflections beyond 13° (all angles represent a value of 2θ) are not included since they become weaker in intensity, which is characteristic for X-ray diffraction experiments, and many reflections are overlapping at higher angles.

All reflections below 4° lie on a very uneven background. Since the beamstop in the center shields the detector from radiation, there is nearly zero scattered intensity between 0° and 2.3°, however due to scattering off the beamstop itself and the surrounding environment (air molecules) the background has a steep slope as opposed to a sharp edge between 2.3° and 3.5°. After this, it increases with a smaller, smoother slope. This is illustrated in Fig. 4.26.

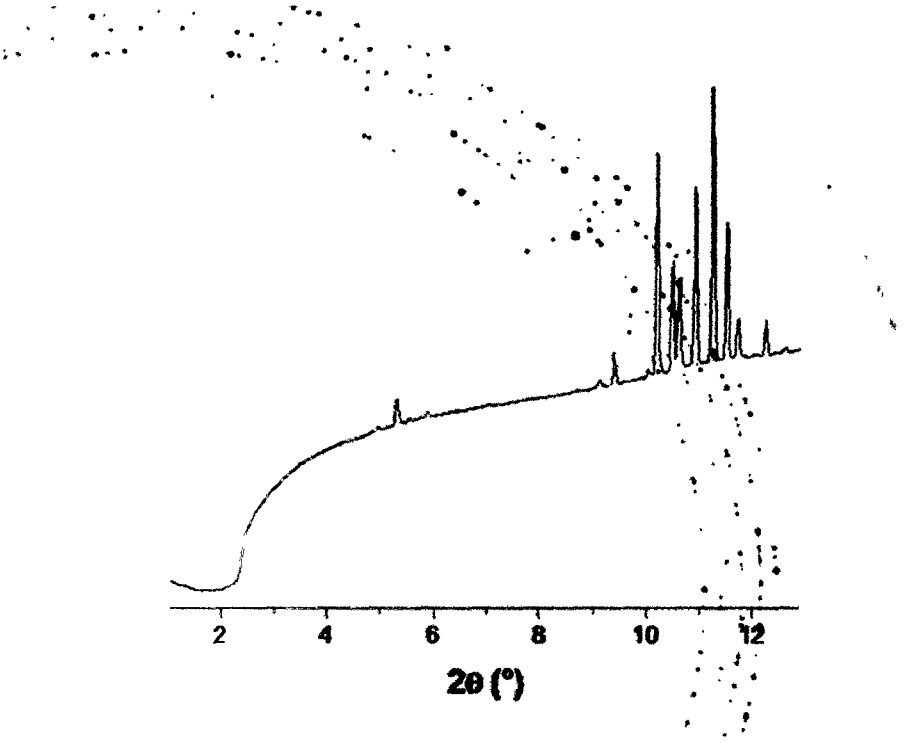

Figure 4.26: The XRD diffraction image of a 71% mixture at 6.17 GPa and the integrated XRD pattern over top. The low background in the XRD pattern corresponds to the area that is shielded from the beamstop.

In order to better investigate reflections in this low angle range, a modification was made to the CLS XRD set-up during the final set of experiments (July 2010). The beamstop was displaced slightly off center to allow the detector to collect some lower angle scattering. In order to ensure that the detector was protected from the direct beam, a lead plug, smaller in diameter than the beamstop, was placed in the center of the detector. This modification lowered the minimum visible angle by approximately 0.5° (down to almost 2°). With this modification, the first predicted reflection of the unit cell should be observable if it is present.

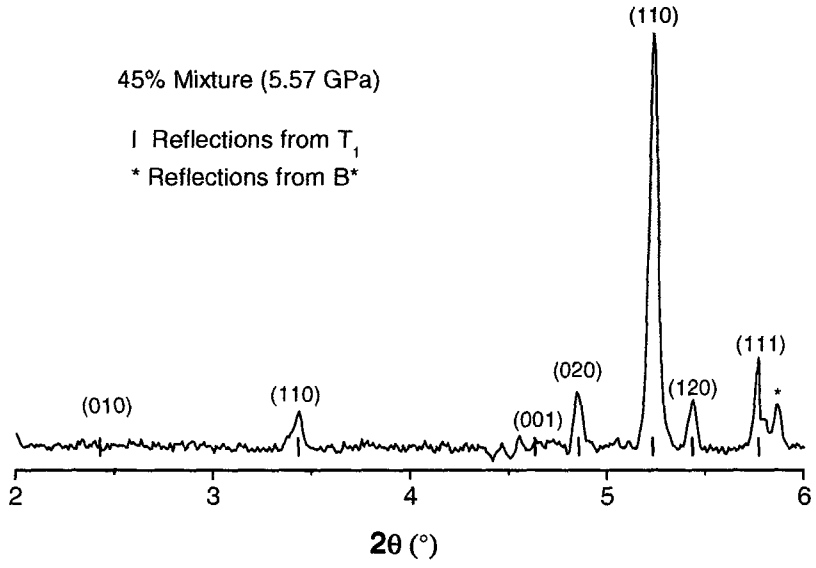

Figure 4.27: An XRD pattern of a 45% mixture at 5.57 GPa. The * refers to a peak from the B* phase and the reflections from the T_1 phase are marked.

The (110) reflection is weak and is not always observable, particularly with thinner samples (less than 120 μm), but the (001) reflection has never been distinguished over the background. If present, the (010) reflection should be observable after the modification is implemented. Thus, the space groups can be narrowed down to those omitting the (010) and (001) reflections, but including all others shown in Fig. 4.27.

After the (111) reflection, there are no well defined reflections until the (131) reflection around 9°, however all possible space groups include some reflections in this range. In some experimental XRD patterns, very weak reflections in this range can be seen, however they do not occur frequently enough to make conclusions with confidence regarding the space group. This results in space groups that predict the least amount of reflections in this range to be favoured.

Table 4.4: Possible Tetragonal Space Groups for T_1

Space Group	Omitting (010)	Omitting (001)
P4		
$P4_2$		✓
P-4		
P4/m		
$P4_2/m$		✓
P422		
$P42_12$	✓	
$P4_222$		✓
$P4_22_12$	✓	✓
P4mm		
$P4_2nm$	✓	✓
P-42m		
$P-42_1m$	✓	
P-4n2	✓	✓
P-4m2		
P-42m		
P4/mmm		
$P4_2/mnm$	✓	✓

Table 4.4: A list of possible tetragonal space groups is shown with those that omit the (010) and (001) reflections. These reflections are not expected to exist from the T_1 compound, so space groups with these absent are favoured. The space groups labelled in bold font are considered the best candidates for the T_1 compound.

Table 4.4 summarizes all the space groups that predict all observed reflections. It also indicates which space groups predict the (010) and (001) to be absent. Four space groups omit both of these reflections, three of which are predicted to be the best possible solutions by Chekcell: *$P4_2nm$, P-4n2,* and *$P4_2/mnm$*. These three space groups also predict fewer reflections than *$P4_22_12$*, and thus are the favoured solutions. The predicted reflections below 13° are identical for each of these three.

4.4.4 Structure

The T_1 compound has so far been described as a tetragonal unit cell with 30 to 32 molecules and the possible space groups *$P4_2nm$, P-4n2* or *P42/mnm*. In order to further define this compound, the positions of the molecules (or atoms) within the unit cell must be determined.

PXRD methods are more commonly used in structure refinement than in full structure determination. Here, the unit cell parameters and the space group have been successfully determined. However, the attempts to determine the atomic/molecular positions have so far been unsuccessful. Since the structure is not fully known, refinement cannot be completed. Some of the problems that have hindered this include having an imperfect (although fairly good quality) powder, the presence of impurities in the XRD pattern (ruby, water, gasket reflections), the uneven background (which may cause misleading diffracted intensities in the low angle range) and phase mixtures.

4.4.5 Raman/Visual Evidence

The T_1 compound possesses a characteristic micro-texture that allows for visual recognition of the phase immediately after loading (Fig. 4.28). This texture remains after the pressure is changed within the phase stability region upon decompression. The first solid region generally appears uniform and smooth, making the transition evident from visual observation.

Figure 4.28: A photograph of a 58% mixture at 7.0 GPa possessing the characteristic texture observed upon loading. The compression chamber is approximately 120 μm.

In addition to the physical appearance, the Raman spectrum can also offer insight on the transition into the T_1 compound. In pure nitrogen, the transition from the β phase to δ phase is marked by the appearance of the ν_1 (N-N) mode in addition to the ν_2 mode, signifying the two types of disorder associated with the δ-N_2 structure [Bini, 2000] (see Fig. 2.9). The slope of the wavenumber of these modes over pressure experiences a small change upon entering the δ_{loc} phase (see Fig. 2.11). For pure methane, the ν_1 (C-H) mode experiences a change in slope over the I to A transition, then a splitting occurs to introduce a shoulder on the low wavenumber side during the A to B transition. The ν_3 mode changes in a similar way for both transitions, though in the B phase it splits into three modes. This mode is weaker and broader than the ν_1 mode and so the additional splittings are not shown or discussed (they are not sufficiently observed) (summarized in Fig. 2.24).

For mixtures between 50% and 60%, the system adopts the I* phase after freezing and then proceeds into the T_1 compound. Prior to this transition, the Raman spectrum of the mixture appears similar to that of the pure species (although the frequencies are somewhat shifted). The vibrational modes of molecules are affected by their environment, so in a mixture, shifts in the frequency of vibrational modes from the pure species would not be surprising.

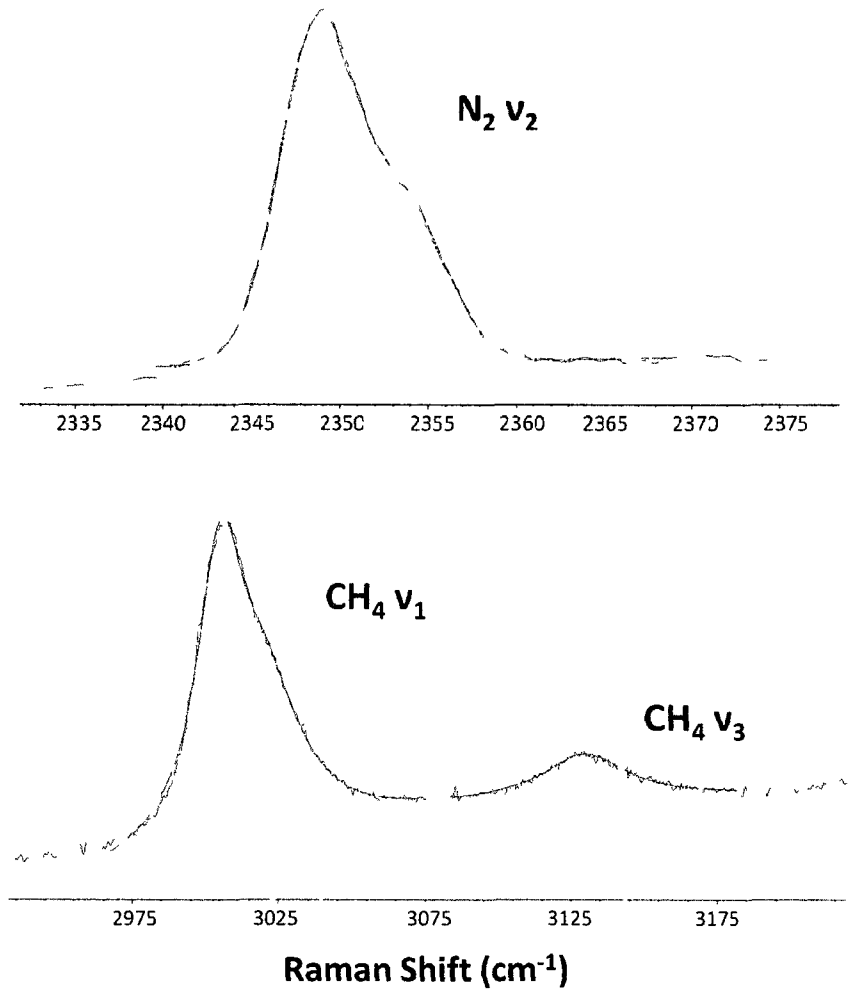

Figure 4.29: A portion of the Raman spectra of (top) nitrogen and (bottom) methane from a 54% sample at 9.42 GPa. Note: the nitrogen mode is fairly sharp so the scale is expanded to display the shoulder.

Shifts of a few wavenumbers (< 10 cm^{-1}) are observed for the v_2 mode of nitrogen and the v_1 mode of methane after the transition into the T_1 phase as well as before. The most interesting difference between the Raman spectra of the pure species and the T_1 spectrum is in the way the modes split. The v_2 mode of nitrogen appears to develop a shoulder on the high wavenumber side. This either represents that the v_1 mode is shifted by about 10 cm^{1} at 9.0 GPa (compared to a 54% mixture), or it is a result of the v_2 mode splitting. Moreover, the v_1 mode of methane splits at the transition into T_1 on the high wavenumber side, unlike in pure methane in which the shoulder appears on the lower wavenumber side of the v_1 mode at higher pressures (at 8 GPa instead of at 5

GPa, where the transition into T_1 occurs). The observation of a spectrum that differs from the pure species is consistent with the pXRD results and confirms the existence of a novel compound.

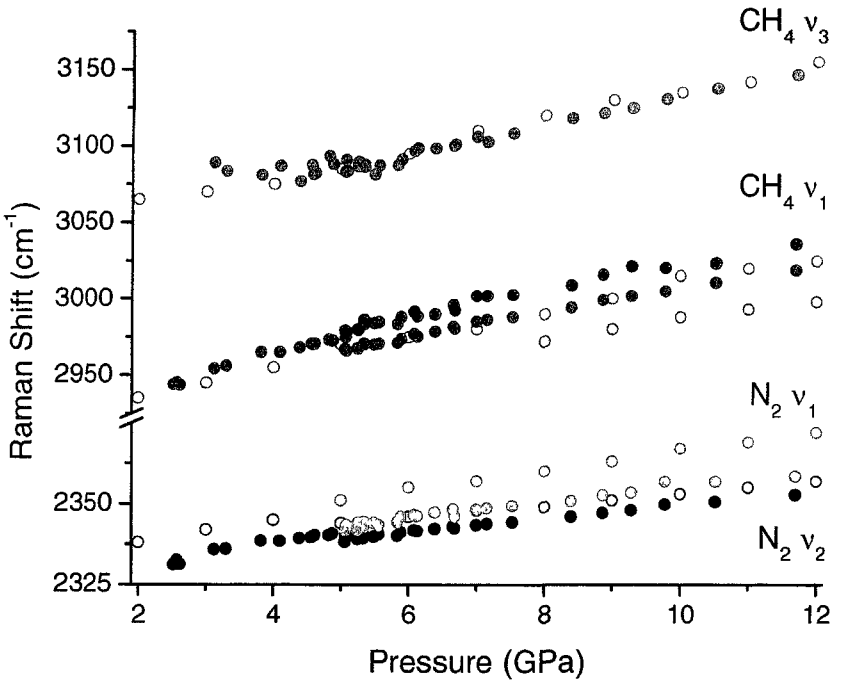

Figure 4.30: The wavenumber (Raman Shift) of Raman modes for nitrogen and methane molecules within the T_1 compound (full symbols) compared to those of the pure species (hollow symbols) [Scheerboom, 1996] and [Hebert, 1987].

4.5 A Second Novel van der Waals Compound: The MR Compound

In addition to the T_1 compound, another phase is identified in which the XRD pattern differs significantly from that of the pure species. The number of reflections alone is sufficient to dismiss the possibility of any combination of the pure phases. This phase exhibits a multitude of XRD lines, for which indexing is challenging. The name given to this phase was the MR phase (methane-rich phase). This phase is seen to exist in mixtures ranging from 10% to 50%.

The unit cell of the MR phase is discussed and the best candidates are presented. However, the amount of overlapping reflections makes it difficult to judge the number and position of peaks that are actually present. This inhibits the success of indexing as well as the determination of space group and stoichiometry. This phase is subject to a large degree of preferred orientation, so the relative pXRD intensities are not dependable.

4.5.1 Unit Cell

Prior to indexing, it is necessary to identify whether a single phase exists or not. Between a concentration of 40% and 49%, this novel compound exists with the T_1 compound. As the combination of these compounds produce an XRD pattern that includes a significant number of reflections, indexing the MR compound for these mixtures is not ideal. In a mixture of 36%, the T_1 compound is not indexed successfully within the observed pattern. It appears as though this may represent a region in which the MR compound exists as a single phase. Lower in concentration (25%), a similar pattern is observed, however, with the addition of new reflections. It is possible that these new reflections are now observed because of reduced preferred orientation (a better powder) or that they belong to another phase. The reflections observed in the 25% sample but not in the 36% sample were not successfully indexed, mostly due to the fact that they are weak reflections that are partially obscured by overlapping peaks in from the MR compound. Although it

cannot be ascertained, the following discussion assumes that the 36% mixture contains the MR compound as a single phase. This is indexed using the best candidate found for the MR compound.

This phase is clearly a low symmetry phase, likely representing a relatively large unit cell, based on the number of reflections that are overlapping and the reflections recorded at lower angles. Using the Crysfire suite, possible unit cells were proposed. Of these, not much confidence was put into large triclinic or monoclinic solutions since they included so many reflections that any matches to the observed pattern could be simply coincidental. The favoured solution was an orthorhombic unit cell: although large, this solution accounted for all observed reflections without significant excess in the lower angle range relative to the other solutions. This unit cell was also consistent over different pressures and in different mixtures.

For a 36% mixture at 9.0 GPa, the XRD pattern was indexed to an orthorhombic unit cell with lattice parameters a = 12.218 Å, b = 19.055 Å, and c = 5.794 Å. Since no structure can be proposed with the current data, a Le Bail fit was performed to judge whether or not these parameters are reasonable. The result is shown in Fig. 4.31. This represents the best candidate, although it is difficult to make any conclusions since it is not confirmed with confidence that this compound is observed as a single phase. Undoubtedly, if a phase mixture were present it would affect the quality and result of the fit.

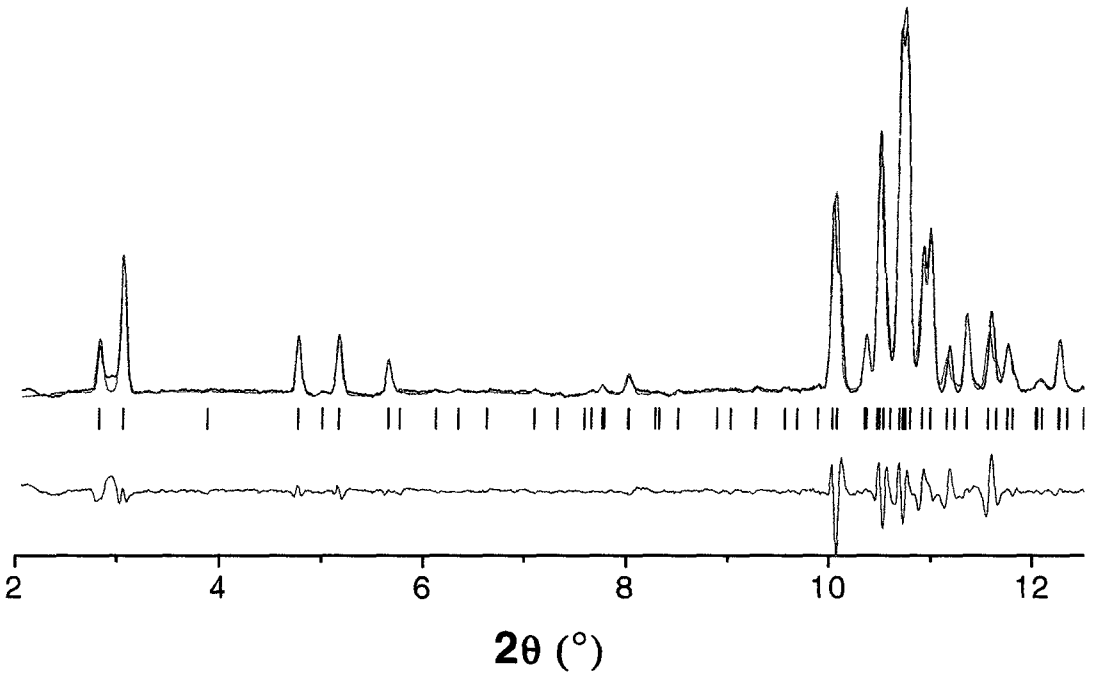

Figure 4.31: Le Bail fit to the XRD pattern recorded from a 36% mixture at 9.00 GPa. This calculated pattern represents the fit of the best candidate of the MR compound.

4.5.2 Stoichiometry and Equation of State

Since it cannot be verified conclusively whether the MR compound exists as a single phase in the 25% and 36% mixtures, the stoichiometry can only be narrowed down to between 25% and 35%. Thus, the stoichiometry is suggested as $(N_2)_3(CH_4)_7$.

The volumes of the MR compound for the 36% mixture and that of the 49% mixture are similar. With the weighted molecular volume assuming 30% nitrogen content, the number of molecules in this compound should be about 48. However, higher packing efficiency could exist. Fig. 4.32 shows the molecular volume of the MR compound for 47 to 50 molecules compared to the pure species.

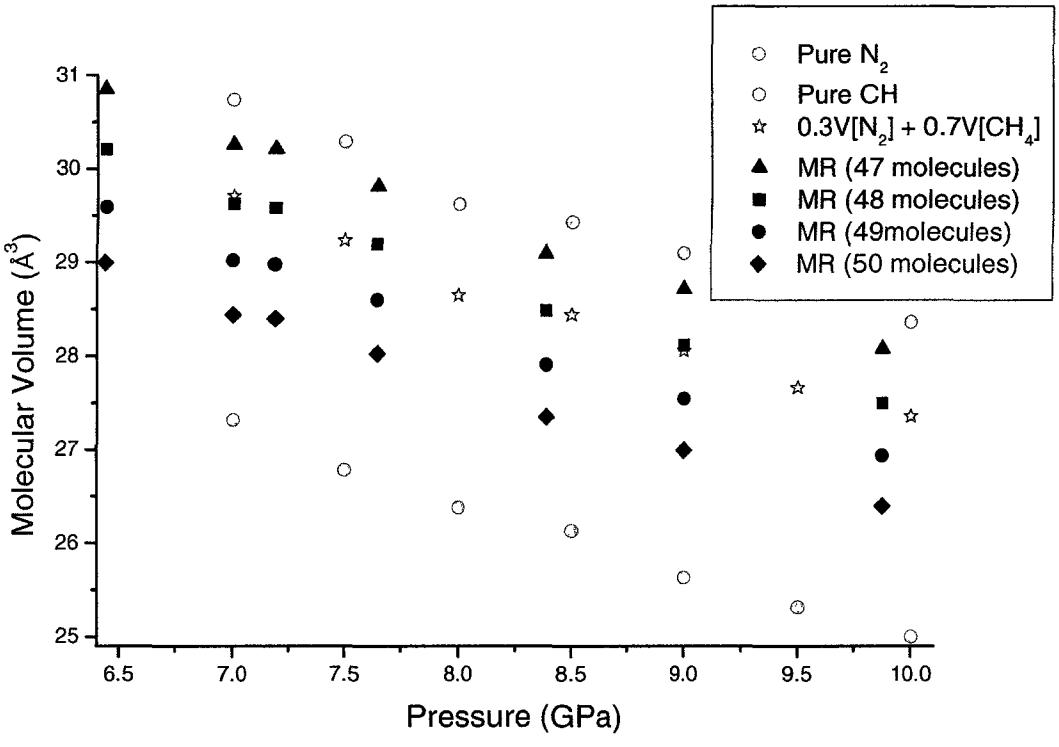

Figure 4.32: The equations of state for pure nitrogen [Olijnyk, 1990], pure methane [Nakahata, 1999] and the MR compound in a 36% mixture assuming 47, 48, 49, and 50 molecules. The star symbols represent the weighted molecular volumes assuming 30% nitrogen.

4.5.3 Space Group

There are many possible space groups for the MR compound, given the large orthorhombic unit cell. There are 23 space groups within the orthorhombic Bravais system that provide a relatively good fit to the observed reflections. This means that they account for all peaks, with less emphasis placed on reflections that are overlapping (exact positions are difficult to confirm when this occurs).

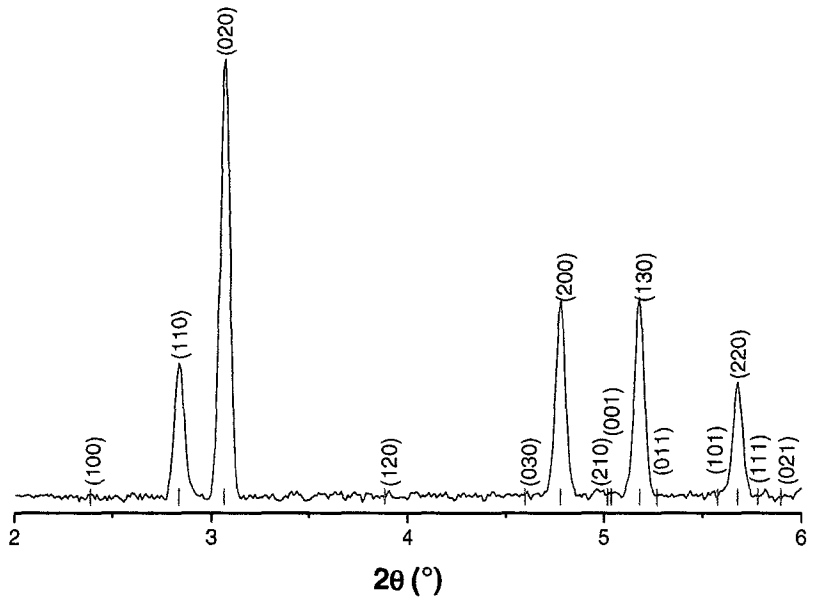

Figure 4.33: The low angle reflections from the MR compound in a 36% mixture at 9.00 GPa. The peaks are observed consistently in separate samples. There has been no evidence observed suggesting the existence of the absent reflections. However, the reflections that are predicted to appear close to an observed peak are difficult to rule out, as they may be superimposed.

The low angle reflections are the most important in narrowing down the space group as well as the unit cell. There are 5 reflections below 6° that are observed for all mixtures: a pair of reflections close to 3° and a set of 3 between 4.5° and 6°, as shown in Fig. 4.33. The number of possible space groups are narrowed down to those that do not predict the (100), (120) and (030) reflections. Out of the 23 possible space groups, 15 of them predict these absences. This is summarized in Table 4.5.

Table 4.5: Space Group Candidates for MR Compound

Space Group	(100) Absent	(120) Absent	(030) Absent
P222			
$P222_1$			
$P2_12_12$	✓		✓
$P2_12_12_1$	✓		✓
$C222_1$	✓	✓	✓
C222	✓	✓	✓
I222	✓	✓	✓
$I2_12_12_1$	✓	✓	✓
Pmm2			
$Pmc2_1$			
Pcc2			
Pmn2	✓		
$Pca2_1$	✓		
Pnc2			✓
$Pmn2_1$	✓		
Pba2	✓		✓
$Pna2_1$	✓	✓	✓
Pnn2	✓	✓	✓
Cmm2	✓	✓	✓
Imm2	✓	✓	✓
Iba2	✓	✓	✓
Pmmm			
Pnnn	✓	✓	✓
Pccm			
Pban	✓	✓	✓
Pbam	✓		✓
Pccn	✓	✓	✓
Pbcm			✓
Pnnm	✓		✓
Pmmn	✓	✓	✓
Pbcn	✓	✓	✓
Immm	✓	✓	✓
Ibam	✓	✓	✓

Table 4.5: A list of possible orthorhombic space groups that match the observed reflections of the MR compound. Candidates that predict observed absences are favoured. The space groups in bold represent the best candidates, as predicted by Chekcell.

The body-centered and base-centered space groups (those beginning with I and C, respectively) represent higher symmetry space groups than the primitive space groups. These are favoured, although the primitive space groups cannot be ruled out. Chekcell calculates the best candidates to be Iba2 and Ibam, both body-centered space groups. Without a proposed structure this cannot be confirmed.

5. Discussion

5.0 Introduction

The results of this work are summarized in the phase diagram presented in Fig. 4.1a. This complex map of phase regions contains several phases and the frequent occurrence of phase mixtures. Analysis of each observed phase was presented in sections 4.2 to 4.5 as well as some comments on the phase mixtures. A general discussion of these results and features of the phase diagram are presented in the following sections. In particular, the intriguing and complex methane-rich (< 50%) portion of the phase diagram is discussed in section 5.1.

As this work contributes to the overall goal of understanding binary mixtures and the formation of vdW compounds, the results for the nitrogen-methane binary system are compared to those of other systems in section 5.2. Section 5.3 provides a discussion on the validity of the proposed phase diagram for nitrogen-methane mixtures.

5.1 The Methane-Rich Portion of the Phase Diagram

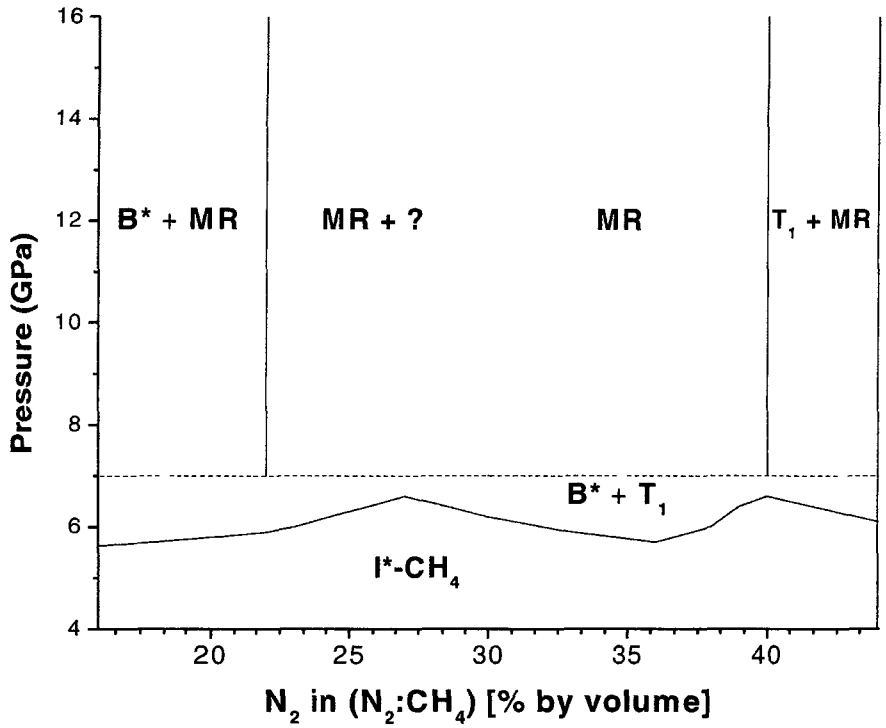

Figure 5.1: An expanded view of the methane-rich portion of the phase diagram

Mixtures in the methane-rich portion of the phase diagram (below 40%) exhibit complex behaviour. The dashed line outlining the stability of the B* + T_1 phase region is not well defined due to hysteresis associated with the transition in and out of this phase mixture. The dotted line separating the MR and MR + ? phase regions indicates that small differences in the XRD pattern of mixtures in each area make it difficult to judge whether or not the MR compound remains as a single phase in the pressure range studied at room temperature. This is elucidated in the following sections.

5.1.1 Phase Mixture of Two Novel van der Waals Compounds

For a 49% mixture, both the T_1 and MR compounds are observed above 7 GPa. Fig. 5.2 shows the XRD patterns of T_1 and MR plotted together for comparison. The combination of the XRD patterns of both compounds appears to reproduce the XRD pattern observed for this mixture. To demonstrate this, a slight offset was used to shift the top pattern along the 2θ axis. The difference in pressure causes a shift of the reflections, and although this is not linear with angle, applying the offset allows for easier visual comparison. It should also be noted that some of the reflections in multiplets are shifted closer together or further apart, which alters the shape of the pattern somewhat.

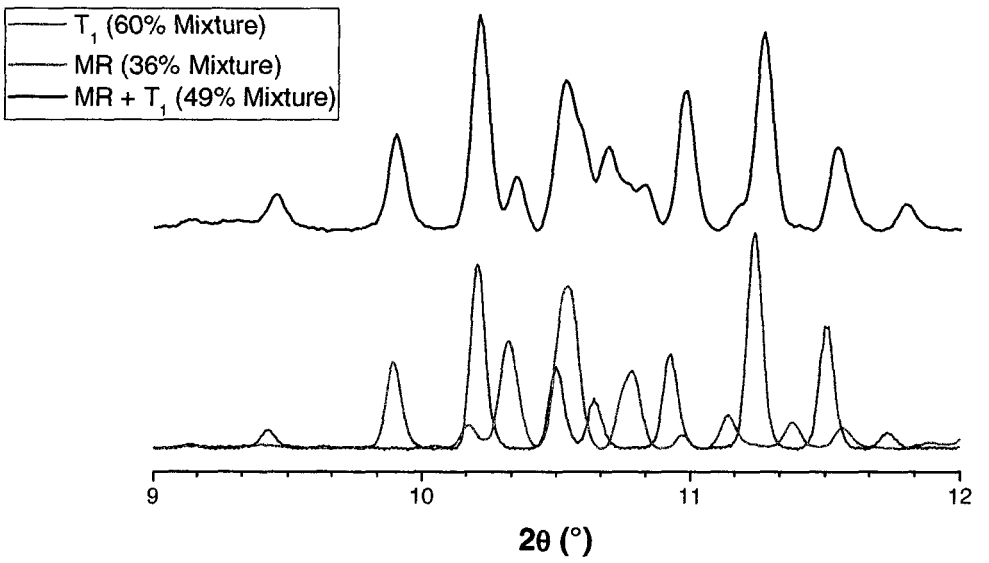

Figure 5.2: (Bottom) An overlay of the experimental XRD patterns of the T_1 and MR compounds from a 60% and 36% at 7.06 GPa and 7.00 GPa, respectively. (Top) Phase mixture containing both compounds in a 49% mixture at 8.02 GPa.

In order to produce the intensities of the observed XRD pattern for the 49% mixture, it is necessary to combine the XRD patterns of the compounds in a ratio of 0.75 MR to 1.0 T_1. By assuming the proposed stoichiometry of each compound, this would require a concentration of

47%, which is close to the calculated concentration. Of course, this assumes several factors: the stoichiometry is correct, preferred orientation does not significantly alter the relative intensities of either phase, and the intensity of one phase is directly related to its relative concentration in the mixture. However, this shows that the superposition of the XRD patterns from each compound yields the observed XRD pattern of the 49% mixture and that the proposed compound stoichiometry is reasonable.

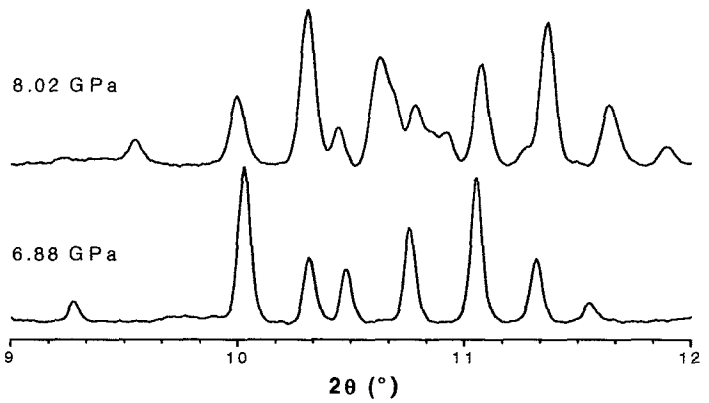

Figure 5.3: XRD patterns for the 49% mixture at 8.02 GPa and 6.88 GPa. Above 7 GPa, a combination of both compounds exist, but this mixture is not stable below this pressure.

It is intriguing to note that the two compounds possess similarities in the unit cell parameters. Around 9.7 GPa, the a and c parameters of MR are close to those of T_1, differing by less than 6%, though the b parameter of the MR compound is 1.7 and 3.2 times the a and c parameters of T_1, respectively. If the molecules were distributed in a similar fashion in both compounds, the MR compound could be described as an expansion (and increase in number of molecules) of the T_1 lattice. Unfortunately, the atomic positions are not known for either compound.

The transition from the phase mixture of the two compounds to the single T_1 phase is observed in the 49% mixture. This transition implies one of two conclusions: either the T_1 compound is not stable at concentrations as low as 49% above 7 GPa, or that the combination of the MR and T_1 compounds is lower in energy. In concentrations below 49% (i.e. in the 45% and 40% mixtures), the MR + T_1 region transforms into the B* + T_1 phases below 7 GPa. The T_1 compound is

thus no longer stable with a minority concentration of nitrogen (below 49%) and the excess methane conforms to the B* phase.

5.1.2 Other Phase Mixtures including the MR Compound

In the phase diagram (Fig. 4.1) and Fig. 5.1, above 7 GPa and between concentrations of 22% and 30%, the phase region is labelled "MR +?". This question mark refers to the fact that it is very difficult to tell whether or not the MR compound exists with a second component. In the 36% mixture, all reflections are indexed to the proposed unit cell of the MR compound. In a 25% mixture, however, additional reflections appear that cannot be well described by this unit cell and may belong to another phase.

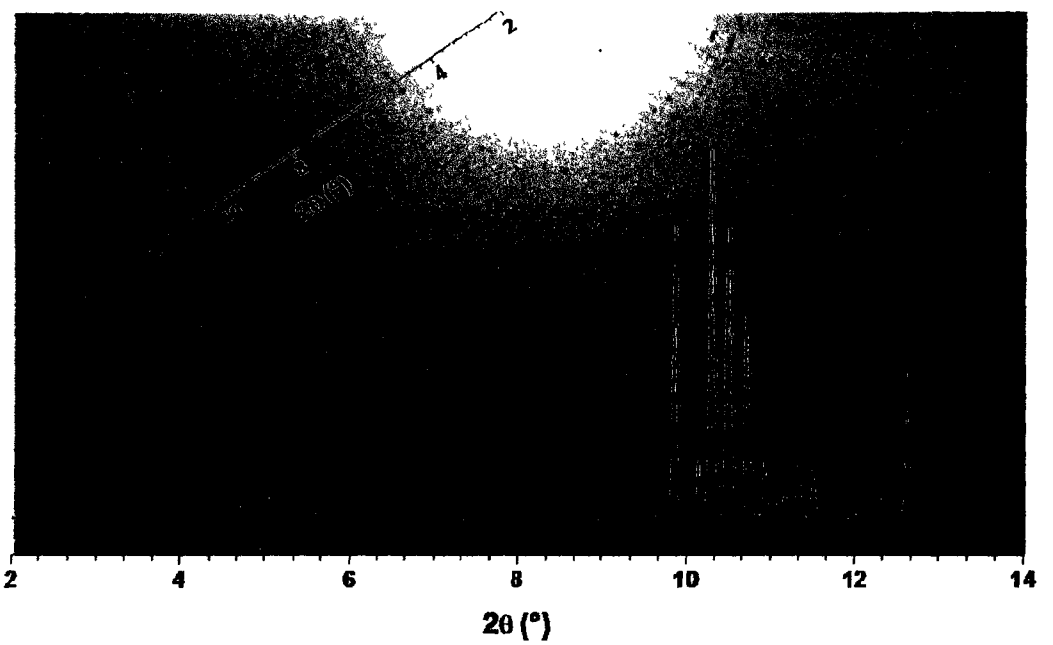

Figure 5.4: A portion of the XRD image of the MR compound from a 36% mixture at 6.75 GPa (below the normal stability pressure due to hysteresis) with the integrated background corrected XRD pattern overlaid. From the numerous spots, the sample appears to have many larger crystallites. The area in the top center represents where the beamstop blocks the scattering intensity and the smooth, broad line represents a reflection from the gasket material. An approximate 2θ scale is shown on the image.

The difference in the XRD patterns of the 25% mixture and the 36% mixture is that additional reflections may be present at the lower concentration. Low angle reflections around 5.4° and 9.6° appear for the 25% mixture at 8.92 GPa that are not included in the pattern of the 36% mixture (see Fig. 5.5). There are also reflections at 2θ values above these, however they are included in multiplets and cannot be well distinguished from the numerous reflections of the MR compound. For this reason, neither the existence nor identity of a second component is confirmed.

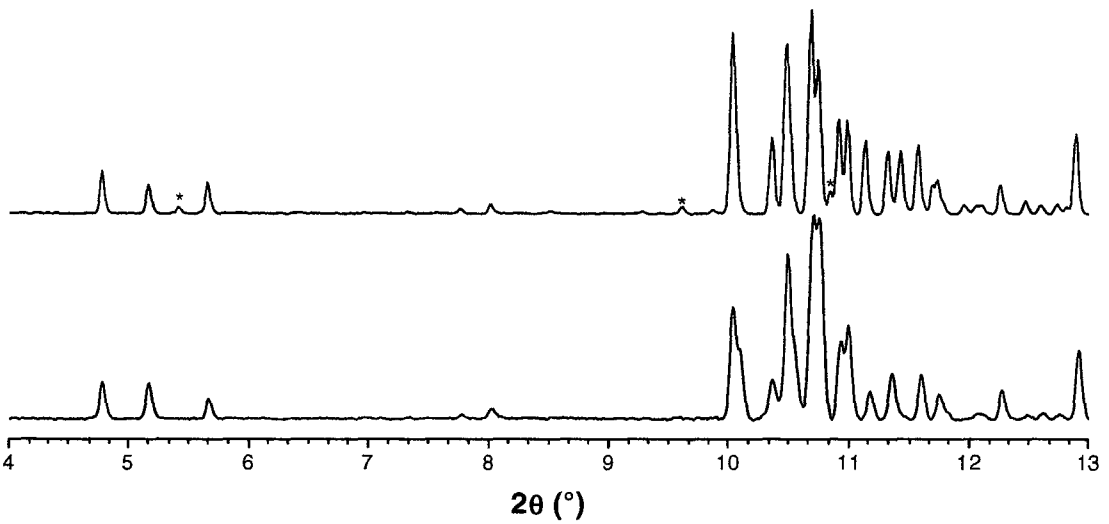

Figure 5.5: The XRD pattern from a (bottom) 36% mixture and a (top) 25% mixture with * to indicate the reflections that appear only in the 25% mixture. Both XRD patterns are taken around 9 GPa.

The existence of a second component is not confirmed due to the nature of the MR compound. It is possible that the proposed unit cell is incorrect or the lattice parameters are slightly off, and the true unit cell would account for the extra reflections observed in the 25% mixture. The transition into this phase is typically accompanied by the formation of large grains, and so not all crystal planes and orientations are accurately represented. The XRD image of the 36% mixture is comprised of many spots (Fig. 5.4). The 25% mixture consists of a better powder sample.

If a second component does exist, it is not the known A or B phases of methane or the δ or δ_{loc} phases of nitrogen. The occurrence of low angle reflections cannot be explained by these structures. The best fit was provided by the reflections of the T_1 compound, although with the

proposed stoichiometry this is not expected to be stable. It is possible that the T_1 compound is preent in regions in which the nitrogen concentration is slightly higher or exists as a very small portion of a phase mixture with the MR compound.

5.1.3 Hysteresis associated with the T_1 + B* Phase Region

For mixtures between 15% and just below 50%, a phase mixture of T_1 + B* results below 7 GPa. This is represented on the phase diagram (see Fig. 4.1) as a dashed line since the transition is observed anywhere between 6 and 10 GPa due to kinematics (ie how quickly the pressure is changed between measurements at a constant temperature). This is similar to the A to B transition in pure methane. The transition pressure is narrowed down based on complementary Raman spectroscopy studies that were performed over a long period of time, taking several spectra after each change in pressure. The transition is marked by the splitting of the v_1 mode of methane, shown in Fig. 5.6.

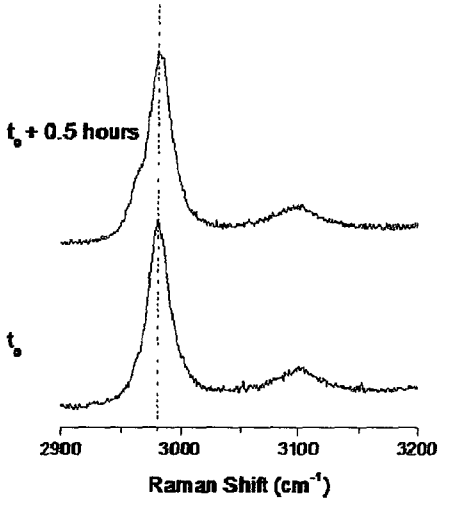

Figure 5.6: The bottom represents the Raman spectrum of methane immediately after pressure is changed from 7.446 GPa to 6.558 GPa and the top represents the Raman spectrum acquired after 0.5 hours. This is similar to what is observed in pure methane during the slow B to A transition.

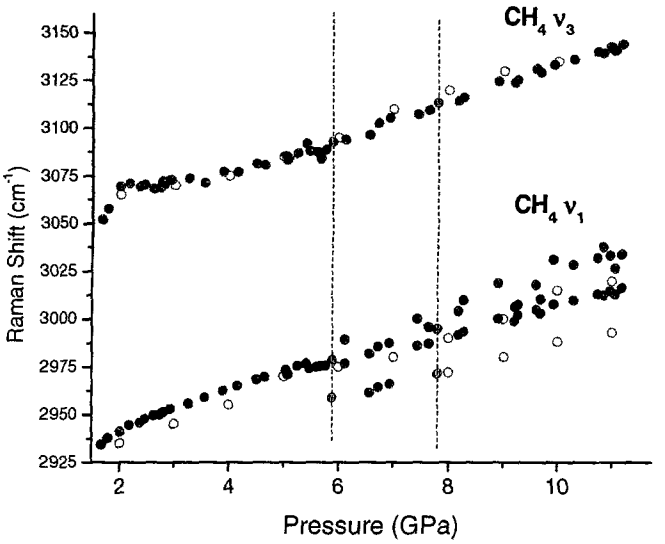

Figure 5.7: The plotted frequencies of the CH_4 Raman active stretching modes. The region affected by hysteresis is represented by the dashed lines. The ν_1 mode is observed for all pressures. The shoulder appearing on the low wavenumber side (red) corresponds to the B phase, and XRD images show that the B* + T_1 phase mixtures occurs in this pressure range. This phase mixture can reach higher pressures when the sample is not given sufficient time to equilibrate after pressure changes. The shoulder appearing on the high wavenumber side corresponds to the MR compound (green). The hollow symbols represent the vibration of pure methane [Hebert, 1987].

Only a limited amount of time is allowed for XRD experiments, so this time dependent transition had only been observed in our laboratory through Raman spectroscopy and visual measurements. The 40% mixture was loaded to 11.2 GPa, in which the two compounds are observed together. After going down in pressure to the I* phase, re-compressing the samples causes the T_1 + B* phase mixture to form, and this phase persists up to 13 GPa. A similar result occurs with the 25% mixture. Both of these mixtures have been subjected to successive pressure changes and later studied with Raman spectroscopy, during which the time-dependent transition is revealed.

5.2 Comparison to other Binary Systems

At high pressures, the N_2-CH_4 binary system exhibits a surprisingly complex phase diagram, as presented in this work (Fig. 4.1). It is interesting to compare some of the features of the phase diagram to those of analogous binary systems. Observing any trends, particularly in terms of compound formation, assists in understanding simple mixtures at high density and allow for better predictions of phase diagrams for mixed systems. The results of other binary systems including components comparable to nitrogen and methane should exhibit some comparable features to the phase diagram presented in this work.

5.2.1 The Argon-Nitrogen System

The methane molecule is analogous to the argon atom in terms of molecular size, its neutrality and effectively spherical geometry. Thus, one would expect the substitution of argon in nitrogen to be similar to that of methane. In the cubic δ-N_2 structure, argon atoms substitute preferentially in the a (spherelike symmetry) sites up to concentrations of 25% argon, in which all a sites are filled by argon atoms [Westeroff, 1996]. It is expected that methane molecules dissolved in this structure occupy the a sites as well (see Fig. 5.8a).

Unlike the nitrogen molecules on the a sites, those located on the d sites possess disklike symmetry, and are less similar in geometry to methane molecules. It cannot be determined whether methane molecules assume full occupancy of the a sites (replacing all or most the nitrogen molecules): at concentrations lower than 25% (implying full occupancy of the a sites) the T_1 compound is formed. Recall that an 88% mixture contains the T_1 compound in addition to the δ^* phase. Thus, the solubility of methane in the δ-N_2 structure is less than 12%, although this may not be representative of the true solubility limit.

Evidence of the preferred occupation of the argon atoms on the a sites of the δ-N_2 lattice is found in the Raman spectrum. The intensity ratio of the nitrogen vibrons in the pure state, v_2/v_1 is 3,

six are on the sites of spherelike symmetry (v_2) as the two molecules are on the sites of disklike symmetry (v_1) [Stinton, 1998] [Mulder 1998]. When the argon concentration is 25%, this ratio is increased to about 5 [Lotz, 2001]. This signifies that there are less nitrogen molecules occupying the a sites, since they are replaced by argon atoms.

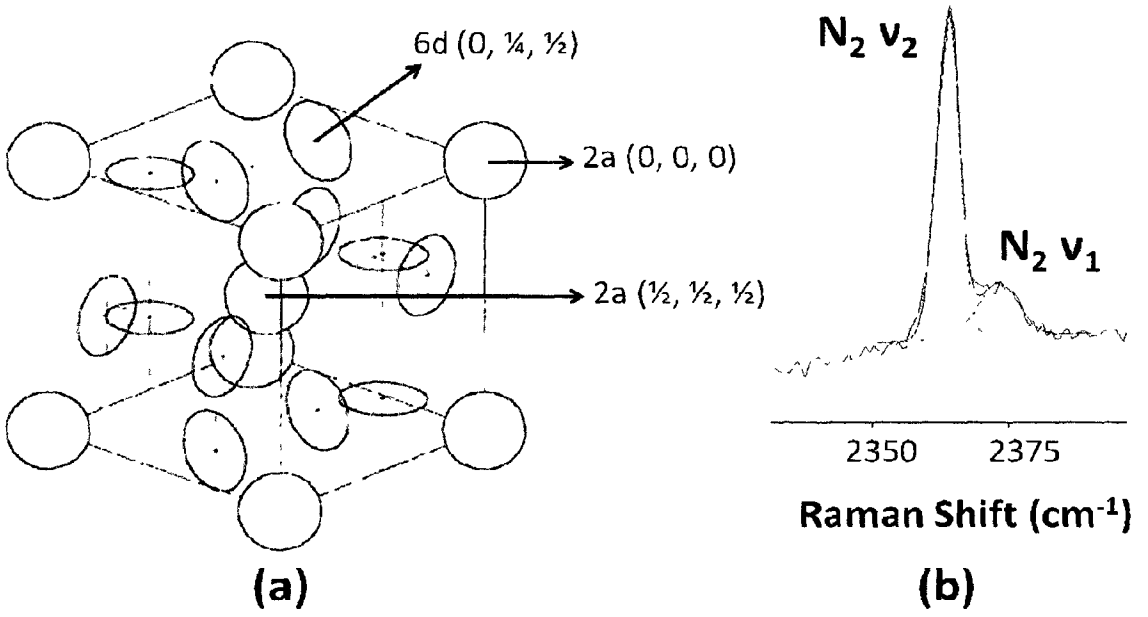

Figure 5.8: (a) The δ-N_2 structure is cubic with a sites exhibiting spherical symmetry (responsible for the v_1 mode) and the d sites exhibit disklike symmetry (responsible for the v_2 mode) [Mills, 1986]. The corresponding Raman spectrum (b) for the nitrogen molecules in an 88% mixture at 14.82 GPa show a increased intensity ratio (v_2/v_1) between the modes compared to pure nitrogen.

Although the observed intensity ratio (v_2/v_1) fluctuates with pressure, for the 88% mixture it is found to be about 4.5. In mixtures, the two vibrons (stretching modes) do appear closer together than in pure nitrogen, so the intensity of the v_2 could be increased by the superposition of part of the v_1 mode. Also, a phase mixture occurs with the T_1 compound, so the vibron intensity is not solely explained by the δ* phase. However, it does appear that the methane molecules preferentially assume the a sites. Although the nature of substitution of methane in δ-N_2 seems to be similar to that of argon, no vdW compounds have been reported in the argon-nitrogen binary system. Furthermore, phase separation of nitrogen and argon have been observed in the pressure range of interest [Aldous, 2010].

Methane molecules would likely show a higher solubility in the δ-N_2 structure if the T_1 compound did not form. However, the substitution of methane molecules causes the δ^* phase to increase in volume relative to the pure phase. The lower molecular volume of the T_1 (for either 31 or 32 molecules, see Fig. 5.9) phase stabilizes its formation, which appears to be more favourable than the expanded δ^* phase. This reduces the apparent solubility of methane in the δ-N_2 structure.

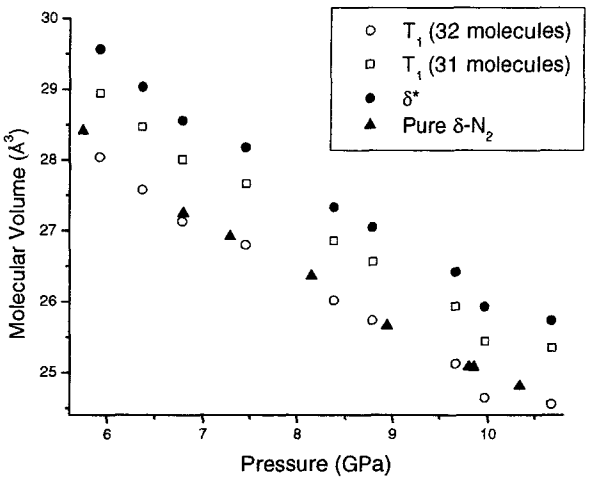

Figure 5.9: Molecular volume of the T_1 compound (as a 31 and 32 molecule structure) and the δ^* phase in the 88% mixture. The molecular volume of pure nitrogen [Olijnyk, 1990] is shown for comparison.

5.2.2 The Nitrogen-Oxygen System

The phase diagram of the nitrogen-oxygen system is quite different from that of nitrogen-methane, despite the similar molecular size ratio. In the nitrogen-methane system, the solubility of nitrogen in methane and vice versa are both quite high in the first solid phases and then similar for each component in the next solid phases. Conversely, in the nitrogen-oxygen system, nitrogen is hardly soluble in the oxygen solid phases, but oxygen exhibits an extremely high solubility in solid nitrogen. The δ phase of nitrogen actually spans a wide region of the phase diagram, extending to 90% oxygen concentration around 6 GPa. At pressures above this, a compound exists for a narrow

range of concentration and pressure, above which phase separation occurs. Nitrogen, on the other hand, has a solubility in solid oxygen of less than 5% above 5 GPa. This is similar to the solubilities of nitrogen in the A and B phases of methane, as well as methane in the δ phase of nitrogen.

The effect of methane on the lattice of δ nitrogen is comparable to the effect that oxygen has. A 10% concentration of oxygen causes a 3% expansion of the δ structure at 5 GPa [Sihachakr, 2004]. For less than 10% (as 12% methane causes the formation of T_1 in addition to the δ* phase) methane at the same pressure, the δ structure experiences a volume increase of around 3.5%.

5.2.3 Oxygen-Containing Systems vs. Nitrogen-Containing Systems

Molecular oxygen and nitrogen are similar in both size (there is a 0.94 size ratio) and geometry. Thus, one may expect a phase diagram of oxygen and a second component to be similar to that of nitrogen mixed with the same component mixed. Molecular oxygen does, however, possess a magnetic moment due to unpaired electrons, which could affect its interaction with another molecule. Potentially, the addition of the second component would reduce short and long range effects of this magnetic moment.

In the oxygen-xenon binary system, a stoichiometric compound, $Xe(O_2)_2$ forms at room temperature above 3 GPa and spans most of the phase diagram up to 10 GPa and above 15% oxygen (molar fraction) [Weck, 2010]. In the nitrogen-xenon system, a compound is observed in the phase diagram at 408 K and possible stoichiometries include $Xe(N_2)$ and $Xe(N_2)_2$ [Kooi, 1999]. The resulting phase diagrams of N_2-Xe and O_2-Xe are quite similar in shape. In fact, from 20% to 80% N_2/O_2, the phase regions are very close, shown in Fig. 5.10. Phase lines are somewhat shifted, which is expected since the nitrogen-xenon system is at higher temperature.

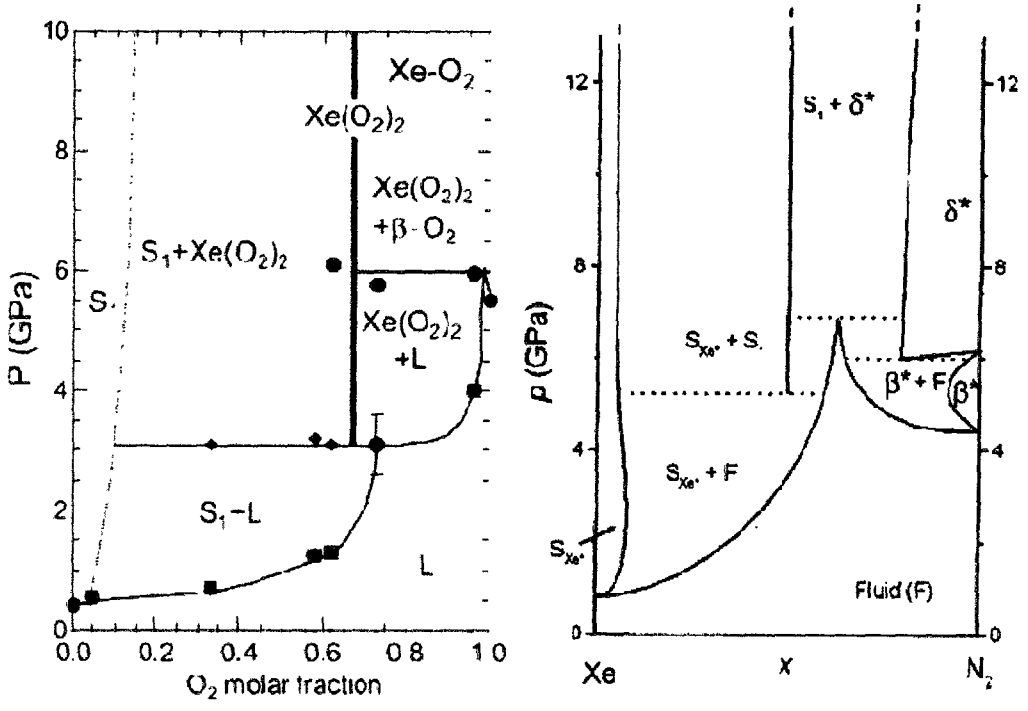

Figure 5.10: (Left) The O_2-Xe phase diagram at room temperature [Weck, 2010]. The S_1 phase refers to a solid rich in xenon (similar to S_{Xe^*} in the N_2-Xe phase diagram). (Right) The N_2-Xe phase diagram at 408 K [Kooi, 1999]. Although a higher temperature, the N_2-Xe phase diagram exhibits many similar phase regions. In both phase diagrams, the amount of xenon increases to the left.

Although the binary systems of nitrogen and oxygen with xenon are similar, mixtures of oxygen and neon show no compound formation at room temperature up to 12 GPa. In fact, above 7 GPa, phase separation occurs [Weck, 2010]. With nitrogen, neon forms two stoichiometric compounds within this thermodynamic range [Kooi, 1999]. It is interesting to note, however, that the phase diagrams below 7 GPa are very close. It is clear that many factors must be taken into consideration when attempting to find trends between binary systems.

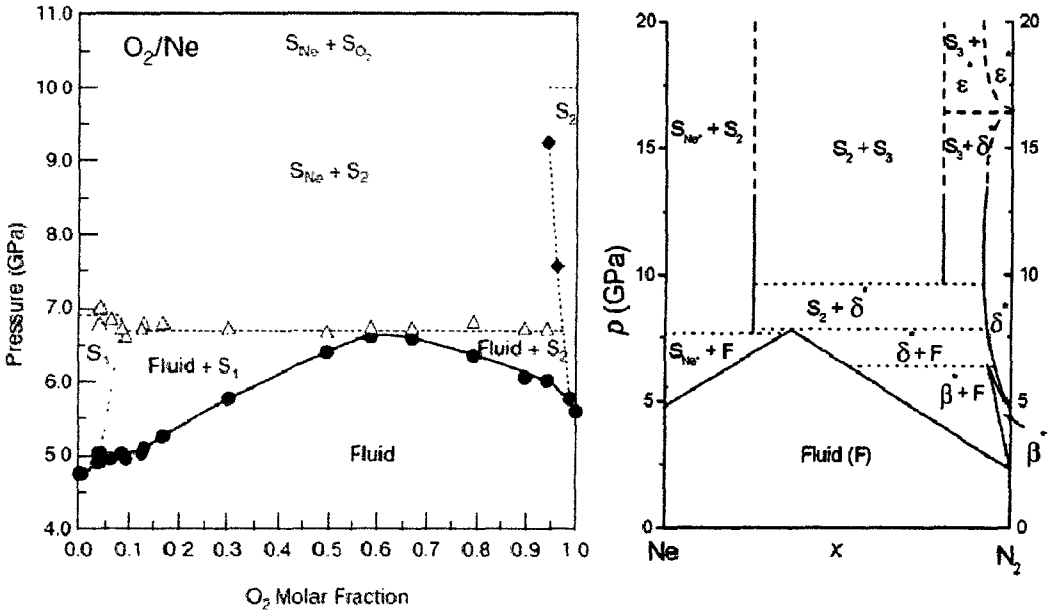

Figure 5.11: (Right) The O_2-Ne phase diagram at room temperature [Weck, 2010]. The S_1 phase refers to a solid rich in neon (similar to S_{Ne^*} in the N_2-Ne phase diagram) and S_2 is a solid rich with oxygen. (Right) The N_2-Ne phase diagram at room temperature. In this phase diagram, the S_2 and S_3 represent the compounds [Kooi, 1999].

As a preliminary attempt to draw the similarities to the nitrogen-methane system, a sample was loaded containing approximately equal concentrations of oxygen and methane in order to see if any comparable compounds formed in this system. Although mixtures of a noble gas and oxygen or nitrogen appear to show similar phase diagrams (at least in some pressure ranges), one should expect some parallel features between the nitrogen-methane and oxygen-methane systems. The oxygen-methane sample studied showed no compound formation, although contamination of nitrogen and ice occurred.

5.2.4 Methane-Containing Systems

Most binary systems previously studied involve a noble gas as at least one of the components. Methane, although sometimes described as a "bad rare gas model" [Bini, 1995], has been studied in few binary systems in the search of vdW compound formation. The methane-hydrogen binary system is particularly interesting since it includes the formation of four novel vdW compounds below 8 GPa.

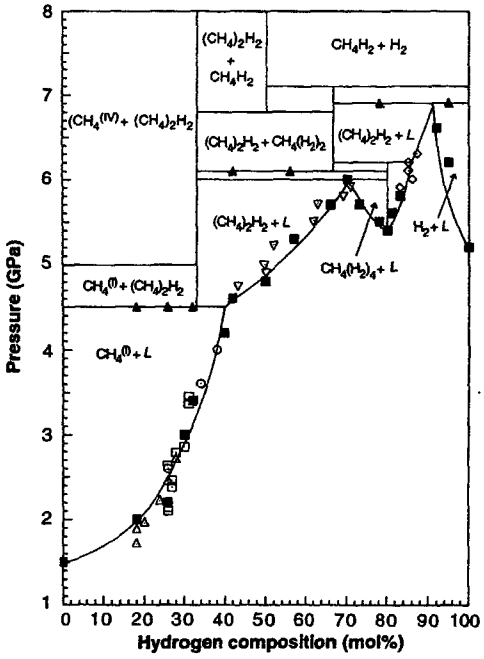

Figure 5.12: The methane-hydrogen binary phase diagram at room temperature [Somayazulu, 1996].

Another interesting feature about this binary system is the phase mixtures. There does not appear to be any regions in which a single phase exists. The compounds exist in a phase mixture with a second compound or with one of the pure phases of hydrogen or methane, as is seen in the nitrogen-methane system. The existence of such phase mixtures implies that there is not a significant difference in energy between the compounds, as is expected for weakly bound vdW compounds.

5.3 Accuracy of Phase Diagram and Sources of Error

The presented phase diagram (Fig. 4.1) represents a map of phases that were discovered when varying the pressure for each concentration. Perhaps referring to this as a *phase diagram* is misleading. In a phase diagram, one should be able to take any thermodynamic path to obtain a particular phase (or phase mixture), and only this phase should exist, regardless of the route taken. Thus, when the term phase diagram is used here, it is referring more accurately to a diagram or map of phases.

Making this distinction is inspired by the complexity of mixed systems studied under pressure. Kinematics play a role in this: increasing or decreasing the pressure on a sample quickly or slowly can alter a transition pressure or even cause a phase mixture including a metastable phase. Hysteresis, for example, is seen in the methane phase diagram between phases A and B, which is similar to what is observed with the T_1 + B* phase mixture. Letting the sample sit over a larger time period at a given temperature, the system could reach an equilibrium phase that is somehow different from the phases previously observed. Also, it is possible that an energy barrier restricts the sample from entering its proper equilibrium state; in this case, the addition of a small amount of energy could influence the state that the system assumes.

Additional influences arise from non-hydrostatic pressure conditions, particularly around grain boundaries, which often experience residual and excess stress. The grain size plays a role in this, which is partly determined by how the pressure is applied to the sample. Some phases also have a tendency to form larger grains, particularly those which contain a large amount of methane (MR, B*, A*).

The diagram of phases that does result is also subject to sources of error involved in the acquisition of data and calculation of results. Quantities such as transition pressures and unit cell volumes are fairly reproducible throughout different data sets and in different samples. The reliability of pressure measurements is very important in evaluating the quality of results.

As described in section 2.1.5, the pressure is measured using the ruby fluorescence technique in situ. Although the result is given to 0.1 to 0.01 GPa (a precision obtained as per the resolution of the spectrograph—at the CLS, the spectrograph resolution is lower than that used in

our laboratory), it is difficult to say whether or not this pressure truly represents the stress throughout the sample. The stress in the compression chamber may not be evenly distributed due to fissures or imperfections in a diamond anvil, misaligned components in the DAC, anisotropic distortion of the gasket, crystal grain boundaries and size or due to the relaxation of the DAC and sample.

Particularly with XRD experiments (as limited time is given at synchrotron radiation facilities), it is not practical to allow the sample to reach an equilibrium state over a long period of time. Thus, occasionally the pressure reading is still increasing or decreasing after compression or decompression of the sample when the XRD image is recorded. Over the duration of the image acquisition, which is often several minutes, the sample can experience a pressure change up to 0.4 GPa (but typically closer to 0.1 GPa). This can also allow hysteresis to occur, interfering with the acquisition of accurate results.

The associated error with these experimental limitations are minimized through proper sample and DAC preparation, performing multiple trials, allowing the sample as much time as possible to reach equilibrium and frequent pressure measurements. After compression or decompression, the pressure is monitored until it reaches a fairly consistent value before recording the XRD image, and then confirmed after the image is acquired.

6. Conclusions and Future Prospects

6.0 Introduction

The results obtained throughout this work on the solid phases of the nitrogen-methane binary system were presented in chapter 4 and related discussions were presented in chapter 5. The outcome of this work is summarized and remarks are made on the success towards reaching the objective in section 6.1. Additionally, future research prospects for this work are outlined in section 6.2. This thesis is concluded in section 6.3.

6.1 Summary of Results

The N_2-CH_4 system at room temperature and high pressure (up to 16 GPa) shows increased solubility when compared to the low temperature phase diagram. Phase diagrams by [Prokhvatilov, 1983] show a solid solution of I-CH_4 and β-N_2 to exist between 45% and 77%, whereas in this work the co-existence region was merely a narrow range around 60%.

The high solubility of these solid phases may be attributed to the spherical disorder in the nitrogen and methane molecules, in their respective structures. The molecules act like spheres, making their molecular size as well as their geometry similar. These similarities would allow substitution of one molecular species in the structure of the other without a significant effect. The methane solid appears to be the more stable structure with substitution, as it persists over a larger range of concentration. Substitution of methane in β-N_2 causes an unfavourable volume increase in the structure, whereas the I-CH_4 structure experiences higher packing (a volume decrease) with the substitution of the smaller nitrogen molecule, thus providing additional stability.

The next solid phase (higher in pressure) in methane is phase A. This phase is observed only in one methane-rich (10%) mixture and only for one pressure point. This phase does not appear to be stable with the substitution of nitrogen molecules, as it is not seen in any other area of the phase diagram. Instead, phase B is observed. The B-CH_4 and δ-N_2 phases can accommodate a much smaller amount of the other component compared to the first solid phases.

The δ-N_2 structure possesses two types of sites in which molecules exhibit a different type of spatial disorder. Two out of eight of these molecules possess spherical disorder. Methane molecules, being tetrahedral in shape may be considered essentially spherical, are not as favourably substituted in this structure since they are different in geometry than most of the molecules in the δ-N_2 structure. Thus, as low as 12% methane in nitrogen can influence the formation of the vdW compound, T_1, to accommodate a fraction of the methane. A similar amount of nitrogen in B-CH_4 also influences the structure to undergo a change in volume; a decrease in unit cell volume is observed. A substitution of 10% nitrogen in this structure causes a very minor amount of MR compound to form. The amount of nitrogen dissolved in B-CH_4 is less than 10%, but not by much.

Although no definite conclusions can be made regarding the fraction of the compounds relative to the pure phases in the phase mixture, it appears as though slightly more nitrogen can dissolve in B-CH_4 than methane in the δ-N_2 structure. This is not surprising, since the substitution of methane by nitrogen causes a relative volume reduction, which is more favourable than expansion for a system under high pressure.

However, it should be noted that the solubility estimates are based on the maximum amount of one component *observed* to substitute into the structure of the other component. Since compound formation results, this does not necessarily imply that the solubility limit is reached. Instead, this formation reveals that the combination of nitrogen and methane in the stoichiometry of the compound is more favourable than the substitution of one component in the structure of the other.

Two novel vdW compounds are observed to form within the pressure range studied: the methane-rich compound, MR, and the nitrogen-rich compound, T_1. Both of these compounds have unit cells that are surprisingly large compared to the unit cells characteristic of the pure species. To the best of the knowledge of the author, these large unit cell seem to be unique to the nitrogen-methane binary system.

The T_1 compound spans a wide range of concentration in the phase diagram. Along with the B* phase, it exists as low as 15%, as a single phase it exists from 49% up to 70%, and with the δ* phase it is observed as high as 88%. The tetragonal unit cell has approximately 32 molecules and the proposed stoichiometry is $(N_2)_3(CH_4)_2$. The best candidates for space groups include *$P4_2/mnm$*, *$P4_2nm$*, and *P-4n2*. Complementary Raman spectroscopy results reinforce the deviation of the T_1 compound from the structures of the pure species.

The MR compound, on the other hand, is not as well described as the T_1 compound due to its apparent lower symmetry and larger unit cell. The best candidate for its unit cell is an orthorhombic cell belonging to space groups *Iba2* and *Ibam*. The number of molecules is likely around 48 with a proposed stoichiometry of $(N_2)_3(CH_4)_7$. The transition between this compound and the lower pressure phase mixture of T_1 + B* is subject to a large hysteresis, although time-dependent Raman spectroscopy experiments confirmed the transition to take place around 7 GPa.

6.2 Future Prospects

A binary phase diagram system can always benefit from the study of additional concentrations and pressures. There exists an ever-present quest of extending the pressure limits of a phase diagram in hopes of describing the stability limits of the observed compounds, discovering other novel compounds, and examining the effect of substitution on pressure induced transitions.

6.2.1 Further Refinement of the Phase Diagram

Within the current phase diagram for the nitrogen-methane binary, unanswered questions remain and there is a need for refinement of the description of the mixed solids and novel compounds. Systematic study of several concentrations within a phase region provides insight on how and where the molecules substitute in the compounds or structure of the pure species. Although the scattering powers of nitrogen and carbon are similar given their atomic numbers, relative XRD intensities from a given phase should experience changes when the concentration of one component with respect to the other is increased within the solid.

Neutron diffraction, combined with X-ray diffraction experiments, as performed in our work, is a powerful technique that can reveal a solid structure. Neutron diffraction experiments would effect the relative intensities of reflections since the neutron scattering cross sections of nitrogen and methane are more distinguishable. More importantly, the contribution of hydrogen in neutron diffraction experiments is much stronger than in XRD experiments. Preferential substitution should also be detectable through Raman spectroscopy, although higher resolution is necessary to discriminate the intensity of the modes from their shoulders.

The systematic study within a phase region would also reveal the change in the relative amounts of the phases in a phase mixture. For the phase mixture of MR + T_1, observing the intensities of the reflections of one compound with respect to the other would allow for the fine-tuning of the stoichiometry. This could also be done for the B* + MR and δ* + T_1 phase mixtures.

6.2.2 Improvement of Concentration Determination Techniques

In order to conduct systematic studies within a phase region, the concentration determination method would require improvement. A high pressure gas loading apparatus for samples within a DAC is currently under construction. By measuring partial pressures of gases within the gas loading apparatus, a more accurate initial concentration is determined prior to loading, compared to measuring the relative volumes within a liquid mixture. With mixtures of well-known concentration, the relative intensity of Raman modes could be measured to refine the current relationship.

Other methods of concentration determination have also been proposed. Calibrating the boiling temperature of the liquid mixture to concentration would be more reliable than measuring the volumes. The boiling temperature would fluctuate however, as the liquid methane and liquid nitrogen would boil unevenly from the mixture. Measuring the relative abundance of molecular species of a sample with mass spectrometry is another possible avenue to determine the concentration.

6.2.3 Structure Determination

An important future goal for describing the nitrogen-methane binary system is to determine the structures of the novel vdW compounds. Before this can be attempted for the MR compound, the unit cell must be confirmed. In order to do this, more information is required for the XRD pattern at low angles. The replacement of the beamstop by a smaller lead plug was attempted, although the acquisition of an XRD image of the MR compound was unsuccessful. This would reveal if any reflections exist below the first observed reflection at 2.8°. These reflections are vital in determining the space group and unit cell.

The phase region in which the MR compound exists also requires more attention. It is crucial to determine whether or not a second component exists in order to confirm the proposed unit cell of the MR compound. The production of a better quality powder is also desirable.

Annealing the sample may improve the quality of the powder; however this may also inspire the formation of larger grains or a single crystal.

Single crystal diffraction would provide more insight into the structure for both compounds. The growth of a single crystal was attempted several times for the T_1 crystal without success. Heating the sample was not attempted, and may provide a path to single crystal growth.

Another way to gain information on the structures of the compounds is to observe the vibrational modes of the lattice. The Raman-active lattice modes appear at very low wavenumbers, close to the excitation wavelength. For pure nitrogen and methane in the relevant pressure range (< 16 GPa) these modes are extremely broad and weak [Schneider, 1992] [Medina, 1979]. Attempts were made, however there was no success in viewing these lattice modes with the employed spectrograph. Determining the total number of vibrational modes (lattice modes, vibrons, and IR-active modes) may allow the elimination of proposed space groups and information regarding the occupied sites of the molecules.

Neutron diffraction patterns would complement the acquired XRD patterns in structure determination, as both patterns can be refined simultaneously using structure refinement programs. Neutron diffraction would also provide the contribution of hydrogen atoms, which is difficult to resolve with XRD experiments since hydrogen has such a low atomic number.

6.2.4 Extension of the Phase Diagram

The room temperature nitrogen-methane binary phase diagram is unknown above 16 GPa. The stability limits of the T_1 and MR compounds have yet to be discovered, as well as the possibility of additional novel compounds of nitrogen and methane.

Attempts to achieve higher pressures include reduction of the diameter of the compression chamber and implementation of a rhenium gasket. A smaller sample is disadvantageous since it contains less volume to scatter from, reducing the intensity of XRD patterns and the Raman spectra. However, it also reduces the possibility of losing the sample upon compression. If the sample space

expands or translates, there is not as much danger of it finding its way outside the diamond culets than if the sample space was larger. The use of a stronger metal for the gasket material also reduces the distortion and translation of the compression chamber. Unfortunately, these attempts were unsuccessful due to the poor quality of the rhenium metal used.

6.3 Concluding Remarks

As vdW compounds have previously been discovered in binary systems such as N_2-He [Vos, 1992], CH_4-H_2 [Somayzulu, 1996] and N_2-O_2 [Sihcahkr, 2004], this thesis describes two novel molecular compounds that have been discovered in the N_2-CH_4 binary system below 16 GPa at 300 K. The previously undiscovered phase diagram of this system at room temperature is presented in Fig. 4.1, which displays a rich polymorphism and collection of phase mixtures.

Over 20 samples have been studied over pressures up to 16 GPa and with concentration varying from 10% to 90% nitrogen in nitrogen-methane mixtures by volume. Through XRD, phases have been identified and defined, with Raman spectroscopy results providing complementary information and the refinement of phase lines. In chapter 4, the numerous phases and phase regions are discussed, and these results are summarized in section 6.1.

A unit cell and space group candidates have been proposed for the T_1 and MR compounds, as well as suggested stoichiometry and stability range. Despite the amount of data collected, full structure solution was not successfully completed. This emphasizes the complexity of these novel compounds, as well as the richness of the nitrogen-methane binary system.

References

Anderson, A., The Raman Effect (Vol. 2), Marcel Dekker Inc, New York (1973)

Anderson, A., The Raman Effect (Vol. 1), Marcel Dekker Inc, New York (1971)

Angel, R.J., Allan, D.R., Miletich, R., Finger, L.W., The Use of Quartz as an Internal Pressure Standard in High-Pressure Crystallography, J. Appl. Cryst., 30, 461 (1997)

Barat, J.L., Vos, W.L., Stability of van der Waals compounds and investigation of the intermolecular potential in helium-xenon mixtures, J. Chem. Phys., 97 (8) 5707 (1992)

Bassett, W.A., Diamond Anvil Cell, 50th Birthday, High Pressure Research, 29 (2) 163 (2009)

Bini, R., Jordan, M., Ulivi, L., Jodl, H.J., Infrared and Raman Studies on High Pressure Phases of Solid N_2: An Intermediate Structural Modification between epsilon and delta Phases, J. Chem. Phys., 108 (16) 6849 (1998)

Bini, R., Pratesi, G., High-Pressure Infrared Study of Solid Methane: Phase Diagram up to 30 GPa, Phys. Rev. B, 55 (22), 14800 (1997)

Bini, R., Ulivi, L., Jodl, H.J., Salvi, P.R., High pressure crystal phases of solid CH_4 probed by fourier transform infrared spectroscopy, J. Chem. Phys., 103 (4) 1353 (1995)

Bini, R., Ulivi, L., Kreutz, J., Jodl, H.J., High-pressure phases of solid nitrogen by Raman and infrared spectroscopy, J. Chem. Phys.,112 (19), 8522 (2000)

Buchsbaum, S., Mills, R.L., Schiferl, D., Phase Diagram of N_2 determined by Raman Spectroscopy from 15 to 300 K at Pressure up to 52 GPa, J. Phys. Chem, 88, 2522 (1984)

Callister, W.D., Materials Science and Engineering: An Introduction (4th Ed.), John Wiley & Sons, USA (1997)

Chen, J., Jin, L., Dong, J., Zheng, H., In Situ Raman Spectroscopy Study on Dissociation of Methane at High Temperatures and High Pressures, Chin. Phys. Lett., 25 (2) 780 (2008)

Canadian Light Source: www.lightsource.ca

Colwell, J.H., Gill, E.K., Morrison, J.A., Second Transition in Solid CH_4, J. Chem. Phys., 36 (8), 2233 (1962)

Connolley, D., Milbrodt, T., Stoner, R., Preliminary solid-solid phase diagram for nitrogen-methane mixtures by x-ray diffraction, J. Chem. Phys., 73 (10) 5388 (1980)

Cromer, D.T., Mills, R.L., Schiferl, D., Schwalbe, L.A., The Structure of N_2 at 49 kbar and 299 K, Acta. Cryst., B37, pp. 8 – 11 (1981)

Cullity, B.D., Stock, S.R., Elements of X-Ray Diffraction (3rd Ed.), Prentice Hall, New Jersey (2001)

Desgreniers, S., Vohra, Y.K., Optical-response of very high-density solid oxygen to 132 GPa, J. Chem. Phys., 94, 1117 (1990)

El Kader, M.S.A., On high pressure phase transitions in solid methane, Chem. Phys., 277, 77 (2002)

El-Sheikh, S.M., A phase transition for solid methane, Chem. Phys. Lett., 247, 159 (1995)

Eremets, M.I., Gavriliuk, A.G., Trojan, I.A., Dzivenko, D.A., Boehler, R., Single-bonded cubic form of nitrogen, Nature, 3, 558 (2004)

Eremets,M.I., High Pressure Experimental Methods, Oxford University Press, New York/Tokyo (1996)

Fabre, D., Thiery, M.M., Kobashi, K., Raman spectra of solid CH_4 under high pressure. ii. new Phases below 9 kbar at 4.2K, J. Chem. Phys., 76 (10) 4817 (1982)

Fabre, D., Thiery, M.M., Vu, H., Kobashi, K., Raman spectra of solid CH_4 under pressure I. phase transition between phases II and III, J. Chem. Phys., 71 (7) 3081 (1979)

Ferraro, J. R., Nakamoto, K., Brown, C.W., Introductory Raman Spectroscopy (2nd Ed.), Academic Press (1994)

Gregoryanz, E., Goncharov, A.F., Hemley, R.J., Mao, H.K., Somayazulu, M., Shen, G., Raman, infrared, and x-ray evidence for new phases of nitrogen at high pressures and temperatures, Phys. Rev., 66, Art. No. 224108 (2002)

Gregoryanz, E., Goncharov, A.F., Sanloup, C., Somayazulu, M., Mao, H.K., Hemley, R.J., High P-T transformations of nitrogen to 170 GPa, J. Chem. Phys., 126, Art. No. 184505 (2007)

Gregoryanz, E., Sanloup, C., Bini, R., Kreutz, J., Jodl, H.J., Somayazulu, M., Mao, H.K., Hemley, R.J., On the epsilon-zeta transition of nitrogen, J. Chem. Phys., 124, Art. No. 116102 (2006)

Hammond, C., The Basics of Crystallography and Diffraction (3^{rd} Ed.), Oxford University Press, New York (2009)

Hanfland, M., Lorenzen, M., Wassilew-Reul, C., Zontone, F., Structural Studies of Nitrogen at High Pressures, Proceedings of Joint AIRAPT-16 & HPCJ-38, p. 130 (1998)

Hazen, R.M, Mao, H.K., Finger, L.W., Bell, P.M., Structure and Compression of Crystalline Methane at High Pressure and Room Temperature, Appl. Phys. Lett., 37 (3), 288 (1980)

Hebert, P., Polian, A., Loubeyre, P., Le Toullec, R., Optical Studies of Methane under High Pressure, Phys. Rev. B, 36 (17) 9196 (1987)

Heintz, A., Bich, E., Thermodynamics in an icy world: The atmosphere and internal structure of Saturn's moon Titan, Pure Appl. Chem., 81 (10) 1903 (2009)

Hellwig, H. Daniels, W.B., Hemley, R.J., Mao, H.K., Gregoryanz, E., Yu, Z., Coherent Anti-Stokes Raman Scattering Spectroscopy of Solid Nitrogen to 22 GPa, J. Chem. Phys., 115 (23) 10876 (2001)

Hemley, R.J., Effects of High Pressure on Molecules, Annu. Rev. Phys. Chem., 51, 763 (2000)

Hemley, R.J., Crabtree, G.W., Buchanan, M.V., Materials in Extreme Environments, Physics Today, Nov. 2009, 32 (2009)

Hemley, R.J., Mao, H.K., New windows on earth and planetary interiors, Mineralogical Magazine, 66 (5) 791 (2002)

Herczeg, J., Stoner, R.E., X-Ray Diffraction Determination of the Molecular Lattice of Solid Methane at 4.2 K, J. Chem. Phys., 54, 2284 (1971)

Hirai, H., Konagai, K., Kawamura, T., Yamamoto, Y., Yagi, T., Phase changes of solid methane under high pressure up to 86 GPa at room temperature, Chem. Phys. Lett., 454, 4-6, pp. 212 – 217, 2008

Izumi, F., Rietveld analysis of X-ray and neutron diffraction patterns, Journal of the Mineralogical Society of Japan, 17 (1) 37 (1985)

Jamieson, J. C., Lawson, A. W. & Nachtrieb, N. D., New device for obtaining X-ray diffraction patterns from substances exposed to high pressure, Rev. Sci. Instrum. 30, 1016, (1959)

Jayaraman, A., Optical Spectroscopy with the Diamond Anvil Cell, Physica, 139 & 140B, 464 (1988)

Katrusiak, A., High-pressure crystallography, Acta Cryst. A., A64, 135 (2007)

Kittel, C., Introduction to Solid State Physics (8th Ed.), John Wiley & Sons, USA (2005)

Kobashi, K., Okada, K., Yamaoto, T., Theory of phase transitions in solid methanes. XI. Infrared and Raman spectra of the v_3 and v_4 modes in phase II of solid CH_4, J. Chem. Phys., 66 (12) 5568 (1977)

Kooi, M.E., Schouten, J.A., High-pressure Raman investigation of mutual solubility and compound formation in Xe-N_2 and Ne-N_2, Phys. Rev. B, 60 (18) 12635 (1999)

Krupskii, I.N., Gasan V.M., Prokhvatilov, A.I., Spin Nuclear Conversion and Phase Transitions in Solid CH_4, Solid State Comm., 15 (5) 803 (1974)

Ladd, M., Palmer, R., Structure Determination by X-ray Crystallography (4th Ed.), Kluwer Academic/Plenum Publishers, New York (2003)

LeSar, R., Ekberg, S.A., Jones, L.H., Mills, R.L., Schwalbe, L.A., Schiferl, D., Raman Spectroscopy of solid nitrogen up to 374 kbar, Solid State Communications, 32 (2) 131 (1979)

Lotz, H.T., Schouten, J.A., Phase behaviour of the N_2-Ar system at high pressure: A Raman spectroscopy study, Phys. Rev. B, 64, Art. No. 024103 (2001)

Loubeyre, P., Jean-Louis, M., LeToullec, R., Charon-Gerard, L., High Pressure Measurement of the He-Ne Binary Phase Diagram at 296 K: Evidence for the Stability of a Stoichiometric Ne$(He)_2$ Solid, Phys. Rev. Lett., 70 (2) 178 (1993)

Mao, H.K., Bell, P.M., Shaner, J.W., Steinberg, D.J., Specific volume measurements of Cu, Mo, Pd, and Ag and calibration of the ruby R1 fluorescence pressure gauge from 0.06 to 1 Mbar, J. Appl. Phys. 49, 3276 (1978)

Mao, H.K., Hemley, J., The High-Pressure Dimension in Earth and Planetary Science, PNAS, 104 (22) 9114 (2008)

Martinez-Canales, M., Bergara, A., No Evidence of Metallic Methane at High Pressure, High Pressure Research, 26 (4) 369 (2006)

Maynard-Casely, H., The new mineralogy of the outer solar system and the high-pressure behaviour of methane, PhD Thesis, University of Edinburg, Edinburg (2009)

Maynard-Casely, H.E., Bull, C.L., Guthrie, M., Loa, I., McMahon, M.I., Gregoryanz, E., Nelmes, R.J., Loveday, J.S., The distorted close-packed crystal structure of methane A, J. Chem. Phys., 133, Art. No. 064504 (2010)

McLennan, J.C., Plummer, W.G., The Crystal Structure of Solid Methane, Nature, 122, 571, Art. No. 3076 (1928)

Medina, F.D, Daniels, W. B.,Raman Spectrum of beta-CH_4 in the Intramolecular and Lattice Regions , J. Chem. Phys., 70 (1) 242 (1979)

Medina, F.D., On the Existence of Phase IV of Solid Methane, Chem. Phys. Lett., 85 (1) 91 (1981)

Mills, R.L., Olinger, B., Cromer, D.T., Structures and phase diagrams of N_2 and CO to 13 GPa by X-ray diffraction, J. Chem. Phys., 84 (5) 2837 (1986)

Mooy, H.H., The Crystal Structure of Solid Methane, Nature, 127, 707 (1931)

Mulder, A., Michels, J.P.J., Schouten, J.A., Epsilon-Delta Phase transition of nitrogen and the orientational behaviour of the second order transition within the delta-phase: A Monte Carlo study at 7.0 GPa, Phys. Rev. B, 57 (13) 7571 (1998)

Muller, A., Schallamach, A., Crystal Structure of Methane at the Transition Point, 20.4K, Nature, 143, 375, Art. No. 3618 (1939)

Nakahata, I., Matusi, N., Akahama, Y., Kawamura, H., Structural Studies of Solid Methane at High Pressures, Chem. Phys. Lett., 302, 359 (1999)

Olijnyk, H., High Pressure X-ray diffraction studies on Solid N2 up to 43.9 GPa, J. Chem. Phys., 93 (12) 8968 (1990)

Olijnyk, H., Jephcoat, A.P., Lattice Modes of Solid Nitrogen to 104 GPa, Low Temp. Phys., 27 (9) 870 (2001)

Olinger, B., The Compression of Solid N_2 at 296 K from 5 to 10 GPa, J. Chem. Phys., 80 (3), 1309 (1984)

Omar, M.H., Dokoupil, Z., Schroten, H.G.M., Determination of the solid-liquid equilibrium diagram for the nitrogen-methane system, Physica, 28, 309 (1962)

Powell, B.M., Pawley, G.S.,A molecular-dynamics simulation study of the beta phase of nitrogen, J. Chem. Phys., 91 (12) 7877 (1989)

Press, W., Huller, A., On the Orientational Order in beta-Nitrogen, J. Chem. Phys., 68 (10) 4465 (1978)

Prokhvatilov, A.I., Isakina, A.P., Krupskii, I.N., Incommensurate Structures in Solid Methane and Deutromethane, Solid State Comm., 42 (1) 59 (1982)

Prokhvatilov, A.I., Yantsevich, L.D., X-ray investigations of the equilbrium phase diagram of CH_4-N_2 solid mixtures, Sov. J. Low Temp. Phys., 9 (2) 94 (1983)

Reichlin, R., Schiferl, D., Martin, S., Vanderborgh, C., Mills, R.L., Optical Studies of Nitrogen to 130 GPa, Phys. Rev. Lett., 55 (14) 1464 (1985)

Savoie, R., Fournier, R.P., Far-Infrared Spectra of Condensed Methane and Methane-d_4,Chem. Phys. Lett., 7 (1) 1 (1970)

Scheerboom, M.I.M., Schouten, J.A., Orientational behaviour of solid nitrogen at high pressures investigated by vibrational Raman spectroscopy, J. Chem. Phys., 105 (7) 2553 (1996)

Scheinder, H., Hainer, W., Wokaun, A., Olijnyk, H., Room temperature Raman Scattering Studies of External and Internal Modes of Solid Nitrogen at Pressure 8-54GPa, J. Chem. Phys., 96 (11) 8046 (1992)

Schenk, H. (Editor), Direct Methods of Solving Crystal Structures, Plenum Press, New York (1991)

Schiferl, D., Cromer, D.T., Ryan, R.R., Larson, A.C., LeSar, R., Mills, R.L., Structure of N_2 at 2.94 GPa and 300 K, Acta Cryst., C39, 1151 (1983)

Schouten, J.A., Recent advances in the study of high-pressure binary systems, J. Phys. Condens. Matter, 7, 469 (1995)

Schouten, J.A., What is Different in Mixtures? From Critical Point to High Pressures, International Journal of Thermophysics, 22 (1) 23 (2001)

Schouten, J.A., van Hinsberg, M.G.E., Scheerboom, M.I.M., Michels, J.P.J., Peculiarities in the high-pressure phase behaviour of binary mixtures of nitrogen with methane, helium and water, J. Phys. Condens. Matter, 6, A187 (1994)

Schuch, A.F., Mills, R.L., Crystal Structures of the Three Modifications of Nitrogen 14 and Nitrogen 15 at High Pressure, J. Chem. Phys., 52 (12) 6000 (1970)

Serway, R.A., Jewett, J.W., Physics for Scientists and Engineers, Brooks Cole (2004)

Shirley, R., The Crysfire System for Automatic Powder Indexing: User's Manual, The Lattice Press, Guildford, England (2000)

Sihachkr, D., Etudes de N_2/O_2 sous pression, PhD thesis, Université Paris XXI, Orsay (2005)

Sihachakr, D., Loubeyre, P.,O_2/N_2 mixtures under pressure: A structural study of the binary phase diagram at 295 K, Phys. Rev. B, 70, Art. No. 134105 (2004)

Smith, J.S., Desgreniers, S., Selected techniques in diamond anvil cell crystallography: centring samples using X-ray transmission and rocking powder samples to improve X-ray diffraction image quality, J. Synchrotron Rad. 16, 83 (2009)

Smith, J.S., High-pressure study of the heavy alkaline earth hydrides, PhD Thesis, University of Ottawa, Ottawa (2009)

Somayazulu, M.S., Finger, L.W., Hemley, R.J., Mao, H.K., High-Pressure Compounds in Methane-Hydrogen Mixtures, Science, 271 (5254) 1400 (1996)

Stevenson, R., Solid Methane – Changes in Phase under Pressure, J. Chem. Phys., 27 (3) 656 (1957)

Stewart, J.W., Phase Transitions and Compressions of Solid CH_4, CD_4 and O_2, J. Phys. Chem. Solids, 12, 122 (1959)

Stinton, G.W., Loa, I., Lundegaard, L.F., McMahon, M.I., The Crystal Structure of Delta and Delta* Nitrogen, J. Chem. Phys., 131, Art. No. 104511 (1998)

Stinton, G.W., Loa, I., Lundegaard, L.F., McMahon, M.I., The Crystal Structures of Delta and Delta-loc nitrogen, J. Chem. Phys., 131, Art. No. 104511 (2009)

Streib, W.E., Jordan, T.H., Lipscomb, W. N., Single Crystal X-Ray Diffraction Study of Beta-Nitrogen, J. Chem. Phys., 37 (12) 2962 (1962)

Sun, L., Ruoff, A.L., Zha, C.S., Stupian, G., Optical Properties of Methane to 288 GPa at 300 K, J. Phys. Chem. Solids, 67, 2603 (2006)

Sun, L., Yi, W., Wang, L., Shu, J., Sinogeikin, S., Meng, Y., Shen, G., Bai, L., Li, Y., Liu, J., Mao, H.K., Mao, W.L., X-Ray Diffraction Studies and Equation of State of Methane at 202 GPa, Chem. Phys. Lett., 473, 72 (2009)

Swenson, C.A., New Modification of Solid Nitrogen, J. Chem. Phys., 23 (10) 1963 (1957)

Syassen, K., Ruby under Pressure, High Pressure Research, 28 (2), 75 (2008)

Tassini, L., Gorelli, F., Ulivi, L., High Temperature Structures and Orientational Disorder in Compressed Solid Nitrogen, J. Chem. Phys., 122, Art. No. 074701 (2005)

Thiery, M.M, Fabre, D., Kobashi, K., Raman Spectra of solid CH_4 under high pressure. III. New high pressure phases in solid CH_4 and CD_4, J. Chem. Phys., 63 (12) 6165 (1985)

Trapenzikova, O., Mujtin, G., Specific Heat of Methane under Pressure, Nature,144,632 (1939)

Ulivi, L., Bini, R., Santoro, M., Extended spectroscopic studies of $Ar(H_2)_2$ at high pressure and low temperature, Physica B, 265, 39 (1999)

Umemoto, S., Yoshii, T., Akahama, Y., Kawamura, H., X-ray diffraction measurements for solid methane at high pressures, J. Phys.: Condens. Matter, 14, 10675 (2002)

Van der Putten, D., Prins, K.O., The Phase Diagram of the Solid Methanes, Int. J. Thermophysics, 10 (6) 1205 (1989)

Vos, W.L., Finger L.W., Hemley, R.J., Hu, J.Z., Mao, H.K., Schouten, J.A., A high-pressure van der Waals compound in solid nitrogen-helium mixtures, Nature, 358, 46 (1992)

Weck, G., Dewaele, A., Loubeyre, P., Oxygen/noble gas binary phase diagrams at 296 K and high pressures, Phys. Rev. B, 82, Art. No. 014112 (2010)

Wigner, E., Huntington, H.B., On the possibility of a metallic modification of hydrogen, J. Chem. Phys. 3, 764 (1935)

Westerhoff, T., Feile, R., High-pressure Raman study of the N_2 stretching vibration ion argon-nitrogen mixtures at room temperature, Phys. Rev. B, 54 (2) 913 (1996)

Zinn, A.S., Schiferl, D., Raman Spectroscopy and melting of nitrogen between 290 and 900 K and 2.3 and 18 GPa , J. Chem. Phys., 87 (2) 1267 (1987)

Permissions for Figures:

Figure No.	Reference	Licence Number/Copyright Information
2.3, 5.12	Somayazulu, 1996	Permitted by section 2.1f in the JSTOR terms and conditions of use
2.4	Omar, 1962	2570890732495
2.5, 4.2	Connolley, 1980	2570900050970
2.6	Gregoryanz, 2007	2570891446065
2.8, 2.14, 5.8a	Mills, 1986	2571430510513
2.9	Buchsbaum, 1984	2570880725958
2.11	Scheerboom, 1996	2570891129832
2.13	Stinton, 2009	2570900612357
2.18, 2.20, 2.21	Maynard-Casely, 2010	2570910614926, 2571390575426
2.19	Nakahata, 1999	2570890569949
2.22	Hirai, 2008	2571410072050
5.10, 5.11	Weck, 2010	Permission granted with the following acknowledgment: Copyright 2010 by The American Physical Society
5.10, 5.11	Kooi, 1999	Permission granted with the following acknowledgment: Copyright 1999 by The American Physical Society

Additional Permissions Information:

Fig. 5.10 and 5.11 in this thesis used figures reprinting from the following articles:

Weck, G., Dewaele, A., Loubeyre, P., Oxygen/noble gas binary phase diagrams at 296 K and high pressures, Phys. Rev. B, 82, Art. No. 014112 (2010). Copyright (2010) by the American Physical Society.

Link: http://prb.aps.org/abstract/PRB/v82/i1/e014112

Kooi, M.E., Schouten, J.A., High-pressure Raman investigation of mutual solubility and compound formation in Xe-N_2 and Ne-N_2, Phys. Rev. B, 60 (18) 12635 (1999). Copyright (1999) by the American Physical Society.

Link: http://prb.aps.org/abstract/PRB/v60/i18/p12635_1

Permission for figure use was also obtained directly from the first author of each publication.